Nanostructured Birefringent and Gradient-Index Micro-Optical Elements

Jędrzej M. Nowosielski

A thesis submitted for the degree of

Doctor of Philosophy

Heriot-Watt University

School of Engineering and Physical Sciences

December 2013

Abstract

The main goal of this thesis is the numerical and experimental verification of the concept of the structured micro-optical elements fabricated with the modified stack-and-draw technique. This technology, based on the well-known method of photonic crystal fibres (PCFs) production, allows the fabrication of nanostructured GRIN microlenses, *form birefringent* nanostructured materials and diffractive optical elements (DOEs). The principle of operation of the nanostructured GRIN (nGRIN) microlenses as well as the form birefringent nanostructured material can be explained by an effective medium theory (EMT). Both the approach based on the Maxwell-Garnet formula used for a description of nanostructured GRIN microlenses and the second-order EMT needed to account for birefringence properties are introduced. Numerical simulations of a Gaussian beam focusing and collimation (within GRIN microlenses) are performed using a FDTD method. The modelling results show that nGRIN microlenses can be described using the notion of the effective permittivity (or the effective refractive index) also in the case of the Gaussian beam illumination. Futhermore, Gaussian beam propagation within nGRIN microlenses can be approximately described by the paraxial scalar theory of the GRIN medium despite a high refractive index gradient. The concept of a so-called large-diameter nGRIN microlens with a quantised refractive index profile is introduced. Numerical simulations, performed using fast Fourier transform beam propagation method (FFT-BPM), show that focusing properties of the large-diameter quantised nGRIN microlens are similar to the focusing characteristic of the corresponding ideal continuous GRIN microlens. Both simulation and experimental results show that the fabricated large-diameter quantised nGRIN microlens has good chromatic properties in a range 633nm - 850nm. The successful fabrication of the prototype birefringent nanostructured element and a few diffractive checkerboards structures with different feature sizes is also reported. Applicability of the second-order EMT in the case of the fabricated birefringent material is verified both numerically, using the FDTD method, and experimentally. Diffractive patterns produced by DOEs are shown.

Acknowledgements

First of all, I would like to thank Prof. Mohammad R. Taghizadeh and Prof. Ryszard Buczyński for recruiting me into the project, and furthermore I would like to thank them for their great patience, kindness and support during the difficult moments of my work. My words of gratitude go also to Prof. Katarzyna Chałasińska-Macukow for support and advice which I received from her during my PhD studies.

My work was funded by Engineering and Physical Sciences Research Council (EPSRC) and Foundation for Polish Science (FNP). This work was supported by the Foundation for Polish Science Team Programme co-financed by the European Regional Development Fund, Operational Program Innovative Economy 2007-2013.

Many people helped me during my studies and it is difficult to mention them all here by name. I want to express a particular gratitude to Darek Pysz and Irek Kujawa from Institute of Electronic Materials Technology (ITME) as well as Neil Ross for providing me with a training in a micro-optical technology. I also want to express my gratitude to Dr Andrew Waddie, who greatly helped me in the numerical and theoretical parts of the work. During microlens measurements I received great support from Stewart Duffin and Dr Aongus McCarthy. I am also grateful to my colleagues and also friends Adam Filipkowski and Dr Florian Hudelist for good team work.

Last but not least, I want to thank my girlfriend Celina Heliasz and my parents for support, patience and understanding.

ACADEMIC REGISTRY
Research Thesis Submission

Name*:*	Jędrzej Marek Nowosielski		
School/PGI:	School of Engineering and Physical Sciences		
Version: *(i.e. First, Resubmission, Final)*	Final	Degree Sought (Award **and** Subject area)	PhD, Physics

Declaration

In accordance with the appropriate regulations I hereby submit my thesis and I declare that:

1) the thesis embodies the results of my own work and has been composed by myself
2) where appropriate, I have made acknowledgement of the work of others and have made reference to work carried out in collaboration with other persons
3) the thesis is the correct version of the thesis for submission and is the same version as any electronic versions submitted*.
4) my thesis for the award referred to, deposited in the Heriot-Watt University Library, should be made available for loan or photocopying and be available via the Institutional Repository, subject to such conditions as the Librarian may require
5) I understand that as a student of the University I am required to abide by the Regulations of the University and to conform to its discipline.

* *Please note that it is the responsibility of the candidate to ensure that the correct version of the thesis is submitted.*

Signature of Candidate*:*		Date:	

Submission

Submitted By *(name in capitals):*	
Signature of Individual Submitting:	
Date Submitted:	

For Completion in the Student Service Centre (SSC)

Received in the SSC by *(name in capitals):*			
Method of Submission *(Handed in to SSC; posted through internal/external mail):*			
*E-thesis Submitted (**mandatory for final theses)***			
Signature:		Date:	

Please note this form should bound into the submitted thesis.

Updated February 2008, November 2008, February 2009, January 2011

Contents

Author's Journal Contributions

1. J. M. Nowosielski, R. Buczynski, F. Hudelist, A. Waddie, D. Pysz, R. Stępień, I. Kujawa, and M. R. Taghizadeh, "Focusing a Gaussian beam in nanostructured non-periodic GRIN microlenses," *Photonics Letters of Poland*, vol. 2, no. 1, pp. 34–36, 2010.

2. J. M. Nowosielski, R. Buczynski, F. Hudelist, A. J. Waddie, and M. R. Taghizadeh, "Nanostructured GRIN microlenses for Gaussian beam focusing," *Optics Communications*, vol. 283, no. 9, pp. 1938–1944, 2010.

3. J. Nowosielski, R. Buczynski, A. J. Waddie, A. Filipkowski, D. Pysz, A. McCarthy, R. Stepien, and M. R. Taghizadeh, "Large diameter nanostructured gradient index lens," *Opt. Express*, vol. 20, pp. 11767–11777, May 2012.

4. F. Hudelist, J. M. Nowosielski, R. Buczynski, A. J. Waddie, and M. R. Taghizadeh, "Nanostructured elliptical gradient-index microlenses," *Optics Letters*, vol. 35, no. 2, pp. 130–132, 2010.

5. A. J. Waddie, R. Buczynski, F. Hudelist, J. Nowosielski, D. Pysz, R. Stepien, and M. R. Taghizadeh, "Form birefringence in nanostructured micro-optical devices," *Opt. Mater. Express*, vol. 1, pp. 1251–1261, Nov 2011.

6. M. R. Taghizadeh, A. J. Waddie, R. Buczynski, J. Nowosielski, A. Filipkowski, and D. Pysz, "Nanostructured micro-optics based on a modified stack-and-draw fabrication technique," *Adv. Opt. Techn.*, vol. 1, no. 3, pp. 171–180, 2012.

Chapter 1

Introduction

The main theme of this thesis is the numerical and experimental verification of the concept of the structured micro-optical elements fabricated with the modified stack-and-draw technique. Most of the work concerns components with the internal sub-wavelength nanostructure with a feature size in the range of $100-300$nm. Additionally the diffractive optical elements (DOEs), with feature sizes larger than a wavelength, produced using the same technique, are tested.

The stack-and-draw technique has been widely used for photonic crystal fibres (PCFs) production and it is now a mature technology.

The novelty of the micro-optical elements, described in this thesis, is about the use of the slightly modified version of this technique for the fabrication of other optical elements i.e. nanostructured gradient-index (GRIN) microlenses, form birefringent nanostructured materials and microstructured DOEs.

The general idea of the considered technology consists in the construction of a macroscopic preform which is assembled out of glass rods with a diameter of $\sim$ 1mm. The glass rods of two types (with two different refractive indices) are arranged according to a designed pattern. Next, the preform is drawn down using the fibre draw tower and the cross-section of the structure is scaled down during the drawing. Usually the drawing is repeated once or twice in order to reach the desired feature size in the final structure. Finally, unlike in the case of fibre production, the output rod is cut into slices, which are then polished down to a required thickness. Each slice is a ready micro-optical element. The fabrication of element arrays is also possible. This fabrication approach has a number of important advantages compared to more traditional techniques such as an ion exchange method or an electron beam lithography:

- significant freedom of design in terms of the refractive index distribution in the cross-section of the optical element – possibility of nonsymmetric index distributions and the high index gradients
- robust and easy to integrate elements with flat facets

- large number elements produced from a single preform leading to a low cost of a single element.

The principle of the operation of the nanostructured GRIN microlenses as well as the nanostructured birefringent material can be explained by an effective medium theory (EMT). Optical properties of the nanostructured GRIN microlenses are described in terms of effective refractive index (or effective permittivity). In the case of the considered microlenses effective permittivity can be simply approximated by the volume average of the permittivity in the neighbourhood of a given point. In the case of the nanostructured birefringent material a desired level of an anisotropy is attained by a layered nanostructure of the material which consists of many subwavelength (in thickness) layers made of two different glasses.

Chapter 2 covers a theoretical and a literature background of the thesis subject. The geometrical optics of the GRIN medium as well as the wave optics description of the GRIN rod lenses is provided. Next, the effective medium theory (EMT) is introduced. Both the approach based on the Maxwell-Garnet formula used for description of nanostructured GRIN microlenses and the second-order EMT, needed to account for birefringence properties, are explained. Section 2.4 contains a description of main features of the finite difference time domain method (FDTD) and a description of the fast Fourier transform beam propagation method (FFT-BPM). These two methods have been used for numerical verification of the optical performance of the investigated elements. Section 2.5 is devoted to techniques, such us an ion exchange method, used for fabrication of classical GRIN lenses.

Chapter 3 covers mainly the concept and fabrication of so-called small-diameter nanostructured GRIN (nGRIN) microlenses. First, a short overview of the nanostructured GRIN optical elements, proposed in literature, is provided. Next, the concepts of the small-diameter as well as so-called large-diameter nanostructured GRIN microlenses, fabricated using the modified stack-and-draw technique, are explained. In section 3.2.1 the fabrication of the small-diameter nanostructured GRIN microlenses is described in detail. At the end of the chapter, a numerical optimisation of the nanorod distribution within the small-diameter nGRIN microlens, based on a simulated annealing (SA) method, is introduced.

In chapter 4 the problem of a Gaussian beam propagation within small-diameter nGRIN microlenses is investigated numerically using the FDTD method. The Gaussian beam focusing using both nanostructured GRIN microlenses and the corresponding 'classical' continuous GRIN microlenses has been modelled. The simulations have been performed in order to verify if the nGRIN microlenses have the same optical properties as the corresponding classical GRIN microlenses. Moreover, it is investigated how accurate a scalar paraxial GRIN theory is in the case of the Gaussian beam

propagation within nGRIN microlenses with a high refractive index gradient. Additionally in section 4.2 the simulation of the Gaussian beam collimation is discussed in order to show suitability of nGRIN microlenses for collimation of the beam generated by a VCSEL.

Chapter 5 is devoted to so-called large-diameter quantised nGRIN microlenses. The diameter of the small-diameter nGRIN microlenses is limited, in practice, to 20–30μm due to a limited number of rods that can be assembled into the initial preform. Hence, the concepts of nanostructured metarods and quantised refractive index profile have been introduced to tackle this issue. Section 5.2 covers a detailed description of the quantised nanostructured microlens fabrication. Simulations (performed using FFT-BPM) show that such quantised microlenses have similar focusing properties to the corresponding unquantised continuous GRIN microlenses. Additionally the chromatic properties of the fabricated prototype of quantised nanostructured microlens have been verified both experimentally and numerically.

Chapter 6 covers novel micro and nanostructured elements fabricated using the modified stack-and-draw technique. A new approach to the fabrication of the birefringent nanostructured materials as well as diffractive optical elements (DOEs) is introduced. The successful fabrication of the prototype birefringent nanostructured element and a few DOE checkerboards with different feature sizes is reported. Applicability of the second-order EMT in the case of the fabricated birefringent material has been verified both numerically, using the FDTD method, and experimentally. Preliminary measurements of the diffraction pattern given by fabricated DOEs are described in section 6.2.2.

Chapter 7 is devoted to the thesis conclusions and suggestions for future work.

Chapter 2

GRIN medium: theory, modelling and fabrication

In this chapter geometrical optics and wave optics descriptions of the GRIN medium are presented. In many cases the principle of operation of the GRIN lenses can be explained using geometrical optics. Moreover ray optics is a base to describe Gaussian beam propagation in GRIN lenses as it is shown in section 2.2. Next an effective medium theory (EMT) is introduced. EMT is essential to understand the principle of operation of the nanostructured GRIN microlenses and nanostructured birefringent materials which are the subject of this thesis. Section 2.4 is devoted to the short description of the two numerical methods which are used for simulation of light propagation through Gradient-Index and birefringent micro-optical elements considered in this thesis. In section 2.5 there are presented various methods of classical GRIN lens fabrication.

2.1 Geometrical optics of the GRIN medium

Approximation of the geometrical optics can be applied for optical systems where any obstacle which is encountered by the light has dimensions much larger than the wavelength of light. In geometrical optics the notion of the light rays. A light ray is a trajectory whose direction in a given location is the same as a direction of the light propagation in this location.

It is desirable to have an equation which determines ray trajectories in a inhomogeneous medium. Such equation can be derived from Fermat's principle [1, 2]. It is the variational principle based on the notion of optical path length. For a given path between two points P_1 and P_2 optical path length is defined as

$$\int_{P_1}^{P_2} n(x,y,z)\,ds \tag{2.1}$$

where n is the refractive index and ds is the differential element of length along the considered path. Fermat's principle states that light ray travelling between two points

P_1 and P_2 follows a trajectory such that optical path length is an extremum compared to other paths in immediate neighbourhood. The extremum is usually a minimum. The minimisation of the optical path length is equivalent to the minimisation of the time of travel between two points. Fermat's principle can be expressed as

$$\int_{P_1}^{P_2} n(x,y,z)\,ds = \text{extremum} \tag{2.2}$$

It is convenient to change variable of integration. The differential element ds of length along the path is equal to

$$ds = \sqrt{dx^2+dy^2+dz^2} = \sqrt{1+\dot{x}^2+\dot{y}^2}\,dz \tag{2.3}$$

where

$$\dot{x} = \frac{dx}{dz};\ \dot{y} = \frac{dy}{dz} \tag{2.4}$$

One can express Eq. (2.2) in the form

$$\int_{P_1}^{P_2} L(x,y,\dot{x},\dot{y},z)\,dz = \text{extremum} \tag{2.5}$$

where

$$L(x,y,\dot{x},\dot{y},z) = n(x,y,z)\sqrt{1+\dot{x}^2+\dot{y}^2} \tag{2.6}$$

The axis Z is usually chosen to coincide with the optical axis of the system. The solution of the problem (2.5) is given by Euler equations

$$\frac{d}{dz}\frac{\partial L}{\partial \dot{x}} - \frac{\partial L}{\partial x} = 0, \tag{2.7a}$$

$$\frac{d}{dz}\frac{\partial L}{\partial \dot{y}} - \frac{\partial L}{\partial y} = 0. \tag{2.7b}$$

After substitution of Eq. (2.6) into Euler equations (2.7) one can obtain

$$\frac{d}{dz}\left[\frac{n\dot{x}}{\sqrt{1+\dot{x}^2+\dot{y}^2}}\right] = \sqrt{1+\dot{x}^2+\dot{y}^2}\frac{\partial n}{\partial x}, \tag{2.8a}$$

$$\frac{d}{dz}\left[\frac{n\dot{y}}{\sqrt{1+\dot{x}^2+\dot{y}^2}}\right] = \sqrt{1+\dot{x}^2+\dot{y}^2}\frac{\partial n}{\partial y}. \tag{2.8b}$$

A light ray is described by functions $x(z)$ and $y(z)$ which must satisfy Eq. (2.8). It is convenient to introduce the direction cosines of the light with respect to X, Y and Z axes

$$\cos\alpha = \frac{\dot{x}}{\sqrt{1+\dot{x}^2+\dot{y}^2}}, \tag{2.9a}$$

$$\cos\beta = \frac{\dot{y}}{\sqrt{1+\dot{x}^2+\dot{y}^2}}, \tag{2.9b}$$

$$\cos\gamma = \frac{1}{\sqrt{1+\dot{x}^2+\dot{y}^2}} \tag{2.9c}$$

and also optical direction cosines

$$p = n\cos\alpha, \tag{2.10a}$$

$$q = n\cos\beta, \tag{2.10b}$$

$$l = n\cos\gamma. \tag{2.10c}$$

Using optical direction cosines one can express Eq. 2.8 as

$$\dot{p} = \frac{n}{l}\frac{\partial n}{\partial x}, \tag{2.11a}$$

$$\dot{q} = \frac{n}{l}\frac{\partial n}{\partial y}, \tag{2.11b}$$

where $\dot{p}$ denotes the derivative of p with respect to z.

Let us consider following distribution of the permittivity n^2

$$n^2(x,y) = n_0^2[1 - g_0^2(x^2 + y^2)]. \tag{2.12}$$

It is difficult to find exact solution of the Eq. (2.8). In many practical cases it is sufficient to use paraxial approximation i.e., to consider only these rays which are nearly parallel to the optical axis (Z axis). In paraxial approximation Eq. (2.8) can be simplified to the paraxial ray equations

$$\frac{d}{dz}(n\dot{x}) = \frac{\partial n}{\partial x}, \tag{2.13a}$$

$$\frac{d}{dz}(n\dot{y}) = \frac{\partial n}{\partial y}. \tag{2.13b}$$

It is also assumed that rays are in the proximity of the optical axis that

$$g_0^2(x^2 + y^2) \ll 1 \tag{2.14}$$

so one can express refractive index distribution to a first order approximation as

$$n(x,y) = n_0[1 - \frac{g_0^2}{2}(x^2 + y^2)]. \tag{2.15}$$

Taking into account Eq. 2.15 and condition 2.14 paraxial ray equations are

$$\frac{d}{dz}(n_0\dot{x}) = -n_0 g_0^2 x, \tag{2.16a}$$

$$\frac{d}{dz}(n_0\dot{y}) = -n_0 g_0^2 y. \tag{2.16b}$$

which can be simplified to

$$\ddot{x} = -g_0^2 x, \tag{2.17a}$$

$$\ddot{y} = -g_0^2 y. \tag{2.17b}$$

Since the refractive index distribution is symmetric in x, y and Eqs. (2.17a), (2.17b) are essentially the same, only Eq. (2.17a) will be considered. Analysis of Eq. (2.17b)

is analogous. Eq. (2.17a) possesses oscillatory solutions. Any paraxial ray may be represented as a linear combination of the two particular solutions. First of them, the axial ray $x_a = H_a(z)$ is determined by the initial conditions

$$H_a(0) = 0, \tag{2.18a}$$

$$\dot{H}_a(0) = 1. \tag{2.18b}$$

And the second particular solution $x_f = H_f(z)$ called the field ray satisfies initial conditions

$$H_f(0) = 1, \tag{2.19a}$$

$$\dot{H}_f(0) = 0. \tag{2.19b}$$

The axial ray and the field ray are given by

$$H_a(z) = \frac{\sin(g_0 z)}{g_0}, \tag{2.20a}$$

$$H_f(z) = \cos(g_0 z). \tag{2.20b}$$

Trajectory of every paraxial ray can be described by linear combination of these two particular solutions

$$x(z) = x(0)H_f(z) + \dot{x}(0)H_a(z) \tag{2.21}$$

The slope $\dot{x}$ of the arbitrary paraxial ray is given by

$$\dot{x}(z) = x(0)\dot{H}_f(z) + \dot{x}(0)\dot{H}_a(z) \tag{2.22}$$

One can simplify Eq. (2.10a)

$$p = n_0 \dot{x} \tag{2.23}$$

and hence optical direction cosine can be express in terms of the field and axial ray as

$$p(z) = n_0 x(0)\dot{H}_f(z) + p(0)\dot{H}_a(z). \tag{2.24}$$

Let us consider a rod (cylinder) with length (thickness) L and radius a where permittivity distribution within the rod is given by Eq. (2.12). The rod is surrounded by air. The considered rod can work as a thick lens and might be used for light focusing. The schematic of the focusing is shown in Fig. 2.1. One can calculate working distance $\overline{V'F'}$ and effective focal length f of the lens using trajectory of the field ray H_f and Snell's law. The ray trajectory within the lens is given by

$$x_{\text{in}}(z) = x_{\text{in}}(0)H_f(z) = x_{\text{in}}(0)\cos(g_0 z). \tag{2.25}$$

Hence on the output facet of the lens

$$x_{\text{in}}(L) = x_{\text{in}}(0)\cos(g_0 L). \tag{2.26}$$

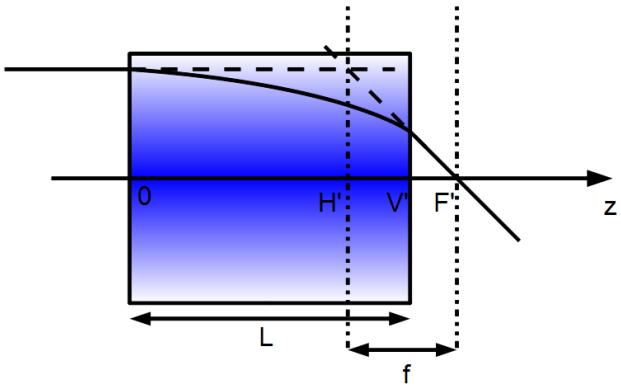

Figure 2.1 – The schematic of the focusing using GRIN rod lens. $\overline{V'F'}$ - working distance. f - effective focal length.

Snell's law related to the refraction occurring on the output facet of the lens can be expressed as

$$\dot{x}_{\text{in}}(L)n_0 = \dot{x}_{\text{out}}(L). \tag{2.27}$$

where $\dot{x}_{\text{out}}$ denotes the ray slope behind the GRIN lens. This slope is equal to

$$\dot{x}_{\text{out}}(L) = -\frac{x_{\text{in}}(L)}{\overline{V'F'}}. \tag{2.28}$$

From Eqs. (2.25) and (2.27) it is easy to calculate that

$$\dot{x}_{\text{in}}(L) = -x_{\text{in}}(0)g_0 \sin(g_0 L), \tag{2.29}$$

$$\dot{x}_{\text{out}}(L) = -n_0 x_{\text{in}}(0)g_0 \sin(g_0 L). \tag{2.30}$$

Finally the working distance $\overline{V'F'}$ is given by

$$\overline{V'F'} = -\frac{x_{\text{in}}(L)}{\dot{x}_{\text{out}}(L)} = \frac{1}{n_0 g_0 \tan(g_0 L)}. \tag{2.31}$$

If the lens length $L = L_{QP} = \pi/(2g_0)$, the working distance $\overline{V'F'}$ is equal to 0 meaning that the focal point is located on the output facet of the lens. The lens length $L_{QP} = \pi/(2g_0)$ is called the quarter pitch length.

Taking into consideration Fig. 2.1 one can see that

$$-\frac{x_{\text{in}}(0)}{f} = \dot{x}_{\text{out}}(L), \tag{2.32}$$

which means that effective focal length f is given by

$$f = -\frac{x_{\text{in}}(0)}{\dot{x}_{\text{out}}(L)} = \frac{1}{g_0 n_0 \sin(g_0 L)}. \tag{2.33}$$

2.2 Wave optics of the GRIN medium

GRIN microlenses considered in this thesis are intended for integration with laser sources. The wave optics and Gaussian beam optics in particular is widely used for the laser beam description. The wave optics describes interference and diffraction.

2.2.1 Scalar time-dependent wave equation and scalar Helmholtz equation

The light is described by scalar wave function $u(\mathbf{r},t)$. It can represent any component of electric or magnetic field vectors. If the relative permittivity n^2 changes only slightly over a distance of the wavelength wave function satisfy following wave equation [2]

$$\frac{\partial^2 u}{\partial x^2}+\frac{\partial^2 u}{\partial y^2}+\frac{\partial^2 u}{\partial z^2}-\frac{n^2}{c_0^2}\frac{\partial^2 u}{\partial t^2}=0, \tag{2.34}$$

where c_0 and n denote the speed of light in vacuum and the refractive index respectively.

It is possible to simplify wave equation when the monochromatic wave is considered. The real wave function of the monochromatic wave can be expressed as

$$u(\mathbf{r},t)=A(\mathbf{r})\cos(\omega t+\delta(\mathbf{r})), \tag{2.35}$$

where
$A(\mathbf{r})$ - real amplitude
ω - angular frequency
$\delta(\mathbf{r})$ - phase
It is advantageous to introduce a complex wave function $U(\mathbf{r},t)$ of the monochromatic wave

$$U(\mathbf{r},t)=A(\mathbf{r})\exp(i\delta(\mathbf{r}))\exp(i\omega t). \tag{2.36}$$

From Eq. (2.36) it is evident that

$$u(\mathbf{r},t)=\mathfrak{Re}\{U(\mathbf{r},t)\}, \tag{2.37}$$

where $\mathfrak{Re}\{U(\mathbf{r},t)\}$ denotes the real part of $U(\mathbf{r},t)$. Complex wave function $U(\mathbf{r},t)$ also satisfies the scalar wave equation (2.34). It is convenient to represent $U(\mathbf{r},t)$ as a product of the time-independent factor $\psi(\mathbf{r})$ and the factor $\exp(i\omega t)$

$$U(\mathbf{r},t)=\psi(\mathbf{r})\exp(i\omega t). \tag{2.38}$$

The time-independent factor $\psi(\mathbf{r})$ is called the complex amplitude. After substituting formula (2.38) into the scalar wave equation (2.34) one can obtain the scalar Helmholtz equation [2]

$$\frac{\partial^2 \psi}{\partial x^2}+\frac{\partial^2 \psi}{\partial y^2}+\frac{\partial^2 \psi}{\partial z^2}+k_0^2 n^2\psi=0, \tag{2.39}$$

where $k_0=\omega/c_0$ denotes the wavenumber in the vacuum. Let us consider permittivity distribution (2.12) which satisfies the condition (2.14). In many practical situations a beam propagates along the direction which differs only slightly from the optical axis

Z. In such case the paraxial approximation can be utilised[3, 4]. In order to derive the paraxial wave equation it is convenient to express complex amplitude $\psi(\mathbf{r})$ as

$$\psi(\mathbf{r}) = \phi(\mathbf{r}) \exp(-ik_0 n_0 z). \tag{2.40}$$

$\phi(\mathbf{r})$ is called a slowly varying envelope. A change of $\phi(\mathbf{r})$ over a distance of a wavelength in the Z direction compared to change of the factor $\exp(-ik_0 n_0 z)$. Substituting the formula (2.40) into the Helmoltz equation (2.39) one obtains [5]

$$\frac{\partial^2 \phi}{\partial x^2} + \frac{\partial^2 \phi}{\partial y^2} + \frac{\partial^2 \phi}{\partial z^2} - i2k_0 n_0 \frac{\partial \phi}{\partial z} + k_0^2 (n^2 - n_0^2)\phi = 0. \tag{2.41}$$

In the paraxial approximation a relation $|\partial^2 \phi / \partial z^2| \ll 2k_0 n_0 |\partial \phi / \partial z|$ is assumed and hence $\partial^2 \phi / \partial z^2$ in Eq. (2.41) can be neglected. The paraxial wave equation is obtained

$$\frac{\partial^2 \phi}{\partial x^2} + \frac{\partial^2 \phi}{\partial y^2} - i2k_0 n_0 \frac{\partial \phi}{\partial z} + k_0^2 (n^2 - n_0^2)\phi = 0. \tag{2.42}$$

2.2.2 Gaussian beam propagation in GRIN medium

Keeping assumptions about paraxiality and permittivity distribution (Eq. (2.12) and the condition (2.14)) let us consider Gaussian beam propagation through a GRIN rod lens. Orientation of the GRIN lens with respect to Cartesian coordinate system is shown in Fig. 2.2.

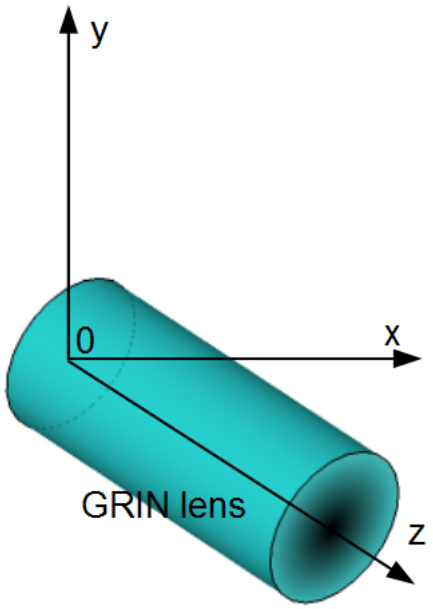

Figure 2.2 – GRIN rod lens in the Cartesian coordinate system. Refractive index gradient is shown by color at the output facet of the lens.

If plane Gaussian illumination with maximum intensity located on Z axis is used the complex amplitude on the input facet of GRIN lens is described by

$$\psi(x, y, z = 0) = \exp\left(-\frac{x^2 + y^2}{w_0^2}\right) \tag{2.43}$$

where w_0 is waist radius of Gaussian beam. This waist is located on the input facet of the lens. The complex amplitude within GRIN lens is given by

$$\psi(x, y, z) = \frac{1}{G_p(z)} \exp[-ik_0 n_0 z] \exp\left[\frac{-i\pi n_0 \dot{G}_p(z)}{\lambda_0 G_p(z)}(x^2 + y^2)\right] \tag{2.44}$$

where λ_0 is vacuum wavelength and function $G_p(z)$ is expressed using the axial ray and the field ray (Eqs. (2.20))

$$G_p(z) = H_f(z) - i\frac{\lambda_0}{\pi n_0 w_0^2} H_a(z). \tag{2.45}$$

A detailed derivation of the formula (2.44) is described in the book [3]. The formula (2.44) can be expressed using the radius of wavefront curvature $R(z)$ and beam radius $w(z)$

$$\psi(x, y, z) = \frac{1}{G_p(z)} \exp[-ik_0 n_0 z] \exp\left[-\frac{x^2 + y^2}{w^2(z)}\right] \exp\left[\frac{-i\pi(x^2 + y^2)}{\lambda_0 R(z)}\right], \tag{2.46}$$

where

$$w^2(z) = w_0^2 |G_p(z)|^2, \tag{2.47}$$

$$\frac{1}{R(z)} = \frac{n_0}{2w^2(z)} \frac{dw^2(z)}{dz}. \tag{2.48}$$

Substituting (2.20) and (2.45) into (2.47) the formula

$$w^2(z) = w_0^2 \left[cos^2(g_0 z) + \left(\frac{\lambda_0}{\pi n_0 w_0^2 g_0}\right)^2 sin^2(g_0 z)\right] \tag{2.49}$$

is obtained.

The quantity

$$w_{\text{fm}} = \left(\frac{\lambda_0}{\pi n_0 g_0}\right)^{1/2} \tag{2.50}$$

is the half-width of the fundamental mode of the medium described by permittivity distribution (2.12) [1, 3].

Using the half-width of the fundamental mode formula (2.49) can be written as

$$w^2(z) = w_0^2 \left[cos^2(g_0 z) + \frac{w_{\text{fm}}^4}{w_0^4} sin^2(g_0 z)\right] \tag{2.51}$$

It is clearly visible that if $w_0 = w_{\text{fm}}$ then $w(z)$ is independent of z. Otherwise $w(z)$ is periodical with the period of π/g_0.

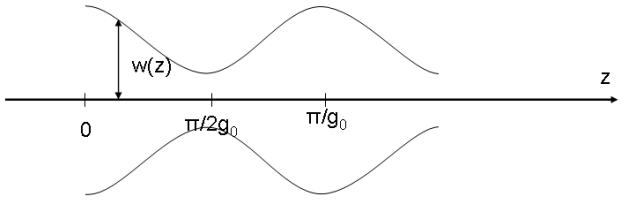

Figure 2.3 – Schematic of the Gaussian beam propagation through the GRIN medium with permittivity distribution given by Eq. (2.12) when $w_0 > w_{\mathrm{fm}}$

If $w_0 > w_{\mathrm{fm}}$ $w(z)$ decreases for $0 < z < \pi/(2g_0)$ and reaches minimum for $z = \pi/(2g_0)$. This case is illustrated in Fig. 2.3 When $w_0 < w_{\mathrm{fm}}$ $w(z)$ increases for $0 < z < \pi/(2g_0)$ and reaches maximum for $z = \pi/(2g_0)$. In both of the above-mentioned cases the flat wavefront $(1/R = 0)$ is obtained for $z = \pi/(2g_0)$. As it was mentioned in the previous section the GRIN lens characterised by length (thickness) $L_{QP} = \pi/(2g_0)$ is called the quarter-pitch lens.

2.3 Effective medium theory

The main idea of the effective medium theory (EMT) is that it is possible to describe a nanostructured dielectric material in terms of effective permittivity ϵ_{eff} as long as the feature size of the nanostructure is sufficiently smaller than the wavelength of the considered illumination. Nanostructured GRIN microlenses which are subject of this thesis can be described by an effective medium theory inspired by the basic mixing rule, so-called Maxwell-Garnet formula. This approach is introduced in section 2.3.1.

Next nanostructured birefringent material is considered in section 2.3.2. Such material exhibits a phenomenon called form birefringence. It is caused by suitable arrangement of alternate, subwavelength in thickness layers of isotropic material (Fig. 2.4) unlike bulk birefringence which is caused by an anisotropy on the molecular level. Second-order effective medium theory suggested by Richter et al. allows to describe optical properties of the considered nanostructured birefringent material using the model of homogenous anisotropic medium characterised by two different permittivites for TE and TM polarisation (Fig. 2.4) [6, 7].

2.3.1 First-order effective medium theory

A basic mixing rule which is used in an effective medium theory (EMT) is based on Maxwell-Garnet formula [8]. Originally the Maxwell-Garnet rule has been derived in the electrostatic case for a dielectric mixture where spherical inclusions of permittivity ϵ_i are randomly distributed in the host medium of permittivity ϵ_e. First, let us

formally define the (relative) effective permittivity ϵ_{eff} of the dielectric mixture. It is defined by a relation [8, 9]

$$< \mathbf{D} >= \epsilon_{\text{eff}} \epsilon_0 < \mathbf{E} >, \tag{2.52}$$

where ϵ_0 denotes the vacuum permittivity, $< \mathbf{E} >$ denotes a volume average of the electric field $\mathbf{E}$ and $< \mathbf{D} >$ denotes a volume average of the electric displacement $\mathbf{D}$. The volume average of the electric field might be written as

$$< \mathbf{E} >= f\mathbf{E}_i + (1-f)\mathbf{E}_e, \tag{2.53}$$

where f is a inclusion fill factor equal to a fraction of the volume occupied by the considered spherical inclusions. $\mathbf{E}_i$ and $\mathbf{E}_e$ denote the electric field inside and outside the inclusions respectively. Average electric displacement can be written in analogous manner.

The Maxwell-Garnet mixing formula can be written as [8]

$$\epsilon_{\text{eff}} = \epsilon_e + 3f\epsilon_e \frac{\epsilon_i - \epsilon_e}{\epsilon_i + 2\epsilon_e - f(\epsilon_i - \epsilon_e)}. \tag{2.54}$$

When both permittivities are similar to each other one can use an approximation given by the first order Taylor expansion of formula (2.54). It gives a simple formula for the effective permittivity

$$\epsilon_{\text{eff}} \approx \epsilon_e + f(\epsilon_i - \epsilon_e) \tag{2.55}$$

which means that effective permittivity ϵ_{eff} is approximated by the volume average of the permittivity.

Although the Maxwell-Garnet formula (2.54) and also the simplification of it given by (2.55) has been derived for electrostatic case one can use them for optical fields as well provided the electromagnetic fields may be treated as quasi-static. It is difficult to determine a strict limit of the quasi-static approximation. Generally speaking the quasi-static approximation is valid when the feature size of the nanostructure is sufficiently subwavelength.

In this work it is proposed to calculate effective permittivity distribution inside nGRIN microlenses using formula (2.55). The beam propagates nearly in parallel to the nanorods in the direction of Z axis. The refractive index distribution is independent of z. It is worth noticing that the component of wavevector $\mathbf{k}$ perpendicular to the rods is much smaller than $(2\pi)/\lambda$. It suggests that the effective index approach can work for larger rod diameter than $\lambda/(2\pi)$. This value is given in handbook [8] as a estimated limit of the quasi-static approximation.

Within the frame of the project conducted at Heriot-Watt Uniwersity (HWU), University of Warsaw (UW) and Institute of Electronic Materials Technology (ITME)

it has been shown that in the case of nanostructured GRIN microlenses (fabricated with the modified stack-and-draw technique) considered in chapters 3 and 4 [10, 11, 12] simple formula (2.55) may be used for calculation of the effective refractive index as long as diameter of the single nanorod is about of $\lambda_0/5$ or smaller and the difference between refractive indices of used glasses is not larger than approximately 0.2. Volume average of the permittivity (or the refractive index) has to be calculated locally for a given point which means that fill factor f is calculated for the neighbourhood of the considered point. The size of the neighbourhood is approximately equal to the wavelength.

2.3.2 Second-order effective medium theory

In this section the concept of the effective medium is extended in order to account for the form birefringence of the nanostructured material shown in Fig. 2.4. As has been

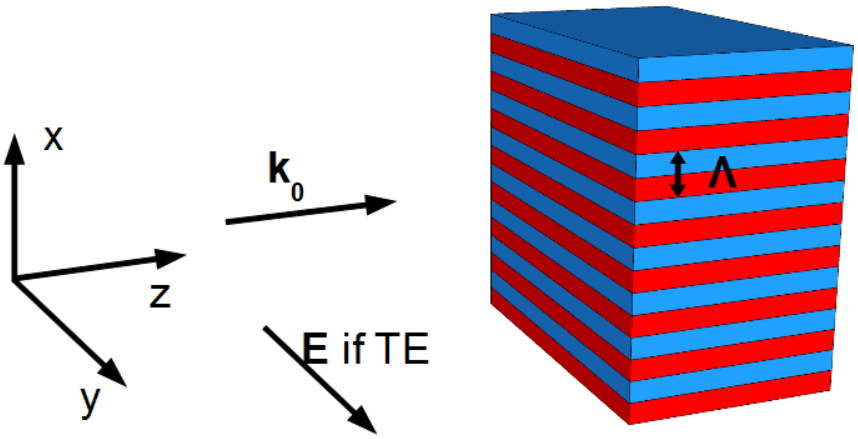

Figure 2.4 – Schematic of the nanostructured birefringent material. A direction of wave vector $\mathbf{k_0}$ of incident illumination is shown. A direction of electric field $\mathbf{E}$ in the case of TE polarisation is also shown.

mentioned in the introduction of section 2.3, the birefringence of the considered nanostructured material is caused by suitable arrangement of alternate, subwavelength in thickness layers of two isotropic dielectric materials. Let us represent permittivities of these isotropic materials by ϵ_i and ϵ_e. The nanostructure is characterised also by its period Λ and the volume filling factor f of the dielectric with the permittivity of ϵ_i. Optical properties of the structure can be effectively described in terms of an anisotropic but continuous and homogenous medium according to the second-order effective medium theory suggested by Richter et al. [7]. According to this EMT model the cosidered nonustructured material can be treated as an uniaxial material with different refractive indices (or permittivities) for TE ($\mathbf{E} \parallel Y$axis) and TM ($\mathbf{H} \parallel Y$axis)

polarisations (Fig. 2.4). The effective refractive indices for TE and TM polarisation $n_{\text{eff}}^{\text{TE}}$ and $n_{\text{eff}}^{\text{TM}}$ respectively are given by [6, 7]

$$n_{\text{eff}}^{\text{TE}} = \sqrt{f\epsilon_i + (1-f)\epsilon_e + \frac{1}{3}\left(\frac{f(1-f)\Lambda\pi}{\lambda_0}\right)^2 (\epsilon_i - \epsilon_e)^2}, \tag{2.56}$$

$$n_{\text{eff}}^{\text{TM}} = \sqrt{\overline{\epsilon} + \frac{1}{3}\left(\frac{f(1-f)\Lambda\pi}{\lambda_0}\right)^2 \left(\frac{1}{\epsilon_i} - \frac{1}{\epsilon_e}\right)^2 (\overline{\epsilon})^3 (f\epsilon_i + (1-f)\epsilon_e)}, \tag{2.57}$$

where

$$\overline{\epsilon} = \frac{\epsilon_i \epsilon_e}{f\epsilon_e + (1-f)\epsilon_i} \tag{2.58}$$

and λ_0 denotes vacuum wavelength.

Richter et al. present in paper [7] results which indicate some inaccuracies of the second-order EMT regarding phase retardation created within the nanostructured birefringent material. However, in this thesis a low contrast nanostructure, with the difference between refractive indices $n_i = \sqrt{\epsilon_i}$ and $n_e = \sqrt{\epsilon_e}$ equal to approximately 0.1, is considered and modelling results presented in chapter 6 show the applicability of the formulae (2.56) and (2.57) in such case.

2.4 Modelling methods

Two modelling methods are utilised in the presented work. One of them is the finite differences in time domain method (FDTD). It is a fully vectorial method based directly on the Maxwell equations. This method is very versatile but also it requires a lot of computer resources.

The fast Fourier transform beam propagation method (FFT-BPM) [5] is the second simulation technique utilised in the presented work. A scalar implementation of FFT-BPM is exploited. The method is based on Helmholtz equation. BPM is much less resource consuming and it can handle much larger structures than FDTD.

In this thesis the FDTD method is used for a verification of the effective medium theory (EMT) in the case of the nanostructured optical elements fabricated with the modified stack-and-draw technique. BPM is used, in turn, for a comparison of a performance of a microlens with a quantised refractive index profile to the performance of the corresponding unquantised microlens.

2.4.1 Finite Differences in Time Domain

In this section general concept of FDTD technique is provided. The method is directly based on two Maxwell equations

$$\nabla \times \mathbf{E} = -\mu \frac{\partial \mathbf{H}}{\partial t} \tag{2.59a}$$

$$\nabla \times \mathbf{H} = \sigma \mathbf{E} + \epsilon \frac{\partial \mathbf{E}}{\partial t} \tag{2.59b}$$

where $\mathbf{E} = [E_x, E_y, E_z]$ is the electric field, $\mathbf{H} = [H_x, H_y, H_z]$ is the magnetic field and ϵ, μ, σ denotes permittivity, permability and electrical conductivity. FDTD requires that initial distribution of the fields is given. This distribution should satisfy two other Maxwell equations. Using Eqs. (2.59) after discretisation the field evolution in time is calculated. It is also possible to implement sources within the computational area. Eqs. (2.59) might be written in cartesian coordinate system as following

$$\frac{\partial H_x}{\partial t} = \frac{1}{\mu}\left(\frac{\partial E_y}{\partial z} - \frac{\partial E_z}{\partial y}\right) \tag{2.60a}$$

$$\frac{\partial H_y}{\partial t} = \frac{1}{\mu}\left(\frac{\partial E_z}{\partial x} - \frac{\partial E_x}{\partial z}\right) \tag{2.60b}$$

$$\frac{\partial H_z}{\partial t} = \frac{1}{\mu}\left(\frac{\partial E_x}{\partial y} - \frac{\partial E_y}{\partial x}\right) \tag{2.60c}$$

$$\frac{\partial E_x}{\partial t} = \frac{1}{\epsilon}\left(\frac{\partial H_z}{\partial y} - \frac{\partial H_y}{\partial z} - \sigma E_x\right) \tag{2.60d}$$

$$\frac{\partial E_y}{\partial t} = \frac{1}{\epsilon}\left(\frac{\partial H_x}{\partial z} - \frac{\partial H_z}{\partial x} - \sigma E_y\right) \tag{2.60e}$$

$$\frac{\partial E_z}{\partial t} = \frac{1}{\epsilon}\left(\frac{\partial H_y}{\partial x} - \frac{\partial H_x}{\partial y} - \sigma E_z\right) \tag{2.60f}$$

FDTD is a finite difference method so the next step is to discretise Eqs (2.60). Hence computational area has to be discretised first. Rectangular Yee lattice [13, 14], shown in Fig. 2.5, is the most basic discretisation scheme. Central difference quotients are used to approximate derivatives.

(i, j, k) denotes $(i\Delta x, j\Delta y, k\Delta z)$, where constants Δx, Δy, Δz are the edge length of Yee cell. $F^n(i, j, k)$ signifies $F(i\Delta x, j\Delta y, k\Delta z, n\Delta t)$. Function F might be every component of the field. Central difference quotients are defined by following formulae

$$\frac{F^n(i,j,k)}{\partial t} = \frac{F^{n+1/2}(i,j,k) - F^{n-1/2}(i,j,k)}{\Delta t} + O((\Delta t)^2) \tag{2.61}$$

$$\frac{F^n(i,j,k)}{\partial x} = \frac{F^n(i+1/2,j,k) - F^n(i-1/2,j,k)}{\Delta x} + O((\Delta x)^2) \tag{2.62}$$

Using these central difference quotients one might discretise Eqs. (2.60). The FDTD method is heavily memory-consuming because a spatial step of discretisation

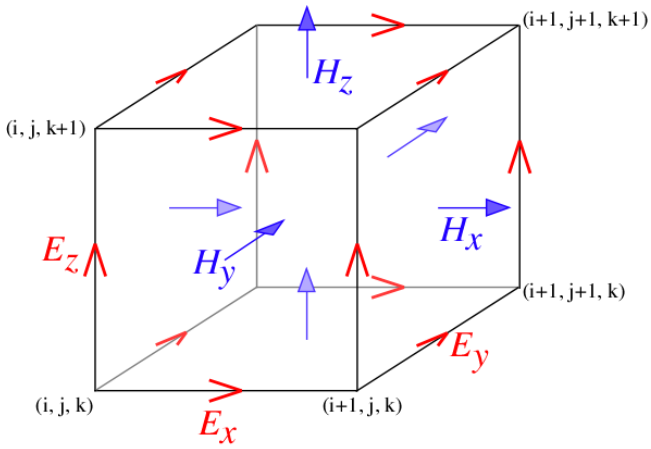

Figure 2.5 – A single cell of the Yee lattice [15].

should be $\lambda/10$ or smaller. Hence it is difficult to simulate big structures with respect to the wavelength. Additionally a time step Δt has to satisfy the stability condition [14]

$$v_{\max}\Delta t \leq \left(\frac{1}{(\Delta x)^2}+\frac{1}{(\Delta y)^2}+\frac{1}{(\Delta z)^2}\right)^{-1/2} \tag{2.63}$$

where $v_{\max}$ denotes a maximum phase velocity. The method is very time-consuming and memory-consuming but on the other hand it very versatile. It results from the fact that the FDTD is based directly on Maxwell equations and therefore it is possible to avoid simplifications.

2.4.2 Beam Propagation Method

Considered in this chapter the beam propagation method (BPM) method can be derived from the scalar Helmholtz equation [5]

$$\frac{\partial^2\psi}{\partial x^2}+\frac{\partial^2\psi}{\partial y^2}+\frac{\partial^2\psi}{\partial z^2}+k_0^2n^2\psi=0, \tag{2.64}$$

where k_0 denotes the wavenumber in vacuum and $n(x,y)$ is the refractive index distribution. A monochromatic wave is considered thus it is assumed that a field component can be expressed by $\psi(x,y,z)\exp(i\omega t)$.

2.4.2.1 BPM in the free space

First let us consider beam propagation in the free space where $n(x,y,z)=n_0$. An approach based on the angular spectrum of plane waves (ASPW) is utilised here. One can express the solution to the Eq. (2.64) in Fourier integral form

$$\psi(x,y,z)=\int_{-\infty}^{\infty}\int_{-\infty}^{\infty}\Psi(\nu_x,\nu_y,z)\exp[i2\pi(\nu_x x+\nu_y y)]d\nu_x\,d\nu_y. \tag{2.65}$$

Expression $\Psi(\nu_x, \nu_y, z)\exp(i2\pi(\nu_x x+\nu_y y))$ might be interpreted as a plane wave characterised by the spatial frequencies ν_x and ν_y. Substitution of Eq. (2.65) into Eq. (2.64) gives the equation for $\Psi(\nu_x, \nu_y, z)$

$$\frac{\partial^2\Psi}{\partial z^2} + \beta^2\Psi(\nu_x, \nu_y, z) = 0, \tag{2.66}$$

where

$$\beta^2 = k_0^2 n_0^2 - 4\pi^2(\nu_x^2 + \nu_y^2). \tag{2.67}$$

A solution of Eq. (2.66) can be expressed as

$$\Psi(\nu_x, \nu_y, z) = \Psi(\nu_x, \nu_y, z_0)\exp[-i\beta(z - z_0)]. \tag{2.68}$$

Let us assume that the field distribution $\psi(x, y, z_0)$ is known at $z = z_0$. One can calculate the spectrum $\Psi(\nu_x, \nu_y, z_0)$ using the Fourier transform

$$\Psi(\nu_x, \nu_y, z_0) = \mathcal{F}\{\psi(x, y, z_0)\} = \int_{-\infty}^{\infty}\int_{-\infty}^{\infty}\psi(x, y, z_0)\exp[-i2\pi(\nu_x x + \nu_y y)]d\nu_x\, d\nu_y. \tag{2.69}$$

Next it is possible to calculate $\Psi(\nu_x, \nu_y, z)$ at any z using Eq. (2.68) and then one can obtain $\psi(x, y, z)$ by the inverse Fourier transform (2.65). The procedure can be described by the equation

$$\psi(x, y, z) = \mathcal{F}^{-1}\{\mathcal{F}\{\psi(x, y, z_0)\}\exp[-i\beta(z - z_0)]\}, \tag{2.70}$$

where $\mathcal{F}\{\}$ denotes the Fourier transform and $\mathcal{F}^{-1}\{\}$ denotes the inverse Fourier transform.

2.4.2.2 BPM in the inhomogeneous medium

Let us consider monochromatic beam propagation in the inhomogeneous medium characterised by the refractive index $n(x, y)$. It is convenient to express complex field $\psi(x, y, z)$ as [5]

$$\psi(x, y, z) = \phi(x, y, z)\exp(-ik_0\bar{n}z) \tag{2.71}$$

where $\bar{n}$ denotes the averaged refractive index in the cross-section of the computational volume. Substituting Eq. (2.71) into Eq. (2.64) leads to

$$\nabla^2\phi - i2k_0\bar{n}\frac{\partial\phi}{\partial z} + k_0^2(n^2 - \bar{n}^2)\phi = 0, \tag{2.72}$$

where

$$\nabla^2 = \frac{\partial^2}{\partial x^2} + \frac{\partial^2}{\partial y^2} + \frac{\partial^2}{\partial z^2}. \tag{2.73}$$

Assuming a low contrast structure one can approximate $(n^2 - \bar{n}^2) \approx 2\bar{n}(n - \bar{n})$. This approximation allows to express Eq. (2.72) as

$$\frac{\partial\phi}{\partial z} = -i\frac{1}{2k_0\bar{n}}\nabla^2\phi - ik_0(n - \bar{n})\phi. \tag{2.74}$$

It is important to notice that the first term of the Eq. (2.74) describes a free space propagation in the medium characterised by refractive index $\bar{n}$. Let us express above-mentioned equation using the operator representation

$$\frac{\partial \phi}{\partial z} = (\mathbf{A} + \mathbf{B})\phi, \tag{2.75}$$

where

$$\mathbf{A} = -i\frac{1}{2k_0\bar{n}}\nabla^2, \tag{2.76}$$

$$\mathbf{B} = -ik_0(n - \bar{n}) \tag{2.77}$$

Formal integration of Eq. (2.75) leads to

$$\phi(x, y, z + h) = \exp[h(\mathbf{A} + \mathbf{B})]\phi(x, y, z). \tag{2.78}$$

Using Barker-Hausdorff theorem [5] and assuming that h is sufficiently small it is possible to approximate

$$\exp(h\mathbf{A} + h\mathbf{B}) = \exp(h\mathbf{B} + h\mathbf{A}) \approx \exp(h\mathbf{B})\exp(h\mathbf{A}) \tag{2.79}$$

Therefore one can express Eq. (2.78) as

$$\phi(x, y, z + h) = \exp(h\mathbf{B})\exp(h\mathbf{A})\phi(x, y, z). \tag{2.80}$$

The term $\exp(h\mathbf{A})$ corresponds to the free space propagation and $\exp(h\mathbf{B})$ is a phase correction term. The second term is related to the medium inhomogeneity. Let us assume that a distribution of $\phi(x, y, z)$ is known for a particular z. In order to calculate $\phi(x, y, z + h)$ when h is small one can propagate ϕ in the free space by the distance h and then apply the phase correction term. This procedure can be expressed using complex field $\psi(x, y, z)$.

1. The free space propagation by the small distance h in the homogenous medium characterised by the refractive index $\bar{n}$. It is given by Eq. (2.70) and Eq. (2.67)

$$\psi_{\text{fs}}(x, y, z + h) = \mathcal{F}^{-1}\{\mathcal{F}\{\psi(x, y, z)\}\exp(-i\beta h)\}. \tag{2.81}$$

2. The phase correction related to the medium inhomogeneity.

$$\psi(x, y, z+h) = \exp(h\mathbf{B})\psi_{\text{fs}}(x, y, z+h) = \exp[-ik_0(n-\bar{n})h]\psi_{\text{fs}}(x, y, z+h) \tag{2.82}$$

One can utilise the described procedure for the numerical computation of the complex field $\psi(x, y, z)$ in the subsequent planes perpendicular to Z axis if the initial field for $z = z_0$ is known. In practice Fourier transforms are realised by the discrete Fourier transform (DFT) using fast Fourier transform (FFT) algorithm

Minimum lateral resolution of the simulation is determined by the sampling theorem [16]. It is sufficient when lateral steps Δx and Δy satisfy the condition

$$\Delta x \leq \lambda_0/(2n_{\max}), \tag{2.83}$$

where $n_{\max}$ denotes a maximum refractive index in the system and λ_0 is the vacuum wavelength. Distance h has to satisfy the condition

$$h \ll \frac{\lambda_0}{2\pi|n-\bar{n}|}. \tag{2.84}$$

2.5 Various methods of the classical GRIN lens fabrication

The concept of the GRIN medium was considered in 1850s when Maxwell designed lens known as fish eye but practical implementation was limited by lack of fabrication technologies for many years [3]. In 1905 Wood constructed a GRIN lens [17, 3] made of gelatin but real development of experimental GRIN optics started in 1970s.

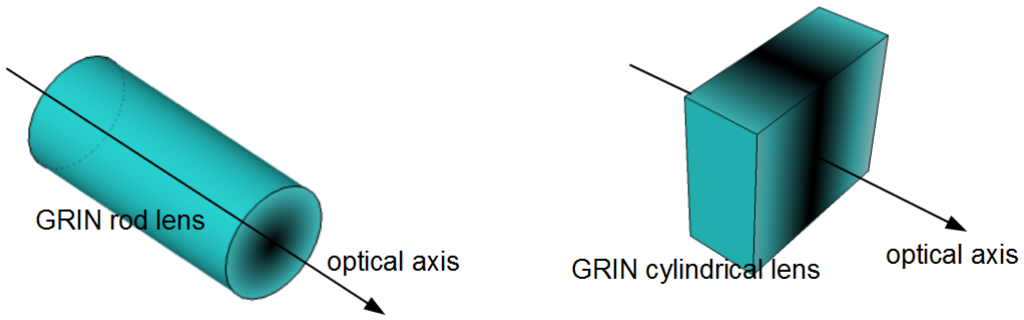

(a) GRIN rod lens (b) cylindrical GRIN lens

Figure 2.6 – Two types of GRIN lenses. Refractive index gradient is illustrated with color.

There are a few possible geometries of GRIN lenses. GRIN rod lenses and cylindrical GRIN lenses are the popular types of GRIN lenses. These two types are shown in Fig. 2.6. Within the GRIN rod lenses refractive index distribution is symmetrical with respect to rotations about an optical axis. Surfaces of constant refractive index are cylinders which have an axis identical with an optical axis [18, 19]. Cylindrical GRIN lens is a glass slab with nearly parabolic distribution in the direction perpendicular to the optical axis. The refractive index is invariant in the direction of the optical axis [20].

2.5.1 Ion exchange technique

The ion exchange technique is the most popular method of GRIN lenses fabrication. It is due to its procedural simplicity [19, 18, 21, 22]. The ion exchange method consists in dipping a piece of glass in molten salt bath. The ion exchange occurs at the glass surface which is cation selective interface. The process happens at high temperature (e.g. 370°C [19]) which is close to transition temperature. Exchanged at the glass surface ions diffuse within the glass. This phenomenon results in different concentration of the exchanged ions at points which are located at different distances from the glass surface. The ion exchange reaction rate depends on the factors such as electrochemical activities between the exchanged ions, strength of bonds of the alkali ions in the used glass and the ion mobility within the glass [19]. It means that the glass composition has to be carefully chosen. The concentration of the ions is directly connected with refractive index. If one can control concentration distribution one can control refractive index distribution within the glass piece. Electromigration is an important modification of the ion exchange technique. In the process of the electromigration the ions are accelerated by the applied electric field. It reduces time of the fabrication and makes the ion exchange technique more cost-effective [23]. Obviously the refractive index distribution depends on the shape of the glass piece. There are a several typical geometries which can be fabricated with the ion exchange technique. One might consider a GRIN cylindrical lens (Fig. 2.6(b)). Such lens is a glass slab with nearly parabolic distribution in the direction perpendicular to the optical axis. The refractive index is invariant in the direction of the optical axis [20]. Utilizing a cylindrical GRIN lens one might transform strongly divergent and asymmetric beam into collimated beam and therefore cylindrical GRIN lenses are used for coupling between laser diodes and optical fibers [20].

It is also possible to fabricate in planar substrate so-called planar GRIN microlenses which have radially symmetrical distribution of the refractive index. Such lenses are described in handbook [23]. The idea of the planar lens fabrication is shown in Fig. 2.7. Radially symmetrical distribution of refractive index is obtained if circular openings in the metal mask are used. Typical maximum penetration depth of the ions within the substrate is of the order of 100μm. When elliptical openings are used it is possible to fabricate astigmatic lenses [24]. Astigmatic planar GRIN lenses are used for transforming an astigmatic and elliptical beam into a nonastigmatic and spherical beam. It is worth noticing that in planar substrate whole 2D array of planar GRIN lenses can be fabricated so such lenses might be easily utilised for optical interconnections [23].

The ion exchange technique is also used for fabrication of GRIN rod microlenses (Fig. 2.6(a)). GRIN rod lenses have a variety of applications. They are utilised for

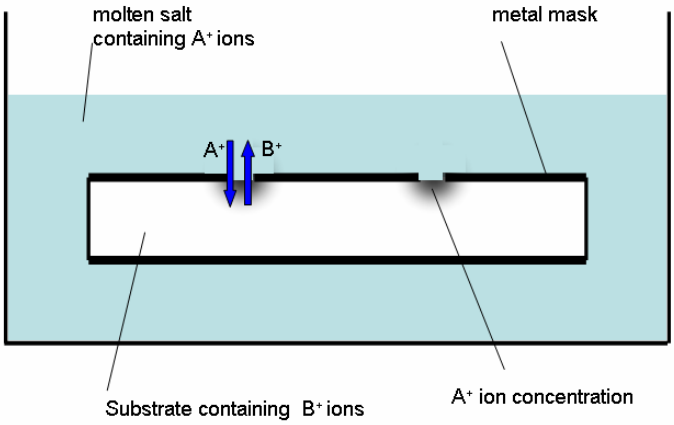

Figure 2.7 – Planar GRIN microlenses fabrication with the ion exchange technique [23]. Typically $A^+ = Ag^+, Tl^+, K^+$ and $B^+ = Na^+$ [23, 24].

fiber coupling and also in copiers, fax machines and compact disc lenses [23, 19]. The example of the GRIN rod fabrication is described in paper [19]. Base glass contains SiO_2, Al_2O_3, TiO_2, Na_2O, Li_2O. Two types of glass NG3A2 and NG3B2 were melted. They are slightly different in composition. After melting, casting, and annealing glass were shaped into glass rods which are 6mm in diameter and 15 to 20mm in length. Then annealing was carried out in order to removal of stresses caused by shaping. Next the rods were dipped into salt bath containing $NaNO_3$. The temperature of molten salt bath was 370°C in case of NG3A2 glass and 400°C in case of NG3B2 glass. Li^+ ions were being exchanged for Na^+ ions from molten salt in order to obtain a negative refractive index profile. It means that there is the highest refractive index in the center of the rod cross-section. After thermal ion exchange process rods were cooled slowly to room temperature. Parameters of the fabrication procedure are shown in Tab. 2.1. Refractive index profiles are presented in Fig. 2.8.

Glass No.	Exchange duration	Exchange temp.
NG3A2-S01	50 h	370°C
NG3A2-S02	100 h	370°C
NG3A2-S03	150 h	370°C
NG3B2-S01	50 h	400°C
NG3B2-S02	100 h	400°C
NG3B2-S03	150 h	400°C

Table 2.1 – Ion exchange parameters [19].

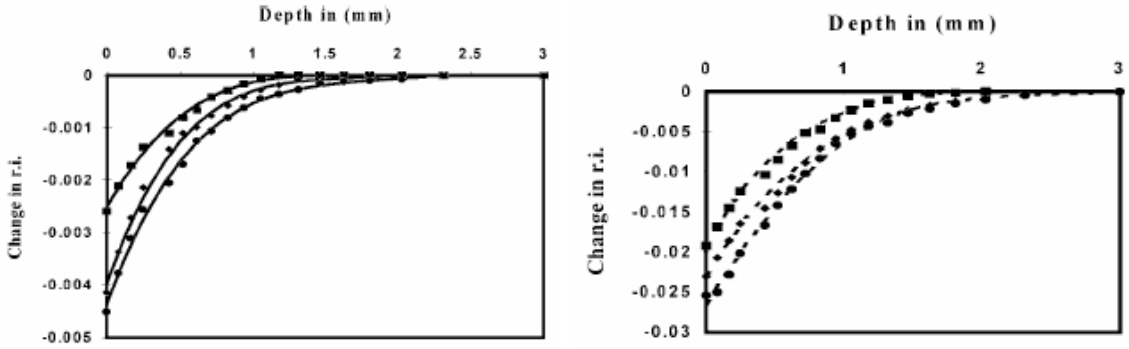

(a) NG3A2 (b) NG3B2

Figure 2.8 – Refractive index profiles within fabricated GRIN rod lenses [19]

2.5.2 Chemical vapor deposition

Chemical vapor deposition (CVD) is another technique used for fabrication of GRIN lenses [18]. This technique is also widely used for fabrication of GRIN fibers. The method consist in deposition layers of glass materials inside or outside a tube. Every glass material has a slightly different composition and refractive index. Some step refractive index profile is created inside or outside the glass tube and this tube is the preform for fiber drawing. Next the preform is drawn in order to obtain a target diameter of the fabricated fiber. The preform diameter is of the order of 1cm and the final fiber diameter is of the order of 100μm. Thickness of single glass layer becomes subwavelength and refractive index profile appears to be continuous. Fiber might be cut into short pieces which can act as GRIN rod lenses. CVD technique is limited to the fabrication of the GRIN lenses with refractive index distribution symmetrical with respect to the rotation about the optical axis.

In paper [25] microprobes for low-coherence interferometry are presented. A simple microprobe consists of single mod fiber (SMF) and GRIN fiber lens fabricated with modified chemical vapor deposition (MCVD). Fusion splicing of these two elements provides automatic alignment. Described GRIN fiber lenses have nearly parabolic negative refractive index profile and they have an outer diameter in the range $100 - 130\mu$m and a GRIN fibre core diameter of $70 - 125\mu$m. The magnitude of refractive index change Δn is of the order of 0.015. Small Δn results in relatively long GRIN fibre lenses. The small diameter of the GRIN fiber lenses is important when microprobe is used for invasive imaging within solid tissue. Reported microprobes were utilised for measuring microscopic brain motions with low-coherence interferometry.

2.5.3 Direct writing in a diffusion-driven photopolymer

In paper [26] Ye and McLeod presented a new method of polymer GRIN lens fabrication. The method consist in exposing photopolymer to a low-power CW laser. Direct writing fabrication set-up is shown in Fig. 2.9. A photopolymer sample is 1 mm

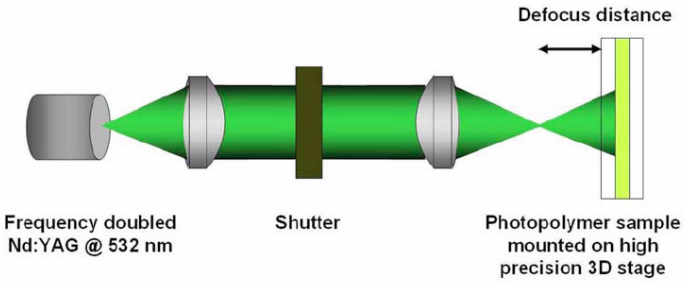

Figure 2.9 – Direct writing setup for GRIN lens fabrication presented in paper [26].

thick photopolymer layer located between two glass slides. The sample is mounted on the precise 3D translation stage. The writing beam size at the sample can be easily changed by moving the sample in the direction of the optical axis. Illumination results in polymerisation and monomer diffusion to the exposed region. This in turn causes increase in refractive index. Desired refractive index profile is created by changing the size and power of the writing beam and also exposure time. Approximately index change is proportional to $I^{\alpha}t$ where I is intensity , t is exposure time and α depends on the composition of the photopolymer. After direct writing with the laser beam the sample is exposed to uniform light. It makes the lens insensitive to light. An example of the fabricated refractive index profile is shown in Fig. 2.10 It is possible to produce GRIN lens which are 40 to 1000μm in diameter. The magnitude of refractive index change is of the order of 0.001. The method is suitable for fabrication lenslet arrays and might be used for cheap and fast prototyping.

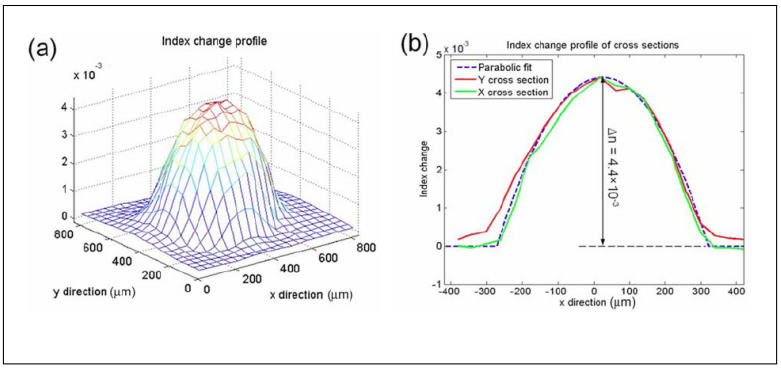

Figure 2.10 – Refractive index profile of the fabricated lens presented in paper [26].

2.5.4 Copolymerisation

It is also possible to fabricate very large GRIN lenses which are promising candidate for eyeglasses lenses [27]. Copolymerisation technique is utilised in order to obtain such lenses. This technique is based on the fact that refractive index of the copolymer depends on the volume fraction of each monomer. Change in copolymer composition means change in refractive index. In paper [27] Wu et. al. reported fabrication of lenses which are 70mm in diameter and have magnitude of refractive index change Δn greater then 0.02.

There are also other fabrication techniques such as neutron irradiation, ion stuffing and crystal growing [3, 18].

Chapter 3

Nanostructured GRIN microlenses: concept and fabrication

Some concepts of the nanostructured GRIN optical elements proposed by other research groups are described in section 3.1. Next the novel concept of nanostructured GRIN microlenses fabricated with a modified stack-and-draw technique is presented.

The present chapter concerns mainly so-called small-diameter nanostructured GRIN microlenses. An array of such small-diameter nGRIN microlenses consists of assemblies of parallel subwavelength diameter glass rods. [10, 12, 11] There are two types of these glass nanorods, each of them charactarised by a different refractive index. A single nGRIN microlens is shown in Fig. 3.2. The nanorods are strongly subwavelength, hence the principle of operation of nGRIN microlenses may be explained by effective medium theory (EMT) [8]. This approach is discussed in details in section 2.3.1 of chapter 2 and also it is applied in section 3.2.2. The idea of so-called large-diameter quantised nanostructured GRIN microlenses is mentioned in section 3.2 but the detailed description of the large-diameter nanostructured microlenses fabricated with the modified stack-and-draw technique is provided in chapter 5

3.1 Nanostructured GRIN optical elements described in literature by other research groups

Elements described in this section are nanostructured optical elements proposed from the literature which can act as GRIN lenses [28, 29, 30]. Nonuniform 2D photonic crystals are an example of such structures. The concept of nonuniform photonic crystals refers to the ordinary photonic crystals (PhCs) [31] but in the nonuniform photonic crystals some PhC parameter e.g. lattice period or filling factor is varied. To describe such structures the name graded (index) photonic crystal was introduced by E. Centeno and D. Cassagne in 2005 [28]. These structures, when the lattice period is sufficiently subwavelength, can be described by the effective medium theory and

effective refractive index distribution. The light focusing ability of the graded index photonic crystals (GRIN PhCs) is shown in papers [29, 30]. H. Kurt et. al. proposed GRIN photonic crystal with varied lattice period [29].There is no fundamental length scale in the Maxwell's equations and one can say that Maxwell's equations are scale invariant [31]. That is why it is possible to use the microwave regime for investigation of optical phenomena. Taking advantage of this fact H. Kurt et. al. implemented the proposed GRIN PhC for the experiment in the microwave regime. Additionally the finite difference time domain method (FDTD) has been utilised for a simulation of the focusing phenomenon The structure consists of aluminium rods, which are sub-wavelength in diameter, placed in an air background. Aluminium can be considered a dielectric material in the microwave regime. The filling factor is highest at the centre of the element (Fig. 3.1a). Such a GRIN PC is able to focus a wide Gaussian beam as is shown in Fig. 3.1b. The focusing occurring in the GRIN photonic crystal can

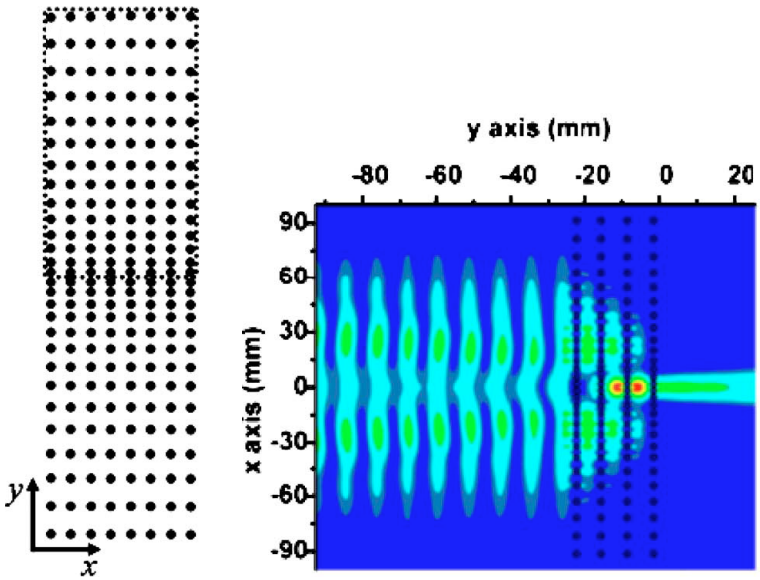

(a) (b)

Figure 3.1 – Schematic of the GRIN PhC [29](a). Focusing of the Gaussian beam by GRIN PhC [29]. Electric field distribution obtained with FDTD method is shown (b).

be explained by the effective medium theory and the notion of the effective refractive index which is higher in the center of the structure than at the sides.

A different approach to obtaining a gradient of the effective refractive index in the GRIN PhC has been presented by C. Tan et. al. in the paper [30]. The described GRIN PhC lens can be fabricated using laser interference lithography (LIL). The structure consists of rods which are arranged in a square array. The rods have varied diameters from 228nm in the centre to 70nm at the sides. During the fabrication four laser beams are utilised. These beams create interference pattern in the recording material. After the lithographic procedure there is a different refractive index in the

spots where the interference intensity is higher than a certain threshold of the material compared to the refractive index in the volume of the material where the recording interference intensity is lower than the threshold.

GRIN PhCs can be made using semiconductor fabrication technologies. These techniques allow the creation of very fine features with a critical dimension of a few tens of nanometres. This is important when one wants to produce effective medium materials with subwavelength feature sizes. An example of such a technique is a direct-write electron-beam lithography combined with dry reactive-ion plasma etching [32].

3.2 Nanostructured GRIN microlenses fabricated with the stack-and-draw technique

In this work a new concept of the nanostructured GRIN (nGRIN) microlenses is discussed [10, 12, 11]. The concept is based on the standard stack-and-draw technique widely used for photonic crystal fibre development [33, 34, 35]. These nanostructured microlenses, whose operation can be explained by the effective medium theory [8], consist of many subwavelength diameter nanorods. The nanorods are arranged parallel to each other. Each nanostructured nGRIN microlens is composed of two types of nanorods characterised by different refractive indices and similar mechanical and thermal properties. An illustrative scheme of the spatial nanostructure of the nGRIN microlens and refractive index distribution in the cross-section of the typical nGRIN microlens are presented in Fig. 3.2. The individual glass rods in the fabricated mi-

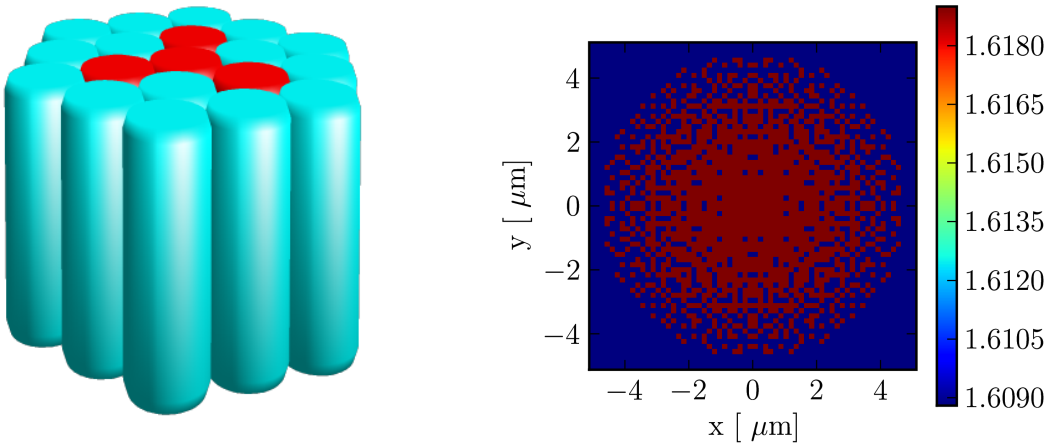

(a) (b)

Figure 3.2 – An illustrative scheme of the spacial nanostructure of the nGRIN microlens and refractive index distribution in the cross-section of the typical nGRIN microlens

crolenses have diameters (typically 100-200nm) much less than the wavelength of the

incident light and can therefore be described using an effective medium theory averaged refractive index distribution (see section 2.3.1). In order to obtain the effective refractive index at a given point within the microlens, assuming no absorption by the constituent glasses, one simply calculates a volume average of the refractive index within the immediate neighbourhood of that point. The diameter of this neighbourhood is typically around one wavelength and the experimental and modelling results presented in [10, 12, 11] show that this approximation is valid for the nanorod diameters under consideration here.

Described in this work nGRIN microlenses have a few attractive advantages compared to the GRIN microlenses fabricated with the traditional techniques mentioned in section 2.5. It is possible to obtain a very high (up to $\Delta n = 0.1$ per 5μm) gradient of the effective refractive index compared to that attained by standard GRIN fabrication techniques ($\Delta n \sim 0.1$ per 250μm) [36]. This large gradient value led to the successful fabrication of nanostructured microlenses with f-numbers equal to one. The stack-and-draw technology allows the straightforward creation of 2D arrays of nanostructured microlenses with, for example, a pitch compatible with the standard pitch of 2D Vertical Cavity Surface Emitting Laser (VCSEL) arrays. Moreover the nanostructuring technology makes possible the fabrication of aspheric and other more exotic refractive index distributions.

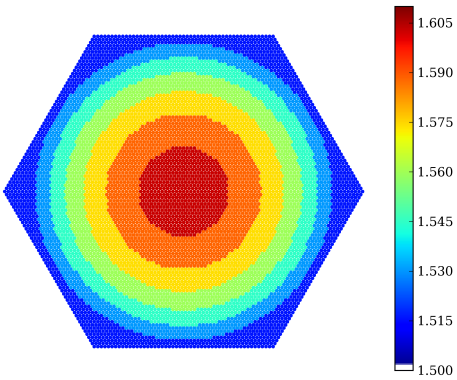

Figure 3.3 – Cross-section of the large diameter nanostructured microlens with the quantised gradient index profile. The colourbar describes the effective refractive index for vacuum wavelength 1μm.

The basic concept of the nGRIN microlens illustrated in Fig. 3.2 limits in practice a diameter of the nGRIN microlenses to $20 - 30\mu$m. This is due to difficulties in stacking the preform which consists of more than 10000 rods. The fabrication procedure is explained in detail in subsection 3.2.1. The need to make also larger diameter microlenses with the stack-and-draw technique was the inspiration for modifying the original concept of the nGRIN microlens. The modified concept allows fabrication

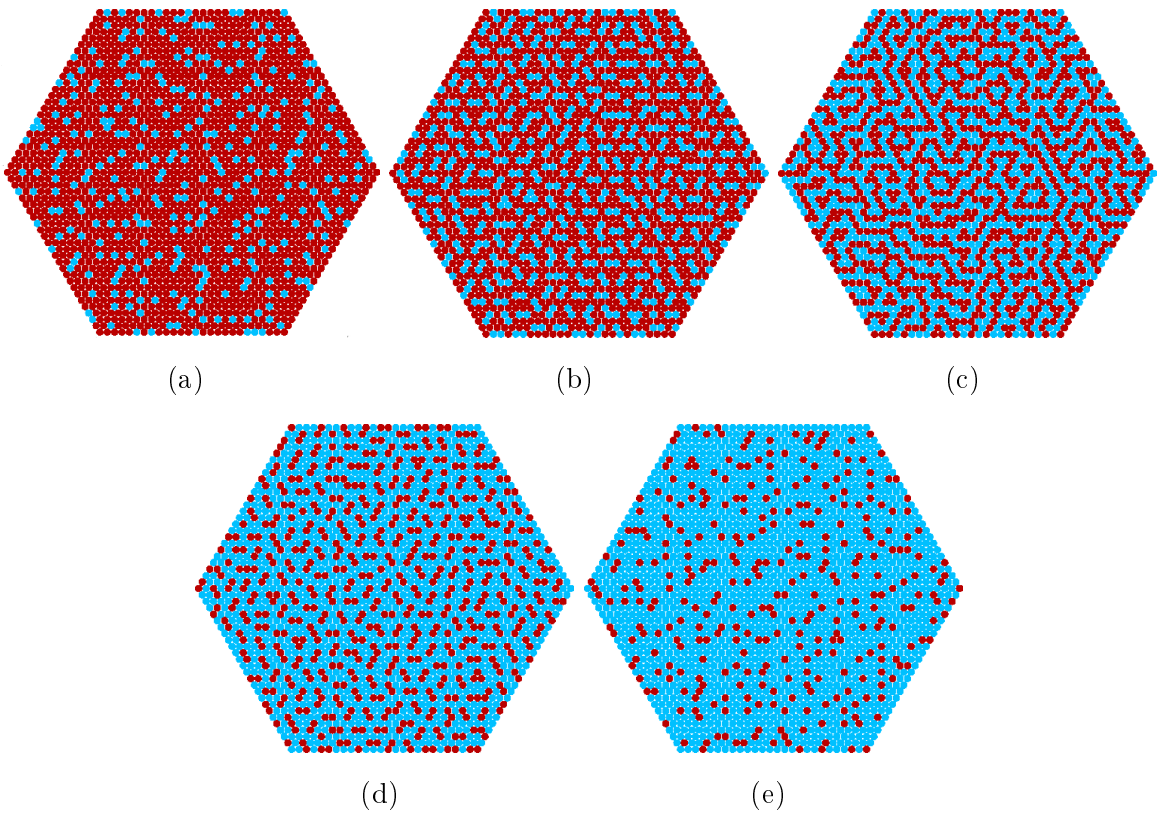

Figure 3.4 – Cross-sections of different nanostructured metarods characterised by different effective refractive indices. Red color and blue color denote high and low refractive index glass respectively.

of large diameter nanostructured microlenses characterised by a quantised gradient index profile (Fig. 3.3) [37]. The idea of these large-diameter microlenses is based on nanostructured metarods which are shown in Fig. 3.4. Each type of metarod is utilised to create one level of the effective refractive index in the quantised gradient index profile of the considered microlenses. It has been experimentally shown in [37] that it is possible to attain the microlens diameter of 100μm for optical wavelength. Further information about these large-diameter microlenses can be found in chapter 5.

3.2.1 Fabrication of small-diameter nGRIN microlenses

The nGRIN microlens array fabrication process exploits the well-known stack-and-draw method [38, 39, 40, 33].

The standard stack-and-draw technique is widely used for fabrication of photonic crystal fibres (PCFs). Many PCFs belong to one of two broad categories - holey fibres (HF) and all-solid fibres [39]. Holey fibres are usually made of a single material (e.g. glass) and they have a regular pattern of holes in their cross-section. (Effectively one obtains an air-glass PCF.) This approach has a few important advantages. It naturally provides relatively high refractive index contrast which is convenient when a photonic

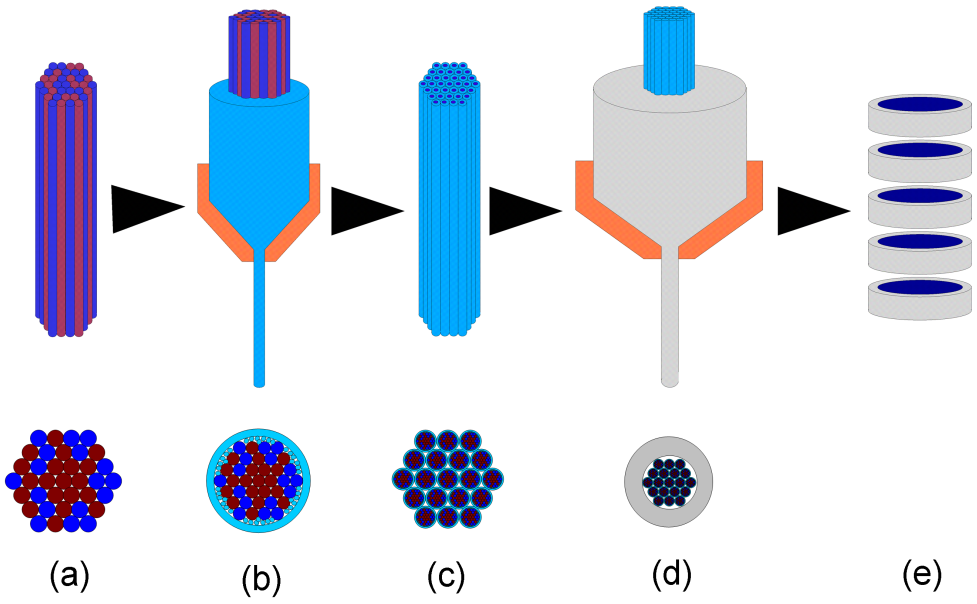

Figure 3.5 – Schematic of the procedure allowing the fabrication of small-diameter nGRIN microlens arrays.

bandgap is desired [38]. Moreover the problems concerning chemical, mechanical and thermal matching of materials are eliminated due to the fact that only one material is utilised. On the other hand there is also some cost of such a solution. It is much more difficult to avoid distortions when holey structures are fabricated. One has to control the air pressure inside the holes during the drawing process, also surface tension can cause problems.

The drawing process in case of the all-solid structure is much easier to realise provided the utilised pair of glasses are properly matched in terms of chemical, mechanical and thermal properties. For a proper pair of glasses there has to a temperature such that the viscosities of both glasses are similar. Choice of a suitable pair of glasses is discussed further in section 3.2.1.3.

Fabrication of the nGRIN microlenses and fabrication of the microstructured fibers are based on the same principle however there are a few significant differences. First of all, the final feature size of the structure is much smaller in the case of nGRIN microlenses compared to a typical PCF. Another difference is the relatively small refractive index contrast between the utilised materials. The diameter of the small-diameter nGRIN microlenses is smaller than 30μm, hence a large refractive index contrast is not needed. For these reasons nGRIN microlenses presented in this thesis are all-solid elements [10, 41, 11, 12]. The third difference between nGRIN microlenses and PCF fabrication is that the nGRIN microlens fabrication requires much more rods (up to 10 thousand) to be stacked together in order to form an initial preform. The last difference is quite obvious - after final drawing the obtained rod is cut into thin

slices. Each slice contains a single nGRIN microlens or an array of such microlenses.

The process of nGRIN microlenses fabrication is comprised of the following steps [10, 11]. Firstly two types of glass, characterised by different refractive indices and similar mechanical and thermal properties, are cast as long rectangular bars which are then cut, ground and polished to obtain rods with a round or rectangular cross-section. These rods are then scaled down, using a fibre drawing tower, to a diameter of $0.6 - 1$mm. Several thousand of these rods are then stacked into an initial preform according to the designed rod distribution (Fig. 3.5a) and this preform is drawn-down at a relatively high temperature ($600 - 700^0C$) (Fig. 3.5b). The drawn-down rods obtained from this stage are cut and re-stacked into an intermediate preform (Fig. 3.5c) which is drawn-down again (Fig. 3.5d). The re-stacking and draw-down stages presented in Fig. 3.5c can be repeated multiple times until the desired final nanorod diameter is achieved. Each draw-down stage scales the cross-section diameter of the structure down by a factor of 10-30. Finally, once the individual nanorod diameter is in the 100-200nm range, the fabricated nanostructured rod is cut into slices, typically about 100μm thick, each of which contains an identical array of nGRIN microlenses. The slices are very thin, hence it is feasible to produce thousands of microlens arrays based on the same initial preform. It should be noted that it is possible to fabricate both rectangular- and hexagonal-packed arrays of microlenses by a suitable choice of rod cross-sectional shape during the initial preform assembly.

3.2.1.1 Description of the draw tower

The draw tower is an essential piece of equipment for the fabrication of the nanostructured GRIN microlenses. It is needed in order to realise the drawing process. A photograph of the draw tower is shown in Fig 3.6. The main part of the tower is the furnace (Fig. 3.7b) where the diameter of the drawn preform is reduced at high temperature. A preform is placed in a shaft inside the furnace. The volume of the shaft can be heated up to 1000°C and the temperature is measured by the thermocouple. The draw tower has to provide a very accurate control over the preform feed rate (Fig. 3.7a) and also the speed of the output rod pulling by the tractor assembly (Fig. 3.7c). There are three main parameters of the drawing process which can be controlled by means of the draw tower. These are the temperature of the furnace, the preform feed rate and the pulling speed. These three parameters have to be carefully set in order to obtain the desired diameter of the output rod. This diameter is measured in real time by a laser micrometer (Fig. 3.7b). The further details concerning control over the drawing process are presented in section 3.2.1.3

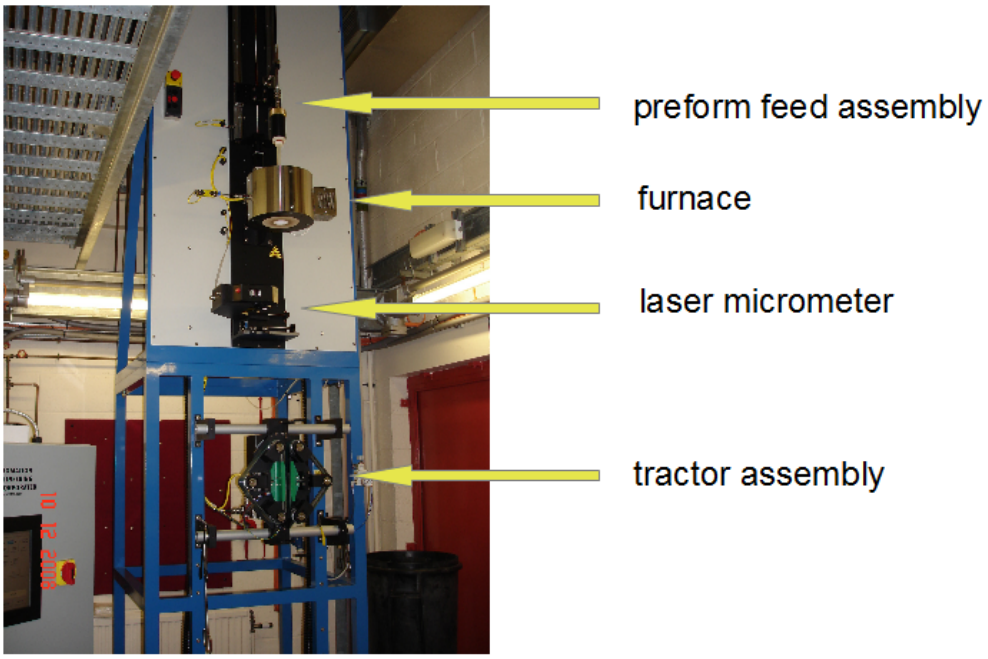

Figure 3.6 – Photo of the draw tower at Heriot-Watt University

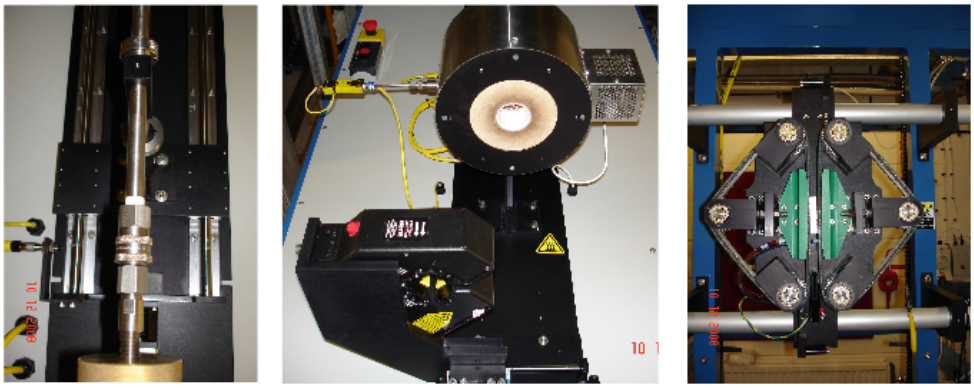

Figure 3.7 – Main parts of the draw tower. Preform feed assembly (a), furnace and laser micrometer (b) and tractor assembly (c)

3.2.1.2 Preform assembly

Assembly of the preform, especially the initial preform, is a critical stage in the fabrication of the nanostructured GRIN microlenses. Stacking the initial preform is also the most labour intensive stage of the fabrication. A few thousands glass rods have to be stacked together according to the designed pattern (Fig. 3.5a). Currently this task is realised manually, although an automatic stacking system has been shown to be possible. A special stacking holder is utilised for assembling the preform. Such

holder is shown in Fig. 3.8.

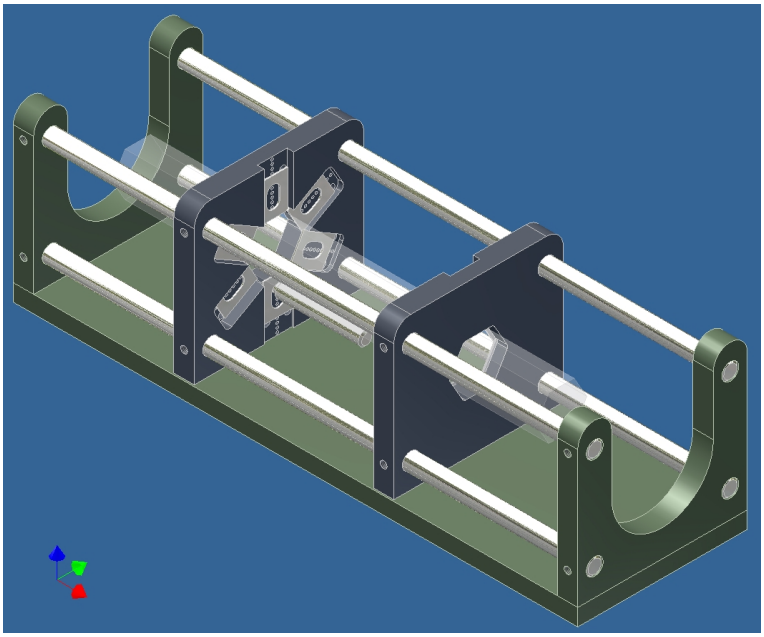

Figure 3.8 – Schematic of a stacking holder.

One of the main challenges faced during assembly of the preform is to build a regular structure out of glass rods despite the fact that in practice these rods are not perfectly uniform and identical in terms of their diameter. Another difficulty is to bind together the rods once they are stacked. It is possible to use a fire-proof adhesive but only at the end of the preform which is above the usable part of this preform during the drawing process. This constraint is related to the fact that impurities are sucked upward inside the shaft of the furnace. The other end of the preform has to be bound without the use of any adhesive. Usually a metal clamp is used for this purpose. The clamp has to be well-fitting in order to provide a rigid assembly.

3.2.1.3 Drawing process

In the introduction to this section (3.2.1) it has been explained why nGRIN microlenses are all-solid structures. Appropriate choice of a pair glasses is a necessary condition for a successful drawing.

When the temperature of the glass is gradually increased it also gradually softens. Dependence of the viscosity on temperature is a key relation if one wants to choose a pair of glasses which can be drawn together. For a proper pair of glasses there has to a temperature such that the viscosities of both glasses are similar. The glass viscosity at such a working temperature needs to be low enough to enable drawing without breaking of the glass structure but at the same time it has to be high enough to preserve a pattern of the structure without significant distortions. Adjusting the furnace

temperature which provides optimal viscosity in terms of sustaining a drawing process and preservation of the glass structure is a critical task during nGRIN microlenses fabrication. Microlenses described in this thesis are made of so-called soft multicomponent glasses. F2 glass made by Schott AG and NC21A glass made by Institute of Electronic Materials Technology (ITME) are examples of such materials. Their working temperatures are around 700°C. The drawing process, after some period of parameter adjustment should be as stable as possible – a steady state process is the ideal case. This is important if repeatability is to be achieved. As was mentioned in section 3.2.1.1, the furnace temperature, the preform feed rate and the pulling speed are the main parameters adjusted during drawing. The relation between the feed rate and the pulling speed determines the scaling factor of the drawing process. The scaling factor, in turn, determines the diameter of the output rod.

To summarise – the two main challenges in the realisation of the drawing is to obtain the desired diameter of the output rod (structure) and also to avoid distortions in the obtained structure. Example photos of the intermediate structures, which still need to be scaled down, are shown in Fig. 3.9.

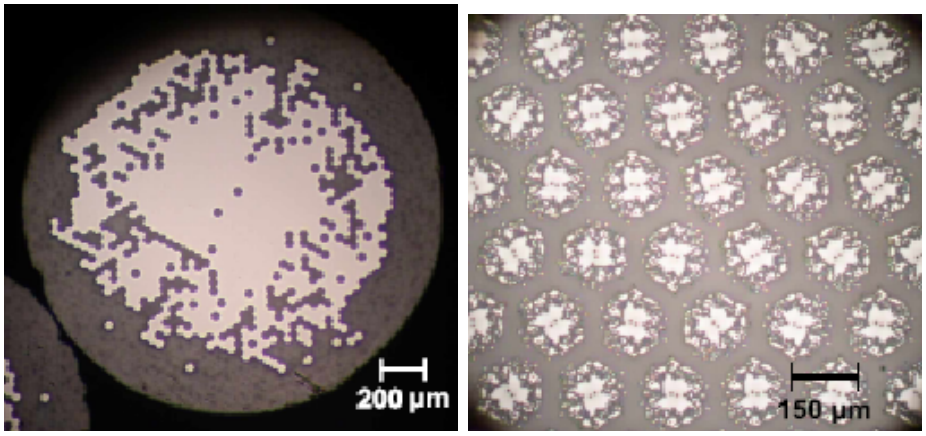

(a) (b)

Figure 3.9 – Example photos of intermediate structures. An intermediate structure obtained by initial preform drawing is shown in (a). Photo (b) presents successive, intermediate structure obtained after restacking and another drawing. It corresponds to an array of microlenses. The structures were made in Institute of Electronic Materials Technology (ITME) by Dariusz Pysz and his team.

3.2.2 Design of the nanorod distribution

A nanostructured GRIN microlens consists of many subwavelength (in diameter) glass nanorods. As has been described previously, the rods are parallel to each other and there are two types of these rods. Each type of rod has a different refractive index.

If the rod diameter is sufficiently small in comparison to the wavelength, the optical properties of such a nanostructured lens can be explained by the effective medium theory (EMT) presented in section 2.3.1. Introduced in the EMT concepts of the effective permittivity and the effective refractive index have been explained in the previous chapter. The aim of the design procedure is to find an arrangement of rods which gives the desired continuous distribution of the effective refractive index. Then the nanostructured lens works like a classical GRIN lens which has continuous refractive index distribution. In the following analysis simple averaging of the permittivity in the neighbourhood area is used for calculating the effective permittivity. The effective refractive index n_{eff} is given, in turn, by the relation $n_{\text{eff}} = \sqrt{\epsilon_{\text{eff}}}$, where ϵ_{eff} denotes effective permittivity.

3.2.2.1 Description of the design algorithm

Direct analytical or numerical calculation of the rod arrangement corresponding to the desired distribution of the effective refractive index is not possible, hence a stochastic optimization method called simulated annealing (SA) is utilised [42]. The SA method belongs to the family of Monte Carlo methods. This class of algorithms is useful when there is an optimisation problem with a large number of degrees of freedom. In the case of the nanostructured microlens the refractive index of each rod may be thought of as one degree of freedom. The inspiration for simulated annealing in the field of numerical algorithms comes from metallurgy. In metallurgy, metals are treated with subsequent heating and cooling in order to eliminate defects in a crystal structure of the material. When a material is heated atoms in dislocations gain sufficient energy to change position. This can lead to elimination of the defects during subsequent cooling. In the field of numerical algorithms, it corresponds to the problem when a global minimum of some energy function (also known as a cost function) has to be found. Some energy value E is assigned to the each state S of the system. In this manner some function $E = H(S)$ is defined for a particular problem. Function $H(S)$ is called the energy function or the cost function. Generally the cost function might have some local minima apart from the global minimum. Theoretically simulated annealing algorithm is able to find a global minimum of the cost function for a given finite problem but infinite time is required. In practice, obviously, time is always limited and there is no guarantee to find a global minimum in the strict sense. However one can hope for a good approximation of the optimal solution provided an efficient cooling protocol is chosen. The flowchart describing the SA method is presented in Fig. 3.10. First some initial state S of the system is chosen. It can be random. Next a random trial state S' is generated. If $H(S') \leq H(S)$ the trial state S' is accepted as a subsequent state ($S := S'$). Otherwise probability of the acceptance

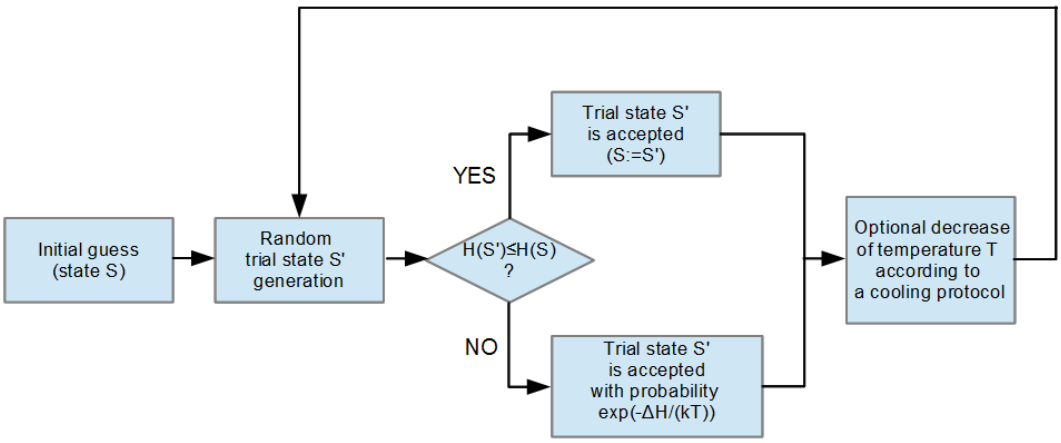

Figure 3.10 – The flowchart describing simulated annealing method.

is given by transition rate $w(S \to S')$ which was proposed by Metropolis et. al. [43]

$$w(S \to S') = \exp\left[\frac{-(H(S') - H(S))}{kT}\right], \tag{3.1}$$

where k is constant and parameter T corresponds to the temperature. Then a new trial state is generated randomly and the step described above is repeated. During the procedure parameter T is decreased gradually according to a chosen cooling protocol.

The cost function $H(S)$ corresponds to the energy and the parameter T to the temperature. If $T > 0$ a trial state with higher energy than the last state of the sequence may be accepted with probability $w(S \to S')$. This fact prevents the system from stopping in a local minimum of the cost function. If the constant T is used, the probability that state S occurs as the m-th element of the sequence (when $m \to \infty$) is given by Boltzmann distribution [42]

$$P_{eq}(S) = \lim_{m\to\infty} P_m(S) = \frac{1}{Z}\exp\left(\frac{-H(S)}{kT}\right) \tag{3.2}$$

It is easy to see that the lower is energy $H(S)$ the higher is probability $P_{eq}(S)$. The idea of the SA method is to approach equilibrium of the system for lower and lower temperature T. An intuitive interpretation of the simulated annealing is that a rough search at the beginning (high T) is followed by a fine search at the end of the procedure ($T \to 0$).

The simulated annealing method is used for optimisation of the rod arrangement in the nanostructured microlens. A value of the refractive index within the lens is independent of the z coordinate and therefore the design problem is limited to the cross-section of the lens. The cross-section is the XY plane perpendicular to the rods.

A particular nanorods arrangement might be treated as a single state S of the system. There are two types of nanorods characterised by two different refractive indices. A new trial state S' is generated by changing a refractive index of the random rod.

Every possible rod arrangement gives a certain profile of the effective refractive index. A cost function $H(S)$ is introduced in order to measure difference between the effective refractive index distribution and the ideal (target) refractive index distribution. A following cost function is proposed

$$H(S) = \sum_{i,j} |n_{\text{eff}}(x_i, y_j) - n_{\text{ideal}}(x_i, y_j)| \tag{3.3}$$

In the sum (3.3) terms related to all pixels (rods) are included. The goal of the optimisation algorithm is to minimise the cost function $H(S)$ given by formula (3.3). It is easy to see that if the value of $H(S)$ is close to 0, then the effective refractive distribution $n_{\text{eff}}(x, y)$ is similar to the ideal (target) refractive index distribution $n_{\text{ideal}}(x, y)$.

The method starts with certain $T_1 > 0$ and a large number of steps (~ 100000) is performed for this temperature. Next a lower temperature $T_2 < T_1$ is set and a large number of steps are performed again. This procedure is repeated for over a hundred decreasing values of temperature. Finally the temperature is set to be 0 and also a large number of transitions are performed.

An example of a target (ideal) refractive index distribution is shown in Fig. 3.11. The corresponding optimised distribution of nanorods inside the nGRIN microlens and the resulting effective refractive index distribution is presented in Fig. 3.12. One might see that the presented nanorods distribution is a square-lattice array of 50 by 50 nanorods. Such a number of nanorods is a practical minimum for decent performance of the lens. Obviously the more rods the better a distribution of effective refractive index is possible. In practice it is feasible to stack manually a structure consisting of 100x100 rods.

3.2.2.2 Exploitation of the design algorithm

The optimisation algorithm, based on the simulated annealing (SA) method, has been used for designing of the small-diameter nanostructured GRIN microlenses which are investigated numerically in chapter 4.

Additionally, the same agorithm has been utilised for designing of nanorod arrangements within metarods. As it is described in detail in chapter 5, the metarods are used for constructing large-diameter quantised nGRIN microlenses. In the case of such quantised microlenses, the effective refractive index distribution within a single metarod is optimised to be uniform (see section 5.2).

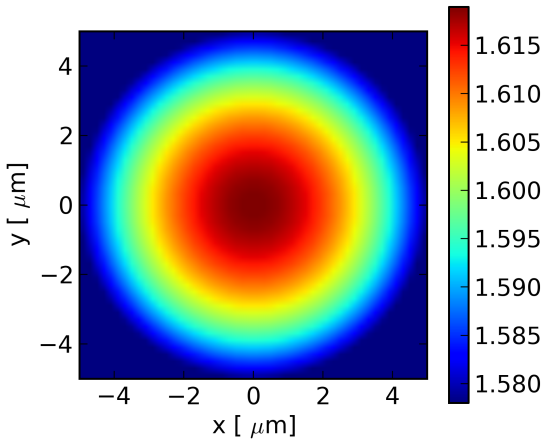

Figure 3.11 – Example of an ideal (target) refractive index distribution in the cross-section of the GRIN microlens.

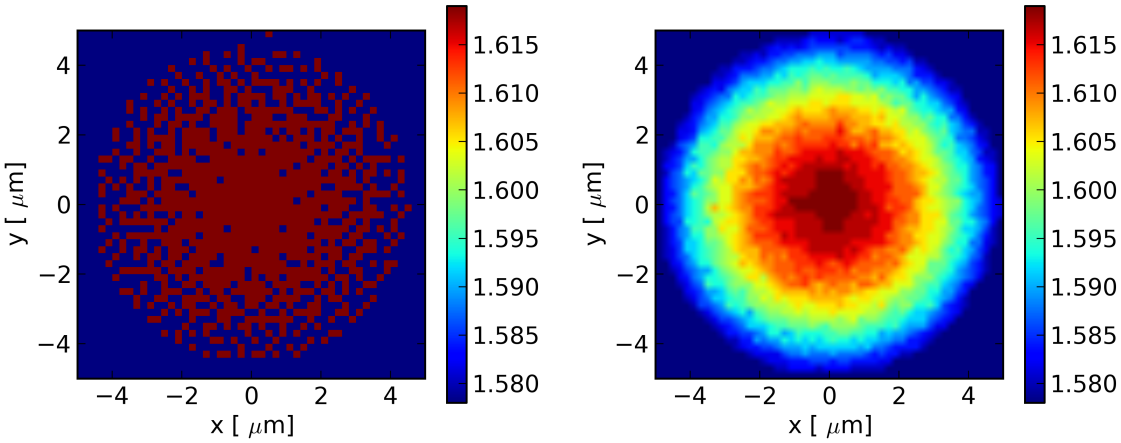

(a) (b)

Figure 3.12 – Example of nanorods arrangement inside nGRIN microlens (a) and the corresponding effective refractive index distribution (b).

Chapter 4

Propagation of Gaussian beam in small-diameter nGRIN microlenses

In this chapter the propagation of Gaussian beam through small-diameter nGRIN microlenses is investigated. The consideration of this problem is motivated by the fact that a Gaussian beam profile is a good approximation to the beams generated by the most lasers. An understanding of the phenomenon of Gaussian beam propagation through the nGRIN microlenses allows to make practical devices using lasers.

The phenomena of Gaussian beam focusing and collimation are discussed in sections 4.1 and 4.2. The results described in section 4.1 have been published in papers [11, 41].

The concept and fabrication of the small-diameter nanostructured GRIN (nGRIN) microlenses has been presented in section 3.2 of chapter 3. nGRIN microlenses are fabricated with a modified stack-and-draw technique. It is possible to obtain a very high (up to $\Delta n \sim 0.1$ per 5μm) gradient of the effective refractive index compared to that attained by standard GRIN fabrication techniques ($\Delta n \sim 0.1$ per 250μm) [36]. This large gradient value has made it possible to successfully fabricate nanostructured microlenses with f-numbers equal to one. The stack-and-draw technology allows the straightforward creation of 2D arrays of nGRIN microlenses with, for example, a pitch compatible with the standard pitch of 2D Vertical Cavity Surface Emitting Laser (VCSEL) arrays. Integration with other optical components is facilitated due to flat input and output facets of the nGRIN microlens array and also due to its small thickness (about 100μm) Moreover the nanostructuring technology makes possible the fabrication of aspheric and other more exotic refractive index distributions [11].

4.1 Nanostructured GRIN microlenses for Gaussian beam focusing

In this section Gaussian beam propagation through nanostructured GRIN microlenses is investigated numerically and the concept of the nanostructured GRIN microlens is successfully tested in the case of the Gaussian beam illumination [41, 11]. The finite difference time domain (FDTD) method [13, 14] (see section 2.4.1 in chapter 2) implemented in the MEEP package [44] has been utilised for this purpose. The focusing properties of the nanostructured GRIN lens have been compared for Gaussian illumination with the focusing properties of the corresponding continuous GRIN lens. The accuracy of the scalar paraxial GRIN theory in the case of GRIN microlenses characterised by a high refractive index gradient is also investigated.

4.1.1 Description of the simulated problem

The theoretical description of Gaussian beam propagation through the GRIN rod lens based on the scalar and paraxial approximations has been presented in details in section 2.2 of chapter 2. Key formulae and features resulting from this approximation for planar Gaussian illumination are repeated here for a reader's convenience.

The GRIN rod lens is assumed to have an optical axis oriented along Z (Fig. 2.2). The refractive index distribution within the lens is given by [3]

$$n(x,y) = n_0[1 - \frac{g_0^2}{2}(x^2+y^2)] \tag{4.1}$$

where n_0 denotes refractive index in the centre of the lens cross-section and g_0 denotes the gradient parameter. Real lenses have a finite diameter d and a minimum refractive index $n_{\min}$. The above mentioned parameters are related to each other by

$$g_0^2 = \frac{8(n_0 - n_{min})}{n_0 d^2}. \tag{4.2}$$

Eq. (4.2) is derived from Eq. (4.1) assuming that $x^2+y^2 = (d/2)^2$ and $n(x,y) = n_{min}$.

If the planar Gaussian illumination with maximum intensity located on the Z axis is used, the complex amplitude at the input face of the GRIN lens is described by

$$\psi(x,y,z=0) = \exp\left(-\frac{x^2+y^2}{w_0^2}\right) \tag{4.3}$$

where w_0 is the waist radius of the Gaussian beam in free space. This waist is located at the input facet of the lens. The complex amplitude within the GRIN lens can be expressed using the radius of wavefront curvature $R(z)$, beam radius $w(z)$ and function $G_p(z)$ (given by Eq. (2.45)) [3]

$$\psi(x,y,z) = \frac{1}{G_p(z)} \exp[-ik_0 n_0 z] \exp\left[-\frac{x^2+y^2}{w^2(z)}\right] \exp\left[\frac{-i\pi(x^2+y^2)}{\lambda_0 R(z)}\right], \tag{4.4}$$

where

$$w^2(z) = w_0^2 |G_p(z)|^2, \tag{4.5}$$

$$\frac{1}{R(z)} = \frac{n_0}{2w^2(z)} \frac{dw^2(z)}{dz}. \tag{4.6}$$

Following formula (4.5) the dependence of the square of the beam radius on the propagation distance z within the GRIN lens can be written as

$$w^2(z) = w_0^2 \left[cos^2(g_0 z) + \frac{w_{\text{fm}}^4}{w_0^4} sin^2(g_0 z) \right] \tag{4.7}$$

where quantity w_{fm} is given by Eq. (2.50). One can easily see that if $w_0 = w_{\text{fm}}$ then $w(z)$ is independent of z. Otherwise $w(z)$ is periodical with period π/g_0. If $w_0 > w_{fm}$ $w(z)$ decreases for $0 < z < \pi/(2g_0)$ and reaches minimum for $z = \pi/(2g_0)$. In the FDTD simulation presented in this chapter properties of quarter-pitch nGRIN microlenses are investigated. As has been mentioned in chapter 2, the quarter-pitch GRIN lens is the lens characterised by length (thickness) $L_{QP} = \pi/(2g_0)$.

Focusing of a Gaussian beam occurs when $w_0 > w_{\text{fm}}$. The focus is located on the output facet of the quarter-pitch GRIN lens. Simulations of Gaussian beam focusing discussed in the next section has been performed according to the schematic presented in Fig. 4.1. The theoretical value of the beam radius (beam half-width) w_{min} at the output facet of the quarter-pitch GRIN lens is given by

$$w_{\text{min}} = \frac{w_{\text{fm}}^2}{w_0}. \tag{4.8}$$

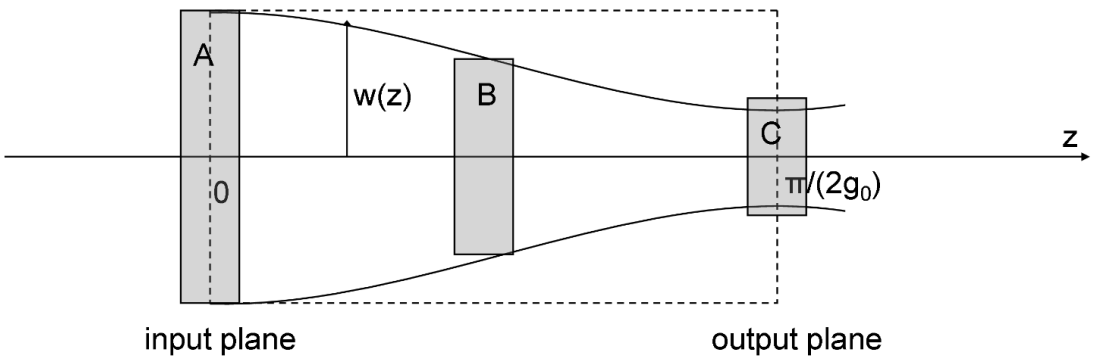

Figure 4.1 – Schematic of the performed FDTD simulations of Gaussian beam focusing. On-axis propagation of the Gaussian beam through GRIN microlens. $Z \times X$ section is shown.

4.1.2 Comparison of focusing properties of continuous and nanostructured GRIN lenses

Let us consider a quarter pitch GRIN microlens illuminated with a planar Gaussian beam [41, 11]. Both the continuous and the corresponding nanostructured GRIN microlenses have been simulated with the FDTD technique [13, 14] using the freely available software package Meep [44]. Schematic of the simulations has been shown in the previous section in Fig. 4.1. In the simulations microlenses are enclosed in glass in order to avoid the back reflection from the lens facets, and thus to facilitate an investigation of the Gaussian beam propagation in GRIN medium. 3D simulations have been done for three different gradients of refractive index. The focusing properties of continuous and nanostructured microlens are compared. Strictly speaking the time averaged Z component of the Poynting vector in the longitudinal section of the lens and the beam profile at the output facet of the lens are compared. The curvature of the wavefronts within both considered microlenses are also investigated. Additionally values of the output beam half-width obtained in the FDTD simulations are compared with predictions of the paraxial scalar GRIN theory [3] given by formula (4.8).

The refractive index distribution within a continuous GRIN microlens is described by Eq. (4.1). Firstly the refractive index distribution characterised by a gradient parameter $g_0 = 45\text{mm}^{-1}$ and on-axis refractive index $n_0 = 1.619$ is investigated. The diameter d of the microlens is 10μm leading to a minimum refractive index n_{min} of 1.578. The above-mentioned parameters are related to each other by Eq. (4.2) and in this case the quarter-pitch value predicted by the paraxial scalar GRIN theory is 34.9μm.

The refractive index distribution in cross-section of the continuous GRIN microlens and the corresponding nanostructured GRIN microlens are presented in Fig. 4.2. The nanostructured microlens consists of 2500 nanorods ordered in a square lattice. They are $0.2\mu\text{m} \times 0.2\mu\text{m}$ in cross-section. One type of nanorod is made of F2 glass and has refractive index 1.619 and the other type of nanorod is made of the concept glass characterised by a refractive index 1.578.

Both the continuous and nanostructured GRIN microlens are illuminated with a planar Gaussian beam polarised linearly along the Y axis and characterised by a beam half-width $w_0 = 5\mu$m. Vacuum wavelength λ_0 is $1\mu m$. The size of the computational cell is $18\mu m \times 18\mu m \times 42\mu m$. Spatial step Δx is equal to $\frac{\lambda_0}{20} = 50nm$. Time step Δt is set to ensure numerical stability [14].

According to the previous section a schematic of both simulations is presented in Fig. 4.1. The intensity distribution within the continuous GRIN microlens is presented in Fig. 4.3 and the corresponding intensity distribution within the nanostructured

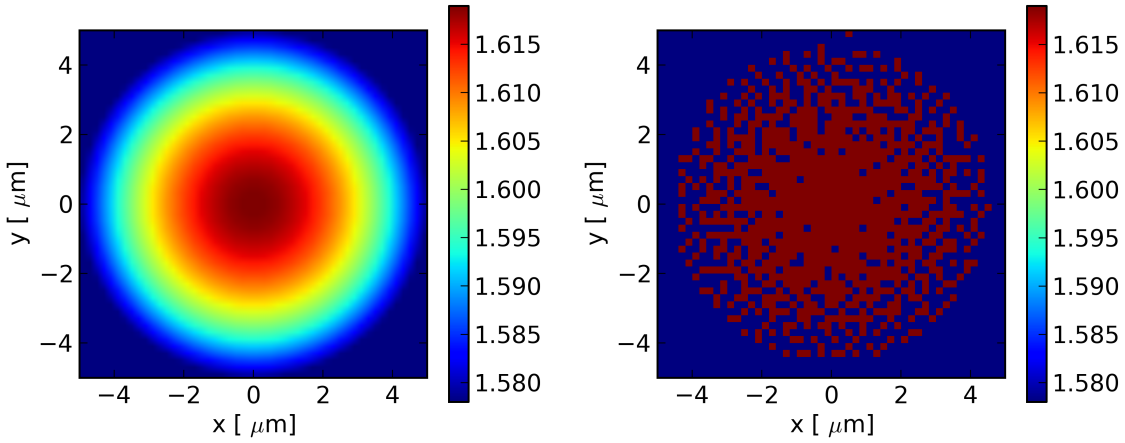

(a) (b)

Figure 4.2 – Cross-section of the refractive index distribution in continuous GRIN microlens (a) and corresponding nanostructured GRIN microlenses (b). On-axis refractive index n_0 is 1.619 and minimum refractive index $n_{\min}$ is 1.578.

GRIN microlens is shown in Fig 4.4. Intensity is represented by the Z component of the time averaged Poynting vector $\bar{S}_z$.

Figs. 4.3 and 4.4 show the intensity distribution in longitudinal sections of the considered microlenses. A cross-section at the quarter-pitch plane is presented in Fig. 4.5a and Fig. 4.5b for continuous and nanostructured GRIN microlenses respectively. The curvature of the wavefronts within the continuous and the corresponding nanostructured GRIN microlens is presented in Figs. 4.6-4.8. The presented intensity and phase distributions show similar performance in the both cases. The visible pixellation of the phase distributions is caused by the discrete nature of the FDTD method, which is a finite difference numerical technique.

The wavefront curvature $1/R$ as a function of propagation distance z has been analysed in case of both microlenses. R denotes the radius of the wavefront curvature. This dependence is presented in Fig. 4.9. It is easy to determine the quarter pitch length based on FDTD simulation and the condition $1/\mathrm{R(z)} = 0$. One can see that in the case of both the continuous and nanostructured GRIN microlenses the quarter pitch value obtained with FDTD technique is about 35μm The value of the quarter pitch predicted by the paraxial scalar GRIN theory is equal to 34.9μm which is roughly consistent with FDTD modelling results. The difference between the paraxial scalar GRIN theory and modelling results is more significant for higher gradient of effective refractive index. This issue is discussed later in this section.

Next the beam profiles at the output plane of the continuous and the nanostruc-

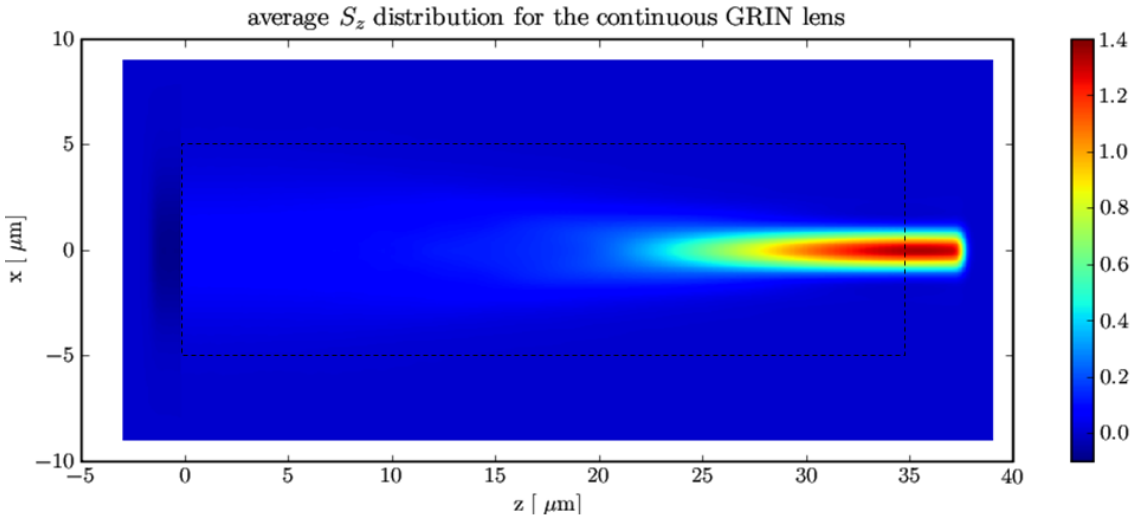

Figure 4.3 – Intensity distribution for the continuous GRIN microlens obtained in the FDTD modelling. On-axis propagation of the Gaussian beam through GRIN microlens with continuous refractive index profile. The Z component of the averaged in time Poynting vector in the $X \times Z$ section is shown. Dash line denotes a contour of the quarter-pitch microlens.

tured GRIN microlens are compared with each other and also with the theoretical model given by scalar paraxial theory (Eq. (4.8)). The comparison has been done for three different gradients of refractive index. The above-mentioned beam profiles are shown in Figs. 4.10-4.12. The FDTD outputs have been approximated to Gaussian profiles and good fits have been obtained. The goodness of these fits is estimated by a normalised root mean square error σ defined as

$$\sigma = \sqrt{\frac{\sum_{i=1}^{N} \left(\frac{o(x_i) - f(x_i)}{Max} \right)^2}{N}}, \tag{4.9}$$

where $o(x_i)$ denotes the FDTD output, $f(x_i)$ denotes the fitted Gaussian profile and Max means a maximum value of the FDTD output.

For three pairs of continuous and nanostructured GRIN microlenses values presented in Tab. 4.1 have been obtained with FDTD technique. $w_{\min}$ denotes the beam half-width at the predicted focal plane.

It is clear that the intensity distributions within both the continuous and nanos-

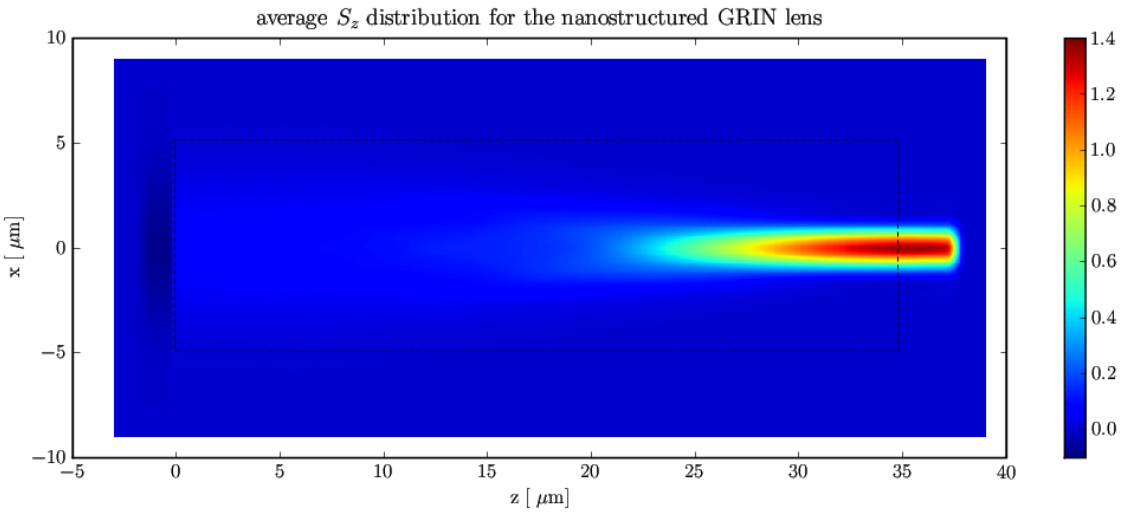

Figure 4.4 – Intensity distribution for the nanostructured GRIN microlens obtained in the FDTD modelling. On-axis propagation of the Gaussian beam through nanostructured GRIN microlens. The Z component of the averaged in time Poynting vector in the $X \times Z$ section is shown. Dash line denotes a contour of the quarter-pitch microlens.

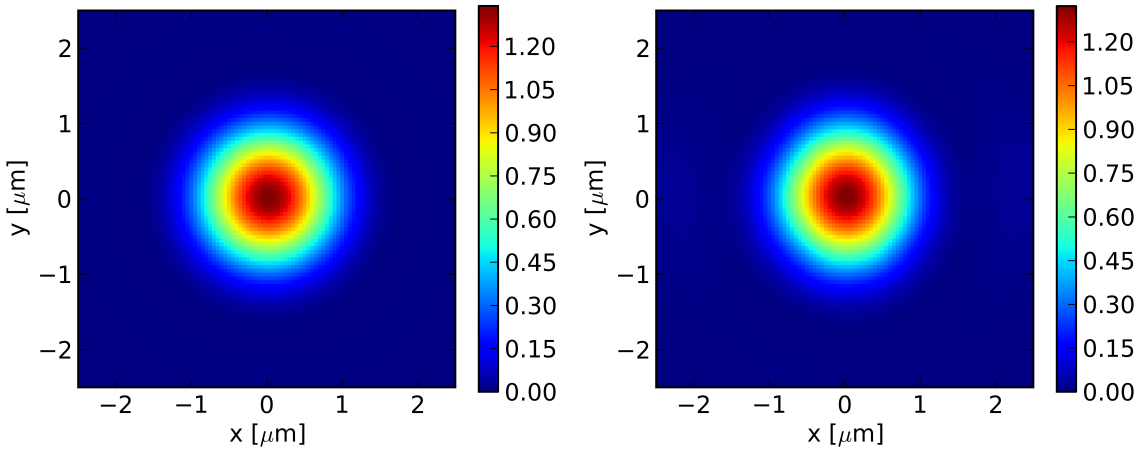

(a) (b)

Figure 4.5 – Intensity distribution of a focused Gaussian beam at the quarter pitch plane for the continuous (a) and nanostructured (b) GRIN microlens – a cross-section in the XY plane of 3D FDTD simulations

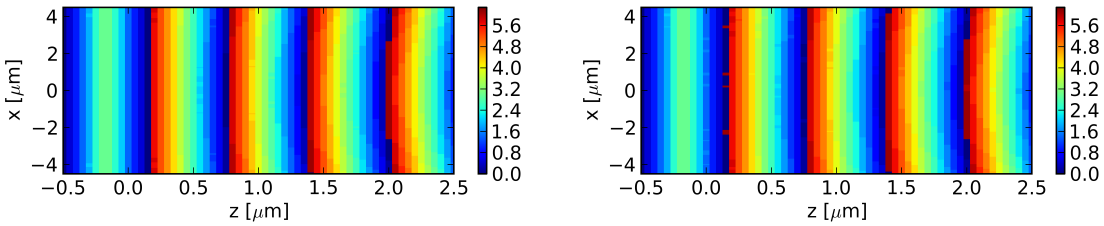

(a) Continuous GRIN microlens. (b) Nanostructured GRIN microlens.

Figure 4.6 – The phase distribution in the area close to input lens facet within the continuous and the nanostructured GRIN lens is presented (area A in Fig. 4.1).

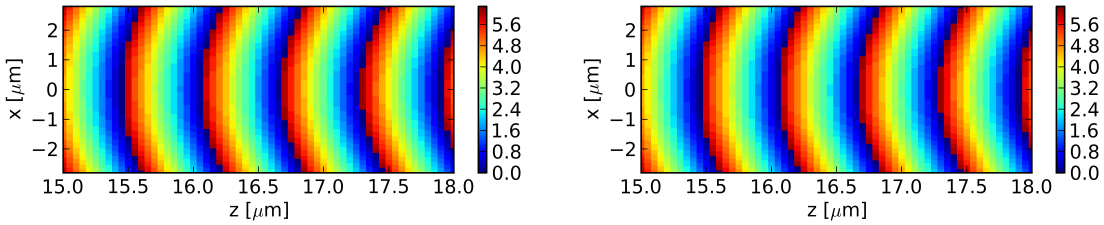

(a) Continuous GRIN microlens. (b) Nanostructured GRIN microlens.

Figure 4.7 – The phase distribution within the continuous and the nanostructured GRIN lens is presented (area B in Fig. 4.1).

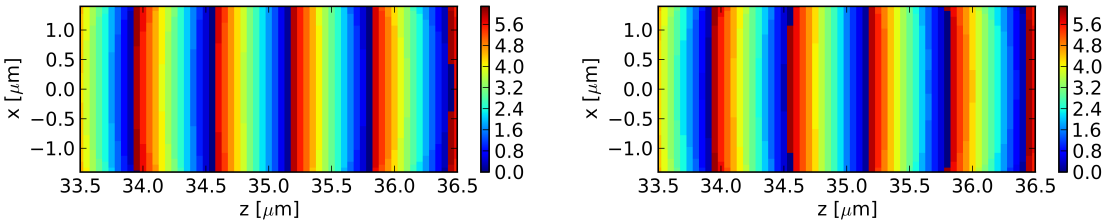

(a) Continuous GRIN microlens. (b) Nanostructured GRIN microlens.

Figure 4.8 – The phase distribution in the area close to output lens facet within the continuous and the nanostructured GRIN lens is presented (area C Fig. 4.1).

tructured GRIN microlenses are very similar for all three gradient parameter values. The small side lobes in Fig. 4.10(b) obtained for the nGRIN microlens with gradient parameter $g_0 = 67\text{mm}^{-1}$ are the only significant difference. The occurrence of side lobes is related to the large gradient parameter.

It has been demonstrated that, in terms of Gaussian beam propagation, the continuous GRIN microlens and corresponding nanostructured GRIN microlens are equivalent. The paraxial GRIN lens theory gives an approximate prediction of the half-width of the output beam, although gradients of the effective refractive index in the inves-

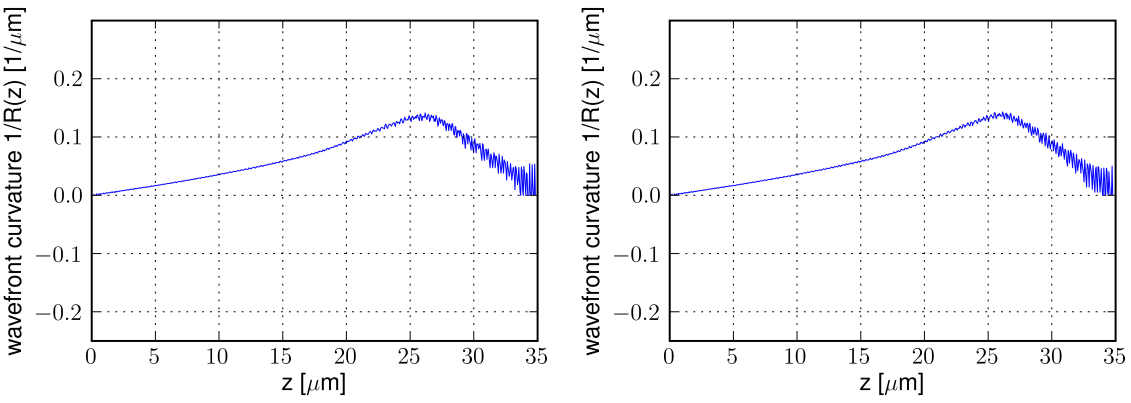

(a) Continuous GRIN microlens.

(b) Nanostructured GRIN microlens.

Figure 4.9 – Wavefront curvature $1/R$ as a function of the propagation distance for the continuous GRIN microlens (a) and the nanostructured GRIN microlens (b). Gradient parameter $g_0 = 45\text{mm}^{-1}$.

gradient parameter g_0	scalar paraxial theory	continuous GRIN microlens	nanostructured GRIN microlens
$g_0 = 67\text{mm}^{-1}$	$w_{\text{min}} = 0.59\mu\text{m}$	$w_{\text{min}} = 0.80\mu\text{m}$ $\sigma = 0.0078$	$w_{\text{min}} = 0.80\mu\text{m}$ $\sigma = 0.0126$
$g_0 = 45\text{mm}^{-1}$	$w_{\text{min}} = 0.87\mu\text{m}$	$w_{\text{min}} = 1.15\mu\text{m}$ $\sigma = 0.0105$	$w_{\text{min}} = 1.15\mu\text{m}$ $\sigma = 0.0103$
$g_0 = 21\text{mm}^{-1}$	$w_{\text{min}} = 1.86\mu\text{m}$	$w_{\text{min}} = 2.35\mu\text{m}$ $\sigma = 0.0054$	$w_{\text{min}} = 2.25\mu\text{m}$ $\sigma = 0.0100$

Table 4.1 – Beam half-widths w_{min} at the predicted focal plane according to the scalar paraxial GRIN theory and FDTD modelling given for three pairs of continuous and nanostructured GRIN microlenses. σ is defined in by formula (4.9).

tigated GRIN microlenses are very high with respect to standard GRIN microlenses ($g_0 \sim \text{mm}^{-1}$) [36]. The dependence of the difference between the scalar paraxial GRIN theory and FDTD simulations of the nGRIN microlens focusing on the index gradient g_0 has been also investigated. The measure D of this relative difference is defined as

$$D = \frac{w_{\text{min}}^{\text{FDTD}} - w_{\text{min}}^{\text{theory}}}{w_{\text{min}}^{\text{FDTD}}}, \tag{4.10}$$

where $w_{\text{min}}^{\text{FDTD}}$ denotes the FDTD obtained half-width of the beam at the predicted focal plane of the nanostructured microlens and $w_{\text{min}}^{\text{theory}}$ denotes the theoretical value of the beam half-width in the predicted focal plane. The theoretical value is given by formula (4.8). The dependence of the relative difference D on the quarter-pitch

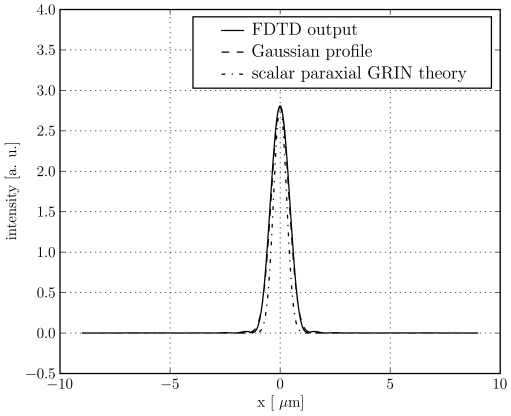

(a) Continuous GRIN microlens.

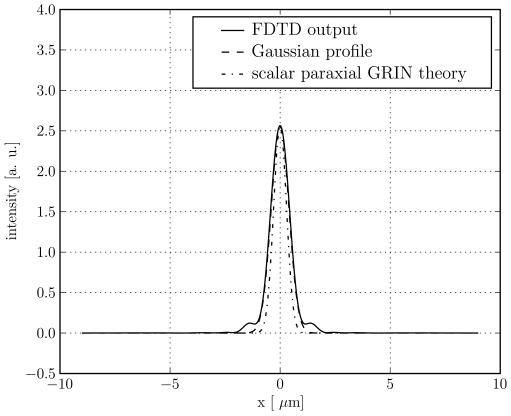

(b) Nanostructured GRIN microlens.

Figure 4.10 – Time averaged Poynting vector intensity (solid – FDTD; dash – Gaussian fit to FDTD; dot-dash – scalar paraxial theory) at the predicted focal plane ($z = 23.4\mu$m) of the continuous (a) ($\sigma = 0.0078$) and the nanostructured (b) ($\sigma = 0.0126$) GRIN lenses for gradient parameter $g_0 = 67\text{mm}^{-1}$.

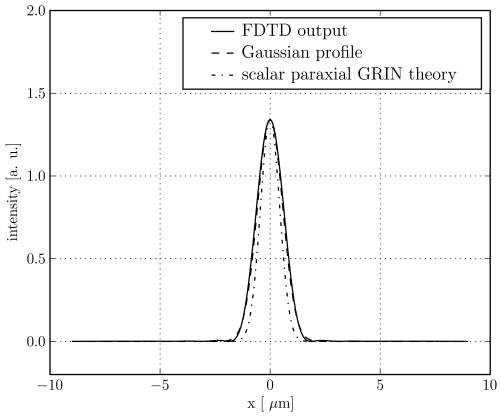

(a) Continuous GRIN microlens.

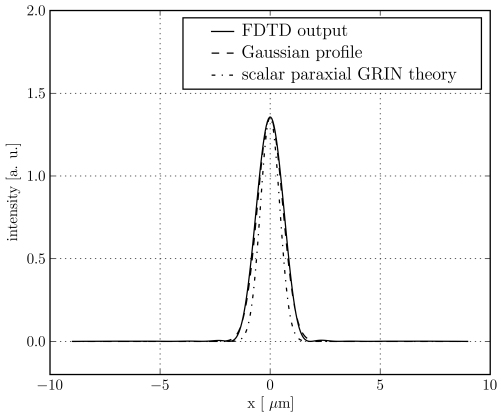

(b) Nanostructured GRIN microlens.

Figure 4.11 – Time averaged Poynting vector intensity (solid – FDTD; dash – Gaussian fit to FDTD; dot-dash – scalar paraxial theory) at the predicted focal plane ($z = 34.9\mu$m) of the continuous (a) ($\sigma = 0.0105$) and the nanostructured (b) ($\sigma = 0.0103$) GRIN lenses for gradient parameter $g_0 = 45\text{mm}^{-1}$.

length $L_{\text{QP}} = \pi/(2g_0)$ is shown in Fig. 4.13. One can see that in the range between $g_0 = 21\text{mm}^{-1}$ (corresponding to $L_{\text{QP}} = 74\mu$m) and $g_0 = 80\text{mm}^{-1}$ (correspoding to $L_{\text{QP}} = 20\mu$m) the relative difference D increases as a function of gradient g_0. This increase can be explained by the fact that the scalar and paraxial approximations are less precise for larger gradients of refractive index. The dependence of relative difference D on quarter-pitch length L_{QP} has regular character, provided L_{QP} is not

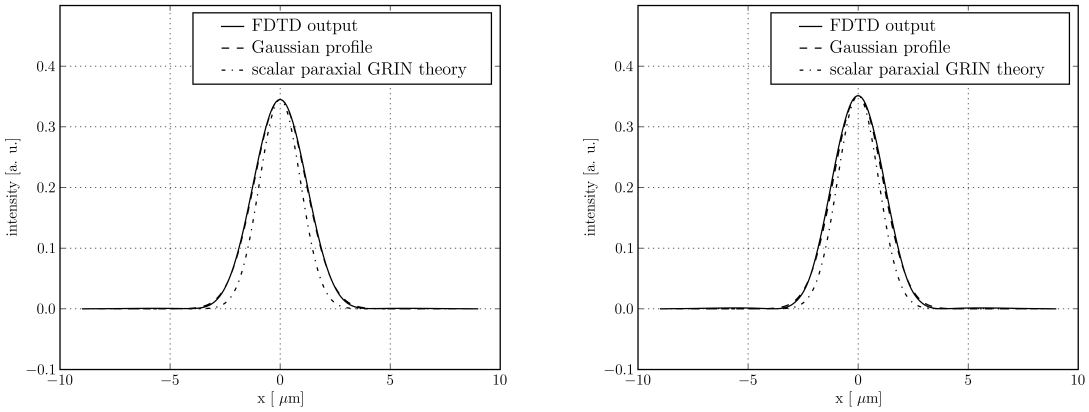

(a) Continuous GRIN microlens. (b) Nanostructured GRIN microlens.

Figure 4.12 – Time averaged Poynting vector intensity (solid – FDTD; dash – Gaussian fit to FDTD; dot-dash – scalar paraxial theory) at the predicted focal plane ($z = 74.5\mu$m) of the continuous (a) ($\sigma = 0.0054$) and the nanostructured (b) ($\sigma = 0.0100$) GRIN lenses for gradient parameter $g_0 = 21\text{mm}^{-1}$.

extremely short i.e. gradient parameter g_0 is not extremely large (see Fig. 4.13). A full-vectorial approach is necessary in the case of extremely high refractive index gradients.

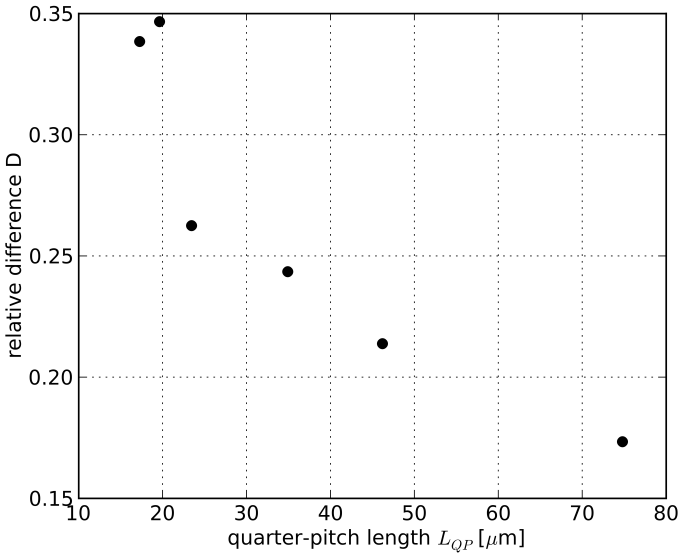

Figure 4.13 – Relative difference D between the scalar paraxial GRIN theory and FDTD simulations as a function of quarter-pitch length L_{QP}.

4.2 Collimation of VCSEL beam using a nGRIN microlens

Collimation of a laser beam is another important phenomenon utilised in photonic devices. Let us consider Vertical Cavity Surface Emitting Lasers (VCSELs), which generally generate high divergence single-mode Gaussian beam profiles. Such lasers can be fabricated in high density 2D arrays [45]. The combination of a GRIN microlens array and an identical pitch VCSEL array would allow the creation of low divergence structured light sources for optical interconnects, printers and scanners [46]. The nanostructured GRIN microlenses might be characterised by very high refractive index gradients (up to $\Delta n = 0.1$ per 5μm) and high numerical aperture. Moreover the microlenses can be arranged into 2D arrays with a filling factor close to 100%. The nGRIN microlens arrays are very thin (about 100 μm thick) with flat input and output facets. These features make it straightforward to integrate such microlens array with a high density 2D VCSEL array in order to collimate the beams generated by the VCSELs. The concept of the system is shown in Fig. 4.14 and in this section FDTD simulation results for a single microlens integrated with a VCSEL laser are presented.

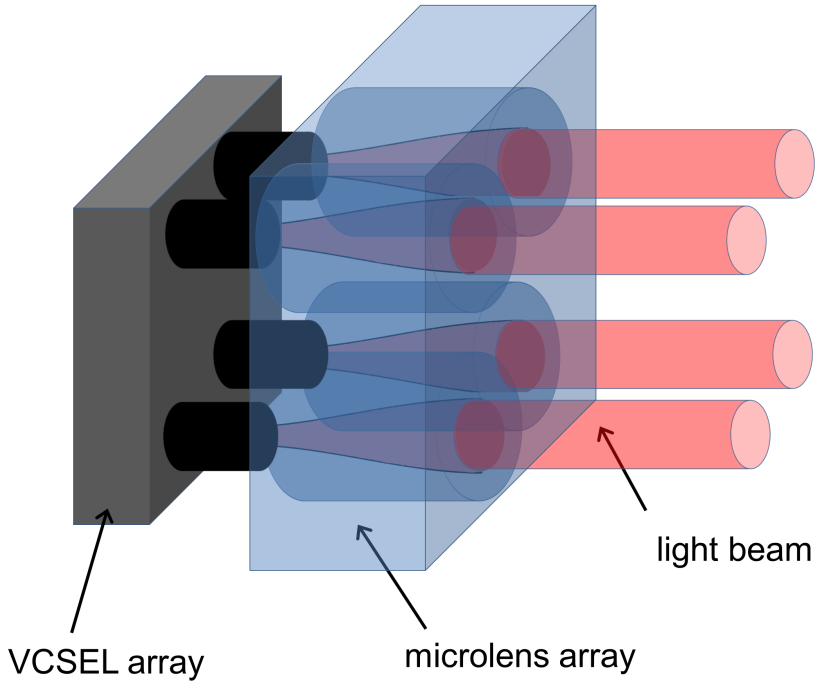

Figure 4.14 – Collimation of the array of VCSEL beams.

4.2.1 FDTD simulation of the VCSEL beam collimation

The goal of the Finite Difference Time Domain (FDTD) simulations [13] (performed using the MEEP package [44]) is to show that a nanostructured GRIN rod microlens can collimate a VCSEL beam with its optical axis oriented along the z-axis. A single mode VCSEL beam can be approximated by a planar Gaussian beam described by the complex amplitude

$$\psi(x, y, z = 0) = A \exp\left(-\frac{x^2 + y^2}{w_0^2}\right) \tag{4.11}$$

where $w_0 = 1.53\mu$m is the half-width of the beam. The VCSEL is assumed to be monochromatic with a vacuum wavelength of 850nm. The above-mentioned parameters of the source correspond to the VCSEL described in [47]. The spatial step of the FDTD simulation is equal to 25 nm and the time step is set to ensure numerical stability [13]. To achieve collimation of such a beam a GRIN lens with a diameter of 10.24μm and an effective focal length of about 30μm might be used. The desired target effective refractive index distribution is given by

$$n(x, y) = n_0[1 - \frac{g_0^2}{2}(x^2 + y^2)] \tag{4.12}$$

where $n_0 = 1.619$ denotes the refractive index in the centre of the microlens cross-section and $g_0 = 22\text{mm}^{-1}$ denotes the gradient parameter (for theoretical description of lenses with such refractive index distribution see section 2.2 of chapter 2). The microlens consists of two types of glass rods laid parallel to each other with refractive indices of 1.6190 and 1.6088. Each individual glass rod has a square cross-section of 0.16μm x 0.16μm and the total microlens diameter is 10.24μm. The refractive index distribution in the cross-section of the modelled microlens is shown in Fig. 4.15. A schematic of the FDTD simulation of the VCSEL beam collimation is presented in Fig. 4.16. The VCSEL source and the input facet of the microlens are located in the plane $z_0 = 0$. The quarter pitch lens, which has a length of $L_q = \frac{\pi}{2g_0}$, is optimal for the VCSEL beam collimation [3]. The output plane Z_q in the following simulations is located at $z_q = z_0 + L_q$ corresponding to the quarter pitch length of the GRIN lens.

A plot of the intensity distribution along the propagation direction is presented in Fig. 4.17. A plot of the wavefront curvature as a function of the propagation distance is shown in Fig. 4.18. One can see that the wavefront is flat (with a curvature of zero) for a propagation distance of $z = 70\mu$m. In practice, the quarter pitch plane Z_q is located at the distance where the wavefront is flat and for the lens considered here the quarter pitch length is $L_q = 70\mu$m. This value is very close to the theoretical value of quarter pitch length given by the expression $\frac{\pi}{2g_0} = 71.8\mu$m

The intensity distribution in the input plane $z = 0$ and the output plane Z_q is shown in Fig. 4.19. The intensity profile obtained in the output plane Z_q is close to

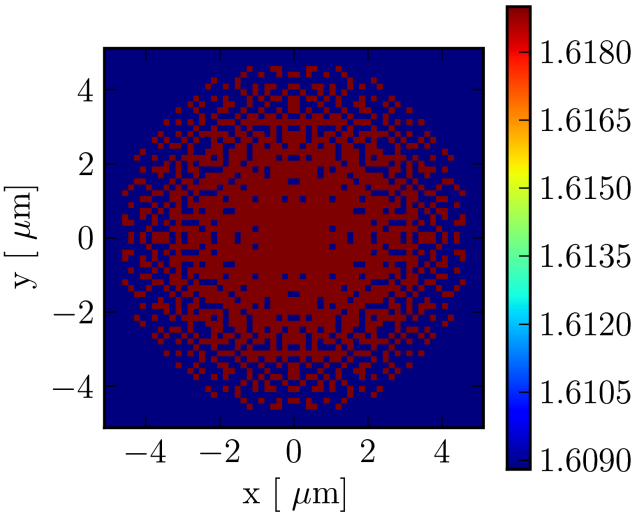

Figure 4.15 – The refractive index distribution in the cross-section of the nanostructured GRIN microlens

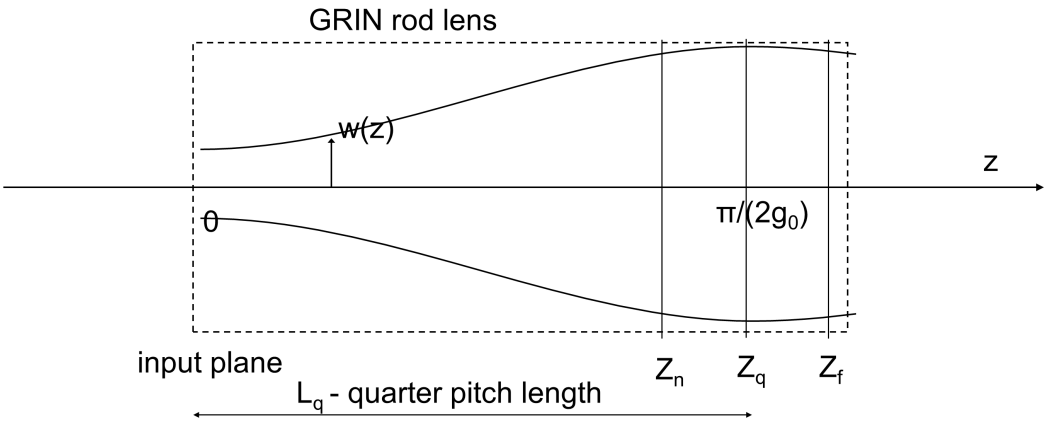

Figure 4.16 – Schematic of the FDTD simulation of the VCSEL beam collimation

a Gaussian profile (Fig. 4.20) and the beam profiles in both the input and output planes have an M^2 of 1.

At the output plane Z_q, the beam half-width is $w_{0q} = 4.7\mu$m and the wavefront is completely flat. In order to calculate the far field divergence half-angle θ one can use

$$\theta = \frac{\lambda_0}{\pi w_0} \tag{4.13}$$

where θ denotes the divergence half-angle and $\lambda_0 = 850$nm is the vacuum wavelength. The results of the FDTD simulations show a reduction in the VCSEL far field diver-

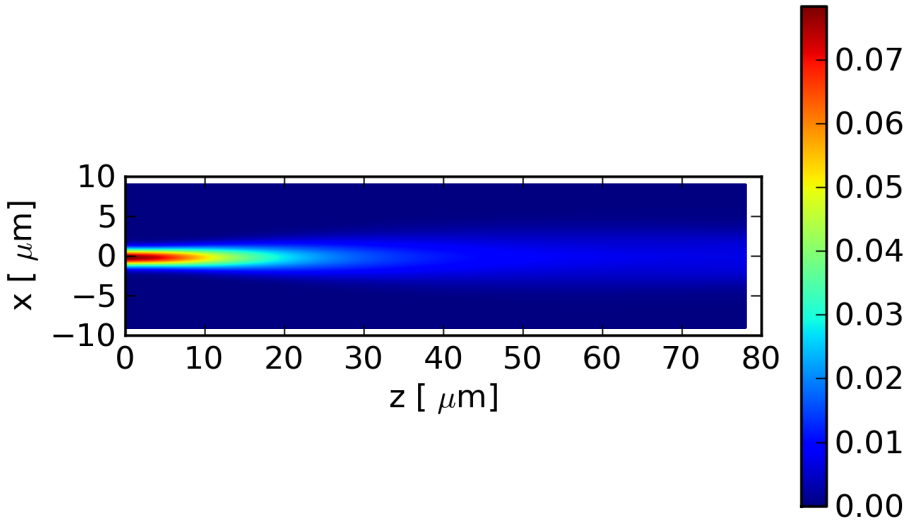

Figure 4.17 – The intensity distribution in the longitudinal section of the FDTD simulation area. The z component of the time averaged Poynting vector in the $Z \times X$ section is shown.

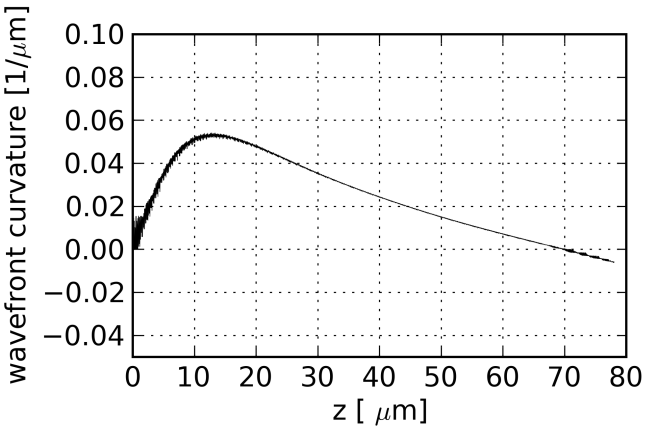

Figure 4.18 – Wavefront curvature as a function of the propagation distance.

gence half-angle from 10.1° to 3.3° due to the presence of the nanostructured GRIN microlens.

4.2.1.1 Polarisation properties

It has been observed that the behaviour of the nanostructured material has a strong dependence on the polarisation of the incident light. This implies that the nanostructured lens performance should be affected by the input polarisation. The FDTD simulation of the nGRIN microlens maintains the linear polarisation of the incident illumination. In the simulation, the VCSEL source has a linear polarisation (E_y)

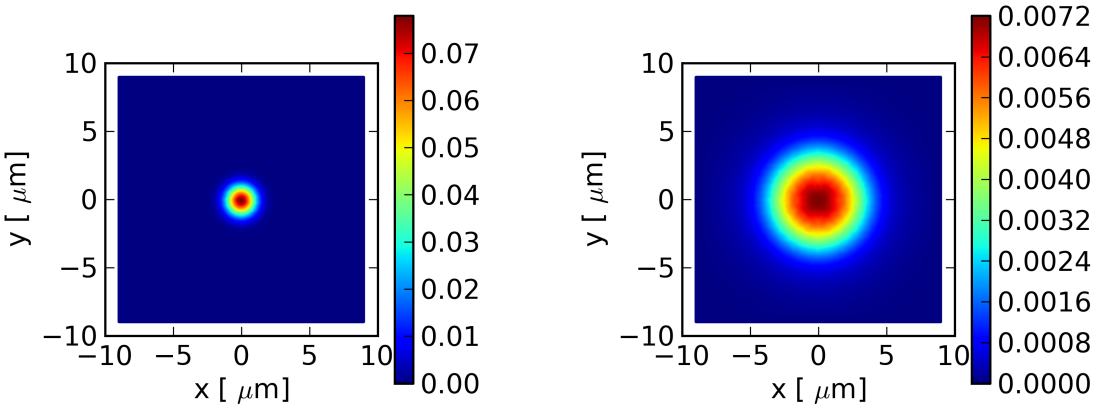

(a) (b)

Figure 4.19 – The intensity distribution in the input plane $z = 0$ (a) and output plane Z_q (b) . The z component of the time averaged Poynting vector is shown.

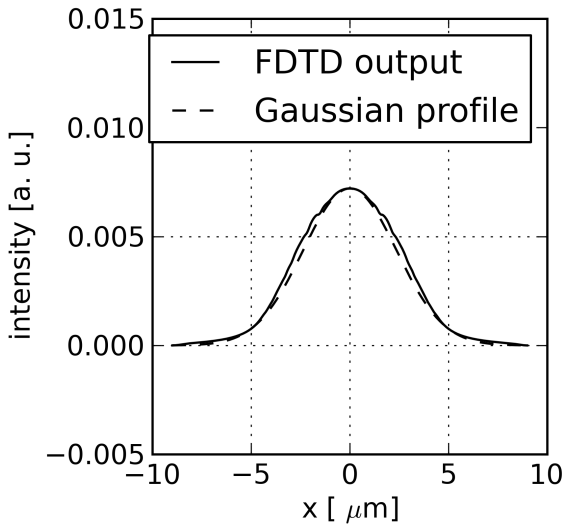

Figure 4.20 – The intensity profile in the output plane Z_q. (solid - FDTD output; dash - Gaussian fit to FDTD output)

and the beam in the output plane Z_q has the same linear polarisation (E_y). The amplitudes of the electric field components E_x and E_y are presented in Fig. 4.21

4.2.1.2 Tolerance of the microlens length

The smallest divergence of the output beam is obtained when a quarter pitch microlens is utilised, which for the considered lens design corresponds to a nGRIN lens length of $L_q = 70\mu$m. In practice, the microlens polishing process has a limited accuracy. The change in the beam divergence for a lens length error of $\pm 10\%$ shorter can be determined by calculating the wavefront curvature and the beam half-width in the

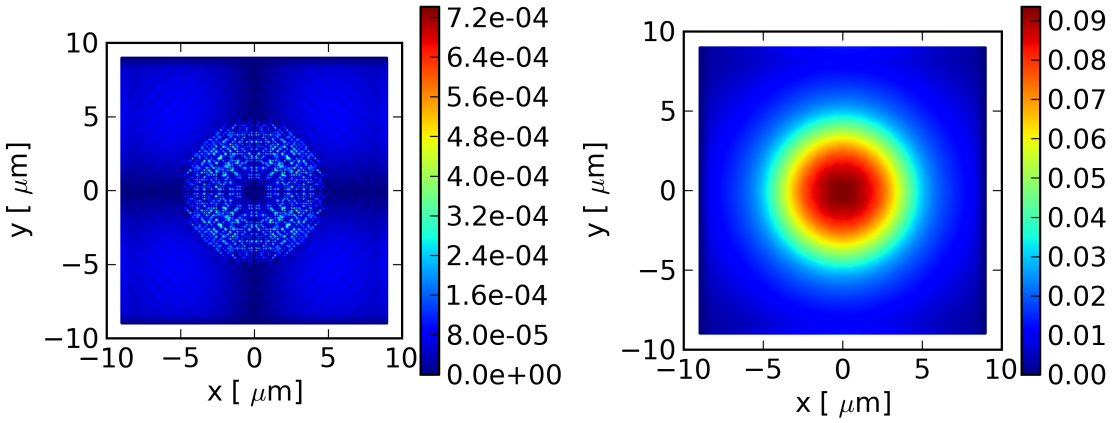

(a) (b)

Figure 4.21 – Amplitudes of the electric field components in the output plane Z_q. Component E_x (a) and component E_y (b)

proximity planes Z_n and Z_f (Fig. 4.16) . The first proximity plane Z_n corresponds to a microlens length of $L_n = 63\mu$m and the second proximity plane Z_f corresponds to a microlens length of $L_f = 77\mu$m.

The beam in the proximity plane Z_n, corresponding to a shorter nGRIN lens, can be approximated by a Gaussian beam with a wavefront curvature of $1/R_n = 0.0050\mu\text{m}^{-1}$ and beam half-width of $w_n = 4.7\mu$m. Propagating this Gaussian beam in air allows the calculation of the beam waist w_{0n} and, hence, the far-field divergence half angle θ_n.

$$\theta_n = \frac{\lambda_0}{\pi w_{0n}} \tag{4.14}$$

Assuming propagation in air, the inverse of the complex radius of curvature q_n is given by [4]

$$\frac{1}{q_n} = \frac{1}{R_n} - i\frac{\lambda_0}{\pi w_n^2} \tag{4.15}$$

and the variation of the complex radius $q(z)$ is given by the simple formula

$$q(z) = q_n + z - z_n \tag{4.16}$$

and therefore the imaginary part of $q(z)$ is constant. Moreover the complex radius q_{0n} for the beam waist is purely imaginary and can be written as

$$q_{0n} = i\,\mathfrak{Im}(q_n) \tag{4.17}$$

where $\mathfrak{Im}(q_n)$ denotes the imaginary part of q_n. On the other hand

$$\frac{1}{q_{0n}} = -i\frac{\lambda_0}{\pi w_{0n}^2} \tag{4.18}$$

where w_{0n} is the waist half-width of the Gaussian beam. Using equations (4.17) and (4.18) we obtain

$$\frac{-i}{\mathfrak{Im}(q_n)} = -i\frac{\lambda_0}{\pi w_{0n}^2} \tag{4.19}$$

and hence

$$w_{0n}^2 = \frac{\lambda_0\,\mathfrak{Im}(q_n)}{\pi}. \tag{4.20}$$

For the shorter lens length, this gives a waist half-width of $w_{0n} = 4.36\mu$m and from equation (4.14) a far field divergence half-angle of $\theta_n = 3.6°$. The same derivation can be applied to the longer microlens, giving a beam waist half-width of $w_{0f} = 4.29\mu$m and a far field divergence half-angle of $\theta_f = 3.6°$.

4.3 Conclusions

It has been demonstrated that, in terms of Gaussian beam propagation, the continuous GRIN microlens and corresponding nanostructured GRIN microlens are equivalent. It has also been shown that standard paraxial GRIN theory gives a fairly good approximation of the Gaussian beam propagation in the high contrast nanostructured GRIN rod microlenses. One can calculate effective parameters of nanostructured GRIN microlenses using standard formulae from the scalar paraxial GRIN theory in order to fabricate nanostructured GRIN microlenses and use them in real systems with laser beam [11, 41].

Additionaly, in conclusion of the section 4.2, one may say that the FDTD simulation shows that the far field divergence half-angle is reduced by the nGRIN microlens with the ideal quarter-pitch thickness from 10.1° to 3.3° and that ±10% inaccuracy of the microlens thickness leads to roughly 10% increase in a final far field divergence.

Chapter 5

Large-diameter quantised nanostructured GRIN microlenses

In this chapter the new approach to develop large-diameter quantised nanostructured GRIN microlenses with internal structure is presented. The performance of a quantised nanostructured microlens is compared with performance of an ideal continuous GRIN microlens. The fabrication method is reported and the focusing properties are measured for various wavelengths. The results described in this chapter have been published in paper [37].

5.1 Motivation for development of large-diameter quantised nGRIN microlenses

In the previous two chapters the concept, the fabrication and the optical properties of the small-diameter nanostructured GRIN microlenses have been described. These microlenses are fabricated using a modified stack-and-draw technique, similar to that commonly used for photonic crystal fiber manufacture. This method allows the creation of extremely large refractive index gradients (up to $\Delta n \sim 0.1$ per 5μm). The functionality of the nanostructured GRIN lens can be described using standard gradient index models [11]. It is has been also demonstrated that a more general (i.e. non-radial) shaping of the refractive index distribution is possible. The successful fabrication of an elliptical nGRIN microlens has been reported in [12]. However the concept of small-diameter nGRIN microlenses described in chapter 3 is limited in terms of the microlens diameter. The diameter is limited roughly up to 20–30μm which radically limits the area of application. The small-diameter nGRIN microlenses are fabricated using a conventional preform assembly technique, where individual rods ($\sim$ 10000 for a 20μm lens) of the basis glasses are placed in the appropriate pattern. Use of this technique to assemble a 100μm diameter lens is currently not feasible, as it would require the manual placement of about 250, 000 individual glass rods. However,

the advent of robotic preform assembly methods may make this direct nanostructuring approach practical in the future.

5.2 Fabrication of large-diameter quantised nGRIN microlenses

In this section the fabrication procedure of the large-diameter quantised nGRIN microlenses is described and thereby the concept of such large-diameter nanostructured microlenses itself is introduced. The concept consists in approximation of the continuous change of the refractive index by the discreet stepped distribution of the refractive index. The performance of such quantised microlens is similar to the performance of the corresponding standard continuous GRIN lens provided a sufficient number of the refractive index levels (steps) is utilised. A discussion of how to determine the suitable number of refractive index levels is included in the next section.

How does one obtain different and well-defined levels of refractive index? One can use the same approach as it is used for fabrication of small-diameter nanostructured microlenses. A desired effective refractive index is attained by a nanostructure consisting of two types of nanorods where each type of nanorods fills determined percentage of the volume. The idea of the large-diameter quantised microlenses is based on nanostructured metarods. Cross-sections of metarods utilised in the prototypical large-diameter microlens are shown in Fig. 5.1. Each type of metarod is utilised to create one level of the effective refractive index in the quantised gradient index profile of the considered microlenses.

Fabrication of metarods is done with the modified stack-and-draw technique in analogous manner to a first stage of the small-diameter nGRIN microlens fabrication. The preform, consisting of two types of glass rods, is stacked. These two types of rods are made of two different glasses characterised by two different refractive indices but similar thermal and mechanical properties. Next the preform is drawn in order to obtain metarods with a diameter of 0.5–0.6mm.

The fabrication of large-diameter quantised nGRIN microlenses is similar to the fabrication of small-diameter nGRIN microlenses described in chapter 3 in terms of the preform assembly technique, control of the drawing process and the requirement of a thermal and mechanical match of the utilised glasses. Assuming that the metarods have been already made the following steps are needed to fabricate large-diameter quantised nGRIN microlenses. The scheme described below allows the production of an array of such large-diameter quantised microlenses with a fill-factor of up to 100%.

1. Metarods are stacked into an initial preform of the large-diameter quantised mi-

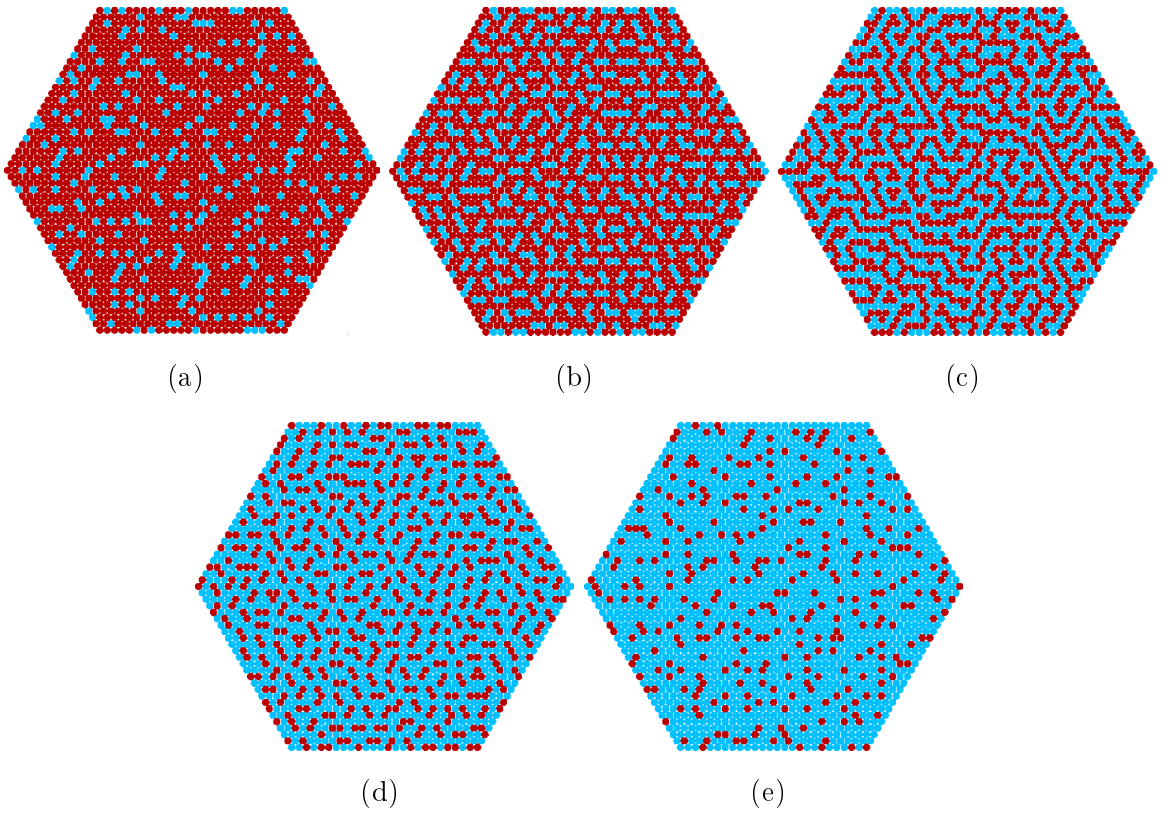

Figure 5.1 – Cross-sections of different nanostructured metarods characterised by different effective refractive indices. Red color and blue color denote high and low refractive index glass respectively.

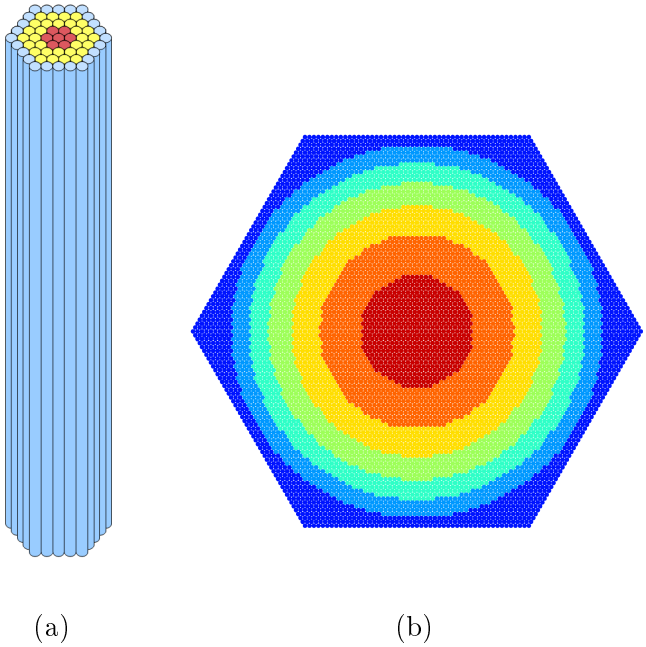

Figure 5.2 – The initial preform of the large-diameter quantised nGRIN microlens. A schematic (a) and the cross-section (b). Different colours denote different metarods.

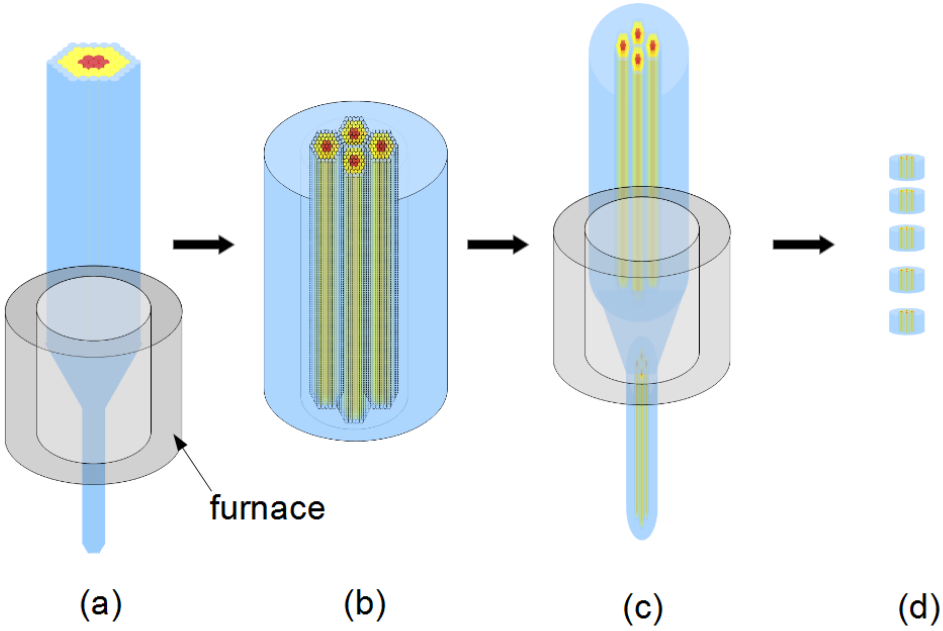

Figure 5.3 – Schematic of the fabrication procedure. The schematic, particularly sub-figures (b), (c), (d), shows the case of the microlens array production.

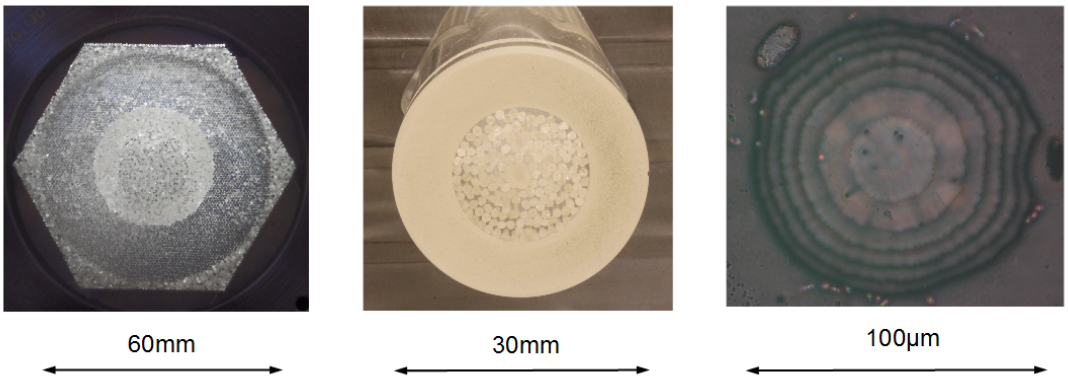

Figure 5.4 – The photos of the initial preform (a), the intermediate preform (b) and the final microlens (c). A single 7–level large-diameter quantised nGRIN microlens has been developed as a proof-of-concept prototype.

crolens. The structure of the initial preform corresponds to the single quantised microlens (Fig. 5.2).

2. The stacked initial preform is drawn-down in the high temperature (600–700°C) using the draw tower (Fig. 5.3a and Fig. 3.6).

3. Rods obtained in the previous step are stacked into an intermediate preform. The outer glass tube and additional filling rods are utilised to construct this intermediate preform. This step allows the fabrication of microlens arrays

Glass Name	Weight Composition	n for $\lambda_0 = 850$nm	n for $\lambda_0 = 633$nm
F2	SiO_2 – 45.7%, PbO – 45.5%, Na_2O – 3.5%, K_2O – 5.0%, As_2O_3 – 0.8%	1.6068	1.6165
NC21A	SiO_2 – 55.0%, Al_2O_3 – 1.0%, B_2O_3 – 26.0%, Li_2O – 3.0 %, Na_2O – 9.5%, K_2O – 5.5%, As_2O_3 – 0.8%	1.5212	1.5265

Table 5.1 – Weight composition of the utilised glasses (F2 and NC21A) and their refractive indices.

(Fig. 5.3b).

4. The intermediate preform is drawn-down in the high temperature (600–700°C) using the draw tower and one obtains the final output rod (Fig. 5.3c).

5. Final rod is cut into slices (Fig. 5.3d) and then polished. Every slice is a large-diameter quantised nGRIN microlens array.

These slices, which are microlens arrays, are very thin, hence it is feasible to produce thousands of microlens arrays based on the same initial preform. The development approach based on the nanostructured metarods retains advantages of the fabrication method presented in subsection 3.2.1 of chapter 3 in terms of a potentially arbitrary non-radial effective refractive index profile and high refractive index gradients.

A single 7–level large-diameter quantised nGRIN microlens has been developed as a proof-of-concept prototype, although the scheme described above allows the fabrication of microlens arrays. The fabricated microlens is 100μm in diameter and 140μm thick (long). The photos of the initial preform, the intermediate preform and the final microlens are presented in Fig. 5.4. F2 glass made by Schott AG and NC21A glass made by Institute of Electronic Materials Technology (ITME) have been utilised as the fundamental glasses to fabricate metarods and thereby the prototype quantised nGRIN microlens itself. The weight composition and refractive indices of these glasses are presented in Tab. 5.1.

5.3 Number of refractive index levels and the diameter of the quantised nGRIN microlens

For a given wavelength, the optical performance of a large-diameter quantised nanostructured GRIN microlens depends on the number of the refractive index levels and the diameter of the microlens. Taking into account the current constraints of the fabrication technique, seven levels of refractive index is a practical technological limit for such a quantised microlens. Let us consider illumination with the vacuum wavelength of 850nm and the number of the refractive index levels equal to 7. It is expected that the smaller the diameter of the microlens the better performance of the considered quantised microlens. The question arises what diameter is sufficiently small to ensure good optical performance of the quantised nGRIN microlens. A series of simulations have been performed to answer this question. The performance of the ideal continuous GRIN microlens is numerically compared with the performance of the quantised microlens for three different microlens diameters. The simulations have been done with fast Fourier transform beam propagation method (FFT-BPM) [37]. The refractive index distributions in the cross-section of the ideal continuous GRIN microlens and the corresponding quantised microlens are shown in Fig. 5.5. Results

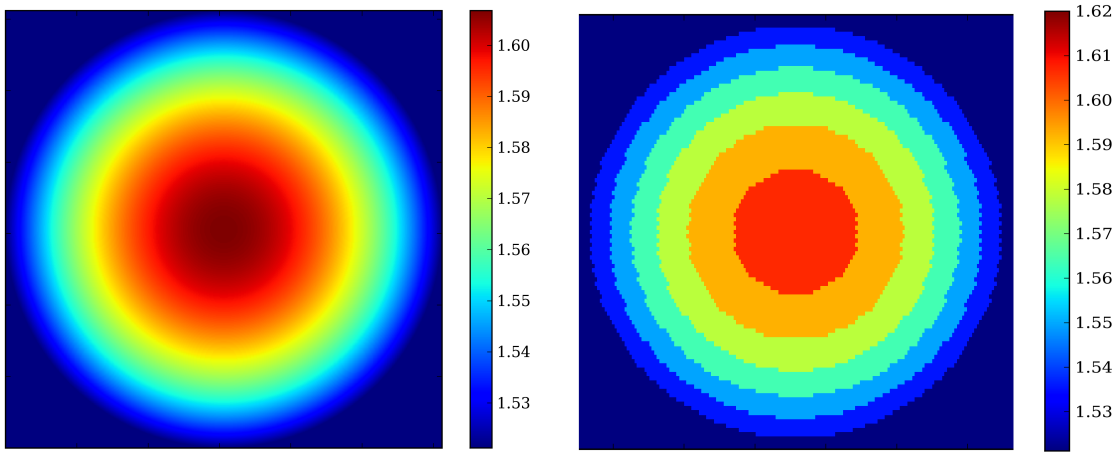

(a) (b)

Figure 5.5 – Refractive index distribution in the cross-section of ideal continuous GRIN microlens (a). Schematic of quantised nanostructured GRIN microlens consisting of 101×101 "pixels" with one of 7 discrete effective refractive index level structures formed by a nanostructured composite of two soft glasses (b).

of these FFT-BPM simulations are presented in Fig. 5.6. Significant improvement of the focusing performance due to diameter reduction has been observed in case of quantised microlens. One can conclude that the microlens diameter of the order of 100μm ensures good optical performance of 7–level nanostructured GRIN microlens

for vacuum wavelength of 850nm.

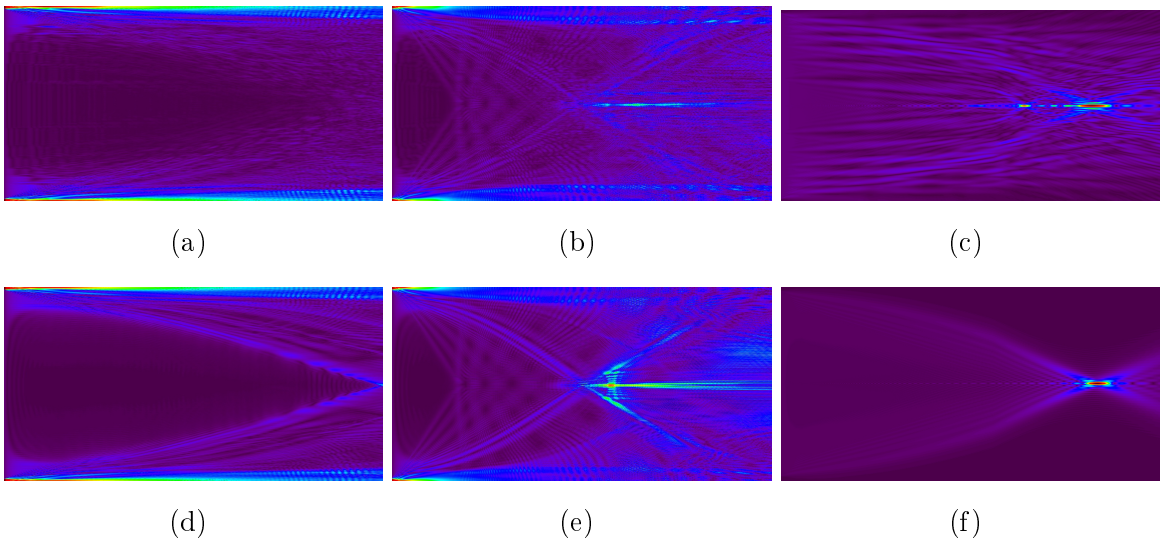

Figure 5.6 – Improvement of focusing for 7–level nanostructured GRIN microlens with reduced diameter of 500μm (a), 250μm (b), 100μm (c). As a reference focusing of ideal continuous GRIN lens with the diameter of 500μm (d), 250μm (e), 100μm (f) is presented. The wavelength of light is 850 nm.

5.4 Numerical verification of performance of developed lens

In order to numerically investigate the expected focusing properties of the fabricated prototype of the quantised nanostructured GRIN microlens described at the end of the section 5.2, the fast Fourier transform beam propagation method (FFT-BPM) has been utilised. The particular implementation of the FFT-BPM had been developed in C++ by Andrew J. Waddie.

The ideal continuous GRIN microlens and the corresponding quantised nanostructured GRIN microlens are shown in Fig. 5.5. Both considered here microlenses are 100μm in diameter. First it is assumed that the vacuum wavelength is 850nm and microlenses are infinite in thickness (length). The simulations of infinite microlenses allow the determination of the quarter-pitch length of the fabricated large-diameter quantised microlens and the corresponding ideal continuous GRIN microlens. Simulation for a continuous (unquantised) microlens was performed as a reference. In this case the lens has a quarter pitch equal to 232μm (Fig. 5.7a) and a full width half maximum (FWHM) beam diameter at focus of 0.8μm (Fig. 5.7b). The quarter-pitch of the quantised microlens has been determined to be 225μm (Fig. 5.8a) with a FWHM beam diameter at the focus of 0.7μm (Fig. 5.8b). The relatively small difference between the two lenses shows that we can expect the quantised nGRIN lens to perform in a similar manner to the ideal lens. It should be noted that the Airy

rings are less intense in the case of the quantised lens (Fig. 5.8b) with respect to the ideal one (Fig. 5.7b). This denotes a degradation of the expected performance of the nanostructured lenses with respect to ideal lenses. In practice, the properties of the fabricated quantised lens should be better than that observed in the simulations due to the presence of sharp refractive index differences on the borders between various quantised levels in the simulations. In the fabricated structures diffusion processes between the glasses result in "fuzzy" border transitions [37].

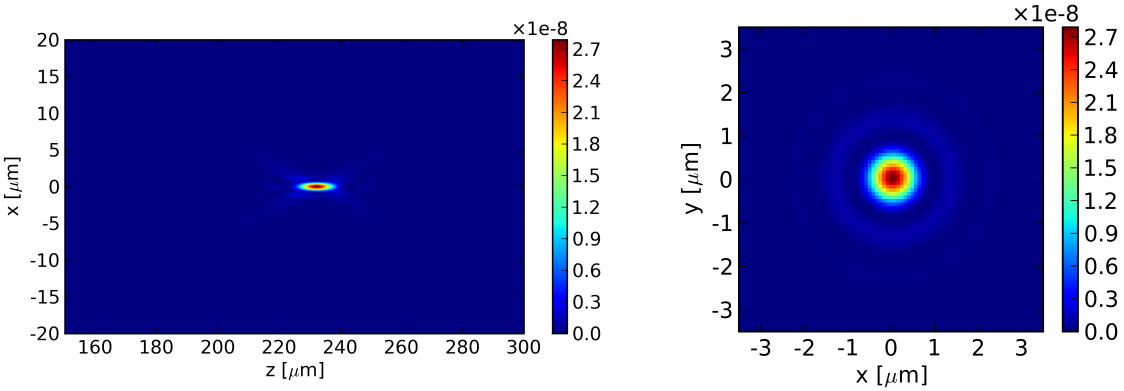

(a) (b)

Figure 5.7 – Propagation of light within the infinite ideal continuous GRIN lens with the diameter of 100μm: the longitudinal section along optical axis (a), the cross-section at the focus perpendicular to the optical axis (b). Simulations are performed for the wavelength of 850nm.

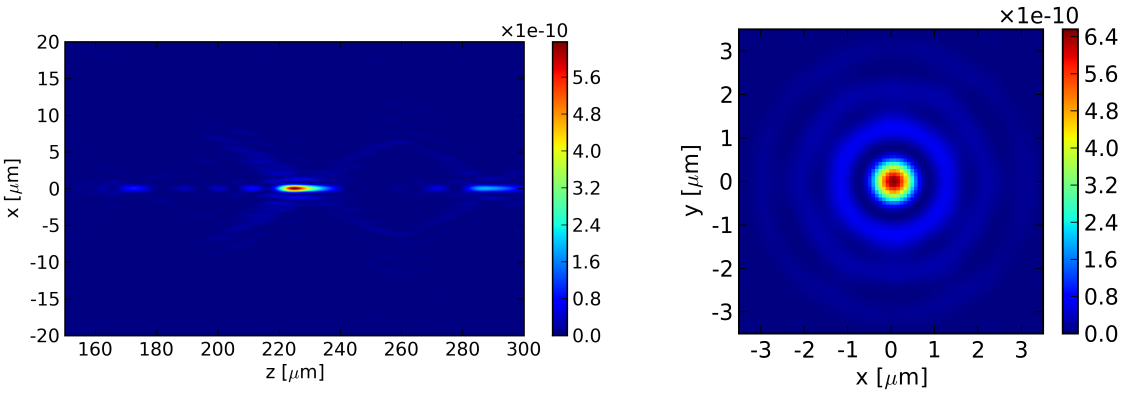

(a) (b)

Figure 5.8 – Propagation of light within the infinite quantised nGRIN lens with the diameter of 100μm: the longitudinal section along optical axis (a), the cross-section at the focus perpendicular to the optical axis (b). Simulations are performed for the wavelength of 850nm.

The measurements presented in the next section have been performed using a quantised nanostructured GRIN microlens with a thickness (length) of 140μm and

simulations to identify the working distance for this length of lens are necessary. In addition, the simulations allow a prediction of the diameter of beam at focus to be made. The working distance of the nanostructured quantised microlens has been numerically determined to be 65μm (Fig. 5.10a) with a FWHM beam diameter at the focus of 0.9μm (Fig. 5.10b). As a reference, the ideal continuous (unquantised) lens with similar parameters of diameter and wavelength has a working distance equal to 68μm (Fig. 5.9a) and a FWHM beam diameter at focus of 1.0μm (Fig. 5.9b). The above-mentioned modelling results have been obtained for the wavelength of 850nm.

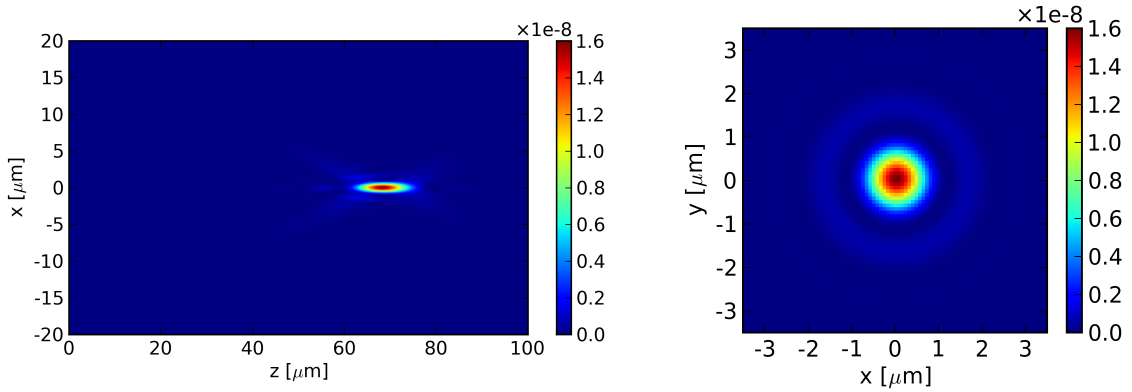

(a) (b)

Figure 5.9 – Propagation of light behind the 140μm thick ideal continuous GRIN lens with the diameter of 100μm: the longitudinal section along optical axis (a), the cross-section at the focus perpendicular to the optical axis (b). Simulations are performed for the wavelength of 850nm.

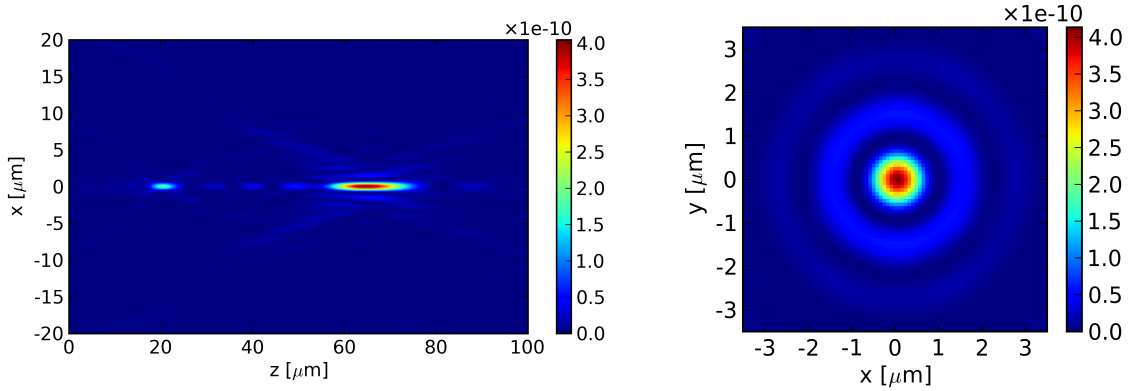

(a) (b)

Figure 5.10 – Propagation of light behind the 140μm thick quantised nGRIN lens with diameter of 100μm: the longitudinal section along optical axis (a), cross-section at focus perpendicular to the optical axis (b). Simulations are performed for the wavelength of 850nm.

The FFT BPM method has permitted the calculation of the chromatic properties

of the 140μm long (thick) nanostructured microlens with the diameter of 100μm to be made. The simulations for the wavelength of 633nm have been performed. In the case of the quantised nanostructured microlens the working distance is 60μm (Fig. 5.12a) with a FWHM beam diameter at the focus of 0.6μm (Fig. 5.12b). As a reference the corresponding ideal continuous (unquantised) microlens has the working distance equal to 63μm (Fig. 5.11a) and the FWHM beam diameter at focus of 0.7μm (Fig. 5.11b).

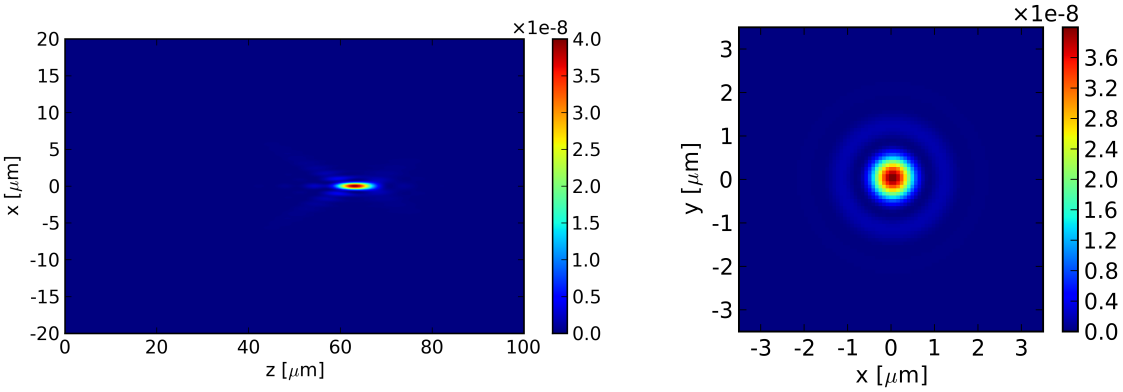

(a) (b)

Figure 5.11 – Propagation of light behind the 140μm thick ideal continuous GRIN lens with the diameter of 100μm: the longitudinal section along optical axis (a), the cross-section at the focus perpendicular to the optical axis (b). Simulations are performed for the wavelength of 633nm.

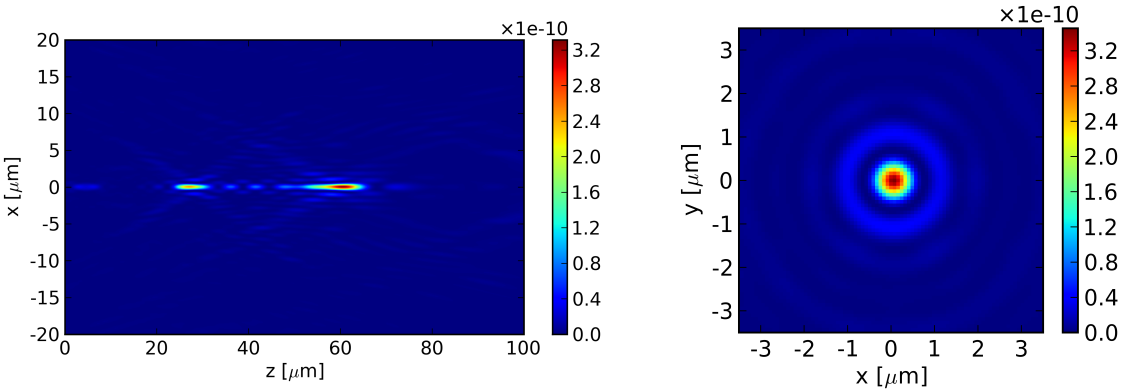

(a) (b)

Figure 5.12 – Propagation of light behind the 140μm thick quantised nGRIN lens with diameter of 100μm: the longitudinal section along optical axis (a), cross-section at focus perpendicular to the optical axis (b). Simulations are performed for the wavelength of 633nm.

In summary, the simulations show that the fabricated 7–level large-diameter quantised nGRIN microlens, with the diameter of 100μm and the length of 140μm, should

have optical performance similar to that of an unquantised ideal GRIN microlens. According to the modelling results the working distance lies within 5% of that of the ideal lens and there is a variation of around 9% over a wavelength range of 200nm (633nm–850nm)[37].

5.5 Experimental verification of focusing properties of developed lens

In order to characterise the focusing properties of the fabricated quantised nGRIN microlens described in section 5.2, the set-up presented in Fig. 5.13 has been used. The set-up consists of an infrared diode laser, a multimode fibre (core diameter 50μm) fitted with a collimation package optimised for wavelength 850nm, ND filters, mirrors and CCD camera COHU (4910 Series) fitted with a tube and microscope objective. The camera has parameter gamma set to 1 and it works with fixed gain. The camera is mounted on a computer controlled 2-axis translation stage. A x40 0.65 NA objective is used. The diode laser wavelength is about 850nm and the beam diameter behind the collimation package is $\sim$ 10mm. Apart from the 850nm infrared diode laser combined with the fibre and the collimation package two different lasers have been utilised to perform measurements i.e. a He–Ne laser with the wavelength of 633nm and a diode laser with the wavelength 532nm. All measurements have been taken with the same CCD camera settings and using the same microscope objective.

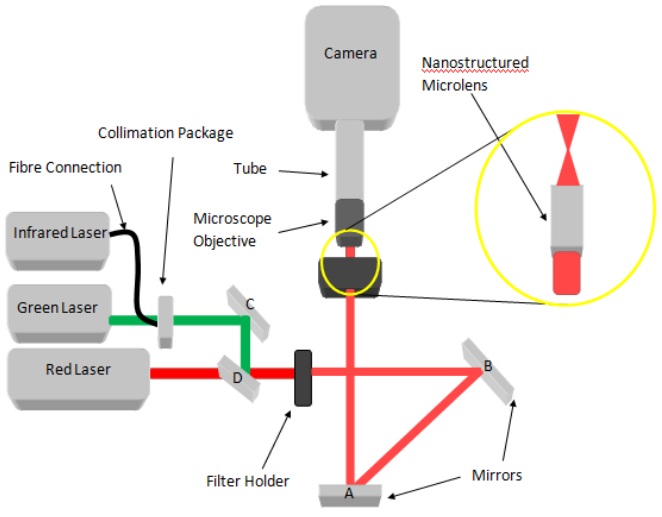

Figure 5.13 – Microlens Characterisation set-up.

We have determined the beam diameter at the focus based on the 2D images obtained with the CCD camera. We used the criterion of the full width in half maximum (FWHM) to determine the diameter of a beam. The focal plane of the lens was determined by scanning with CCD along the optical axis. The computer controlled

translation stage has a submicron precision and the error for the measurement of the distance between subsequent steps is below 1μm. The error in the position of the output facet of the microlens, which is used in the determination of the working distance, is larger and is estimated to be $\pm 10\mu$m.

5.5.1 Focusing properties measured using diode laser 850nm

For the wavelength of 850nm the maximum intensity has been measured 34μm away from the output facet of the microlens. This distance is the back focal length (working distance) of the microlens related to the brightest focus. The intensity distribution in the focal plane is shown in Fig. 5.14. One can see that the focal spot has an

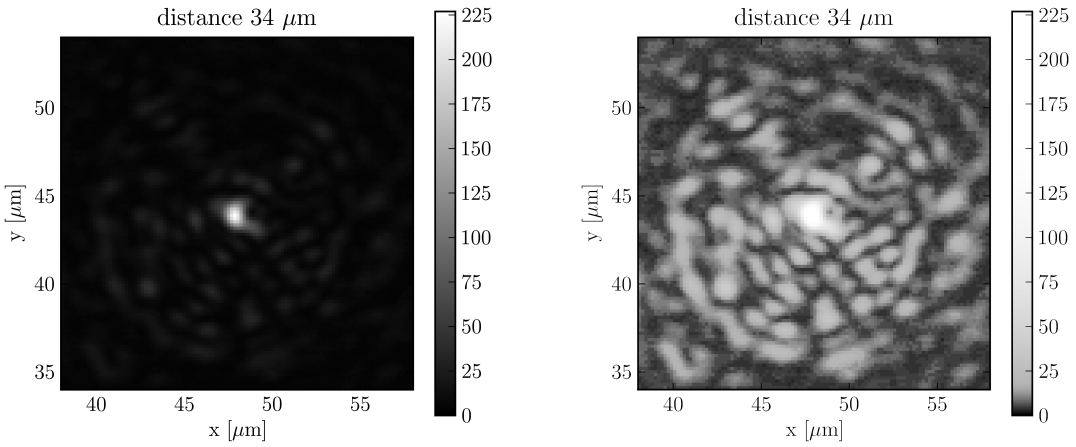

(a) (b)

Figure 5.14 – The intensity distribution in the focal plane 34μm away from the output facet of the microlens. A standard colourmap (a) and a colourmap modified to enhance the diffraction pattern visible around the focal spot (b). Wavelength of 850nm.

approximately elliptical shape. Most likely this is to be due to the phenomenon of elliptical focusing of a linearly polarised beam [48]. Full Width in Half Maximum (FWHM) along X axis is 0.9μm and FWHM along Y axis is 1.3μm. The intensity profiles in the focal plane along X and Y axes are shown in Fig. 5.15. Intensity distribution in the planes perpendicular to the optical axis just before and just behind the focal plane is presented in Fig. 5.16–5.19. One can see that the shape of the central spot is irregular and different at different planes. Maximum intensity in a given plane perpendicular to the optical axis as a function of the propagation distance is shown in Fig. 5.20. In all shown planes perpendicular to the optical axis, the central spot is surrounded by large number of much weaker spots. One may say that this is a diffraction pattern. The origin of this diffraction pattern might be related to the quantisation of the refractive index distribution. This quantisation makes the

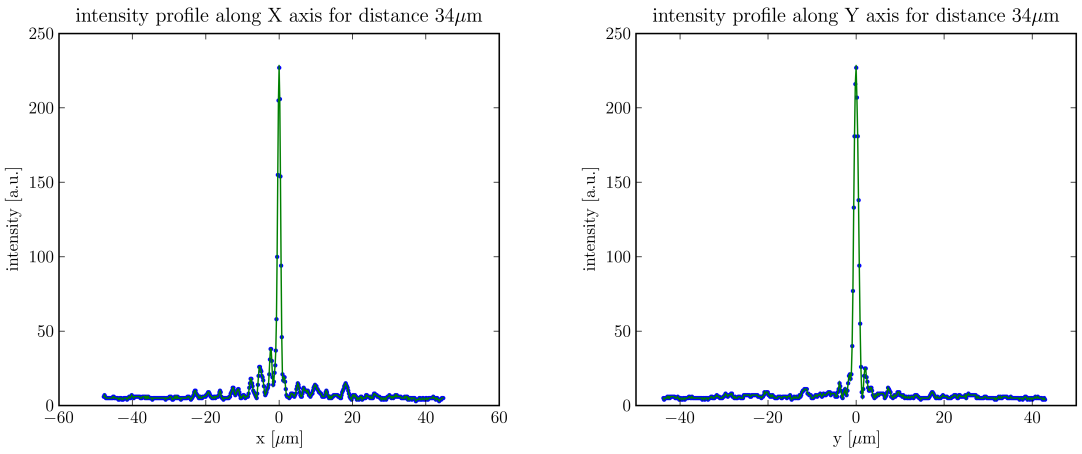

(a) (b)

Figure 5.15 – The intensity profiles along X axis (a) and Y axis (b) in the focal plane 34μm away from the output facet of the microlens. Wavelength of 850nm.

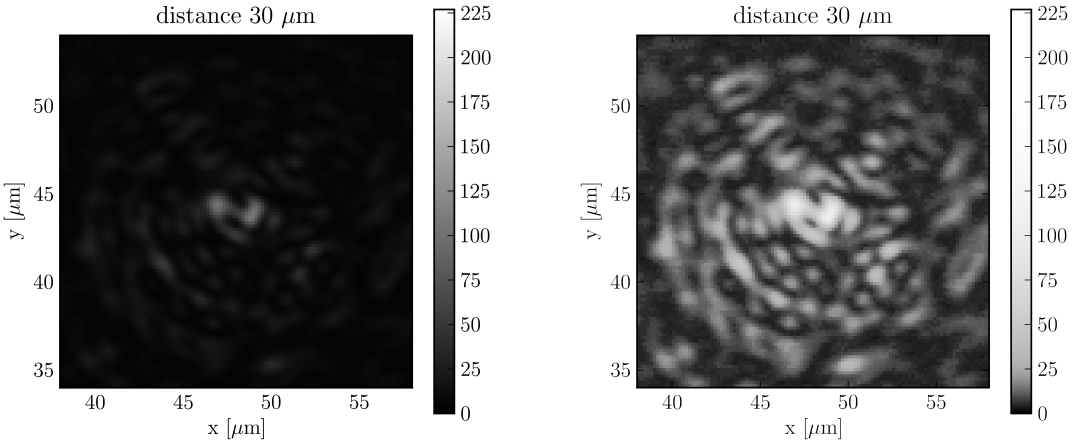

(a) (b)

Figure 5.16 – The intensity distribution in the plane 30μm away from the output facet of the microlens. A standard colourmap (a) and a colourmap modified to enhance the diffraction pattern visible around the central spot (b). Wavelength of 850nm.

characterised microlens similar, in a sense, to diffractive optical elements (DOEs) presented in the last chapter (see section 6.2).

5.5.2 Focusing properties measured using He-Ne laser 633nm

In this section the focusing properties of the microlens Lens2 has been described for the wavelength of 633nm. The maximum intensity has been measured 40μm away from the output facet of the microlens. This distance corresponds to the back focal length (working distance) related to the brightest focus. The focal plane is presented

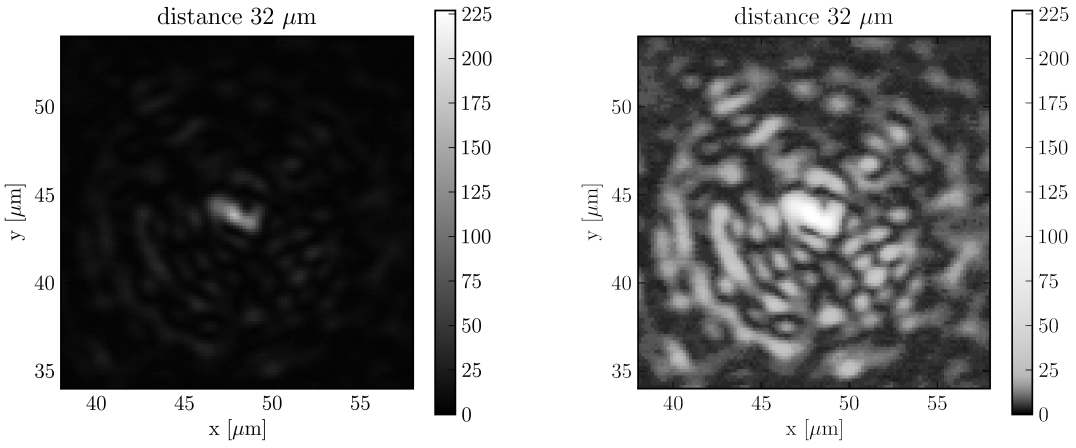

Figure 5.17 – The intensity distribution in the plane 32μm away from the output facet of the microlens. A standard colourmap (a) and a colourmap modified to enhance the diffraction pattern visible around the central spot (b). Wavelength of 850nm.

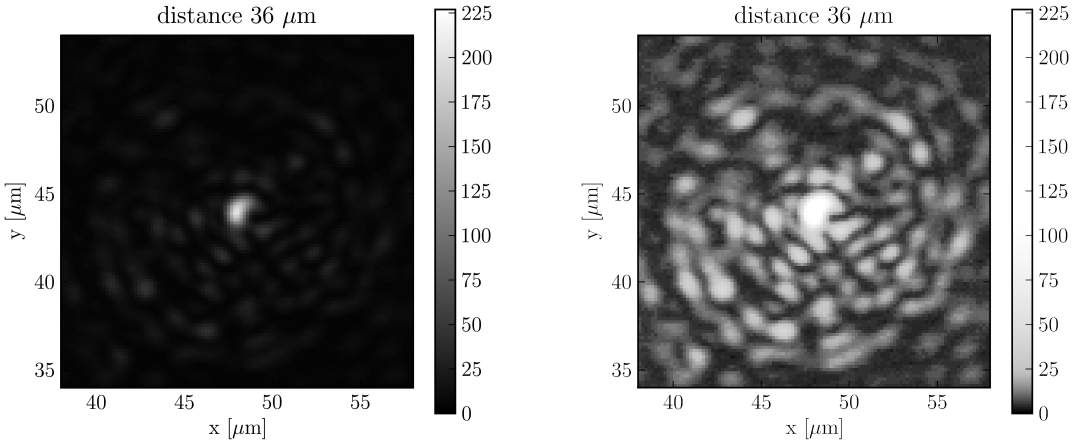

Figure 5.18 – The intensity distribution in the plane 36μm away from the output facet of the microlens. A standard colourmap (a) and a colourmap modified to enhance the diffraction pattern visible around the central spot (b). Wavelength of 850nm.

in Fig. 5.21. One can see that the focal spot has elliptical shape. Full Width in Half Maximum (FWHM) along the X axis is 0.9μm and FWHM along the Y axis is 1.2μm. The intensity profiles in the focal plane along X and Y axes are shown in Fig. 5.22

The intensity distribution in the planes perpendicular to the optical axis just before and just behind the focal plane is presented in Fig. 5.23–5.26. One can see that the shape of the central spot is irregular and also there are many spots around the central spot at every presented plane, which can be thought a diffraction pattern

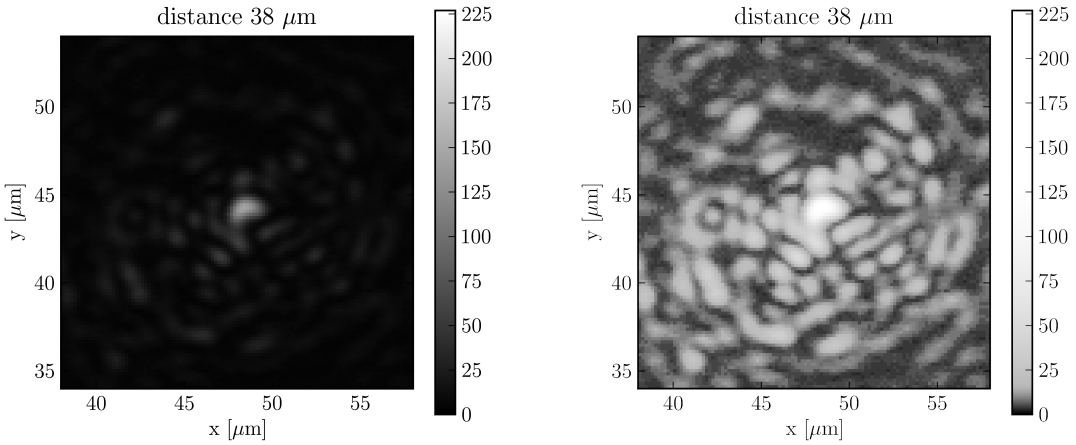

(a) (b)

Figure 5.19 – The intensity distribution in the plane 38μm away from the output facet of the microlens. A standard colourmap (a) and a colourmap modified to enhance the diffraction pattern visible around the central spot (b). Wavelength of 850nm.

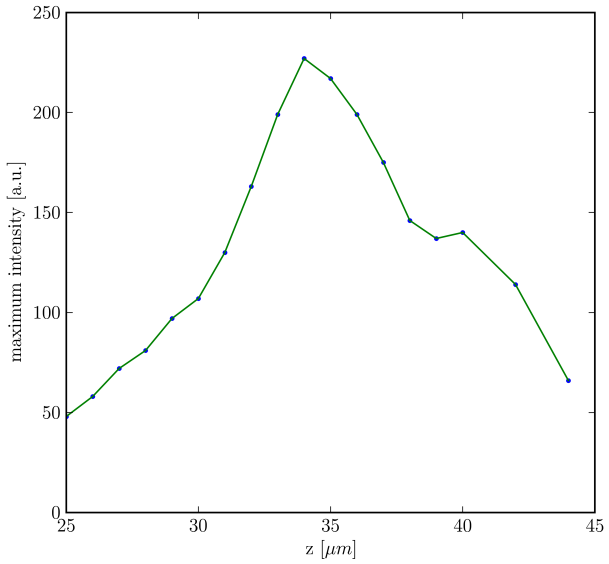

Figure 5.20 – Maximum intensity in a plane as a function of the propagation distance. Wavelength of 850nm.

as it was mentioned in the previous section. Maximum intensity in a given plane perpendicular to the optical axis as a function of the propagation distance is shown in Fig. 5.27

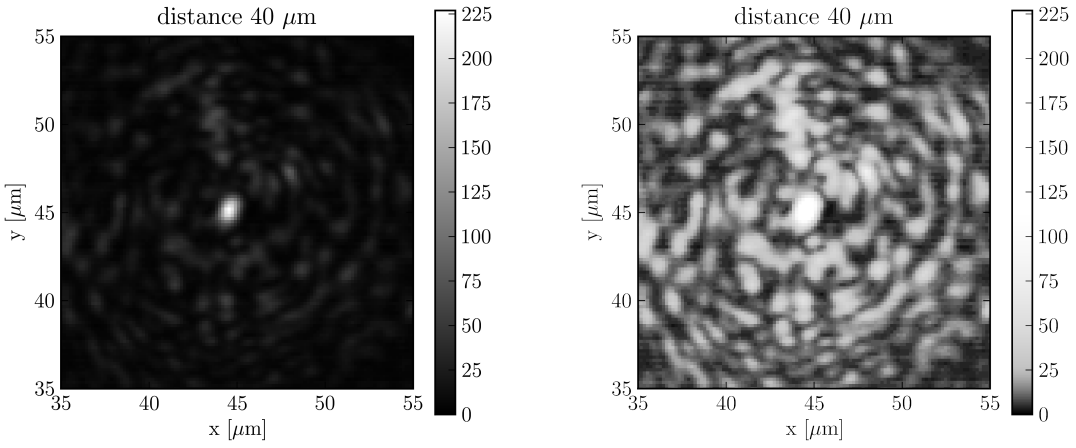

(a) (b)

Figure 5.21 – The intensity distribution in the focal plane 40μm away from the output facet of the microlens. A standard colourmap (a) and a colourmap modified to enhance the diffraction pattern visible around the focal spot (b). Wavelength of 633nm.

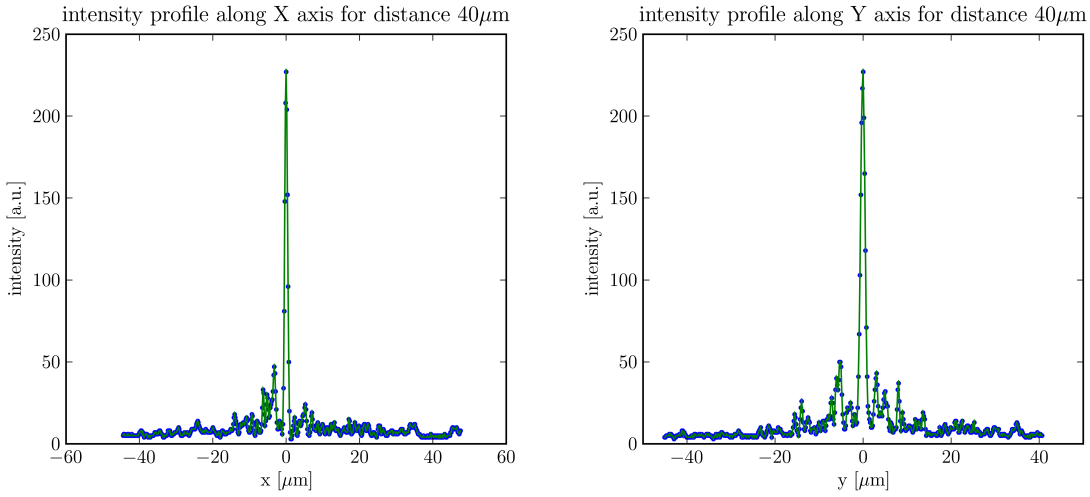

(a) (b)

Figure 5.22 – The intensity profiles along X axis (a) and Y axis (b) in the focal plane 40μm away from the output facet of the microlens. Wavelength of 633nm.

5.5.3 Focusing properties measured using diode laser 532nm

Finally the same measurements has been performed for the wavelength of 532nm. In this case the focusing phenomenon has significantly worse quality i.e. the exact position of the spot cannot be determined and a central spot is surrounded by a large number of relatively bright spots, which, most likely, create a diffraction pattern. The surrounding spots are much brighter for the wavelength of 532nm compared with the longer wavelengths.

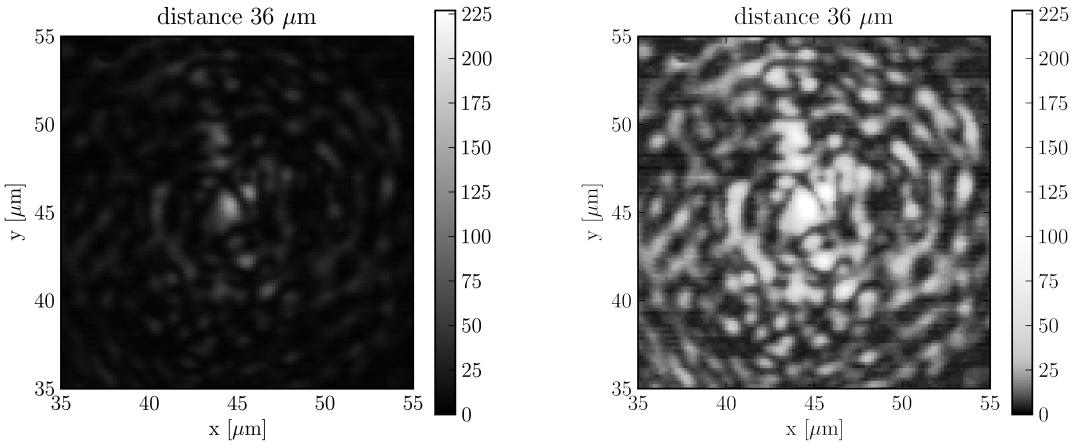

(a) (b)

Figure 5.23 – The intensity distribution in the plane 36μm away from the output facet of the microlens. A standard colourmap (a) and a colourmap modified to enhance the diffraction pattern visible around the central spot (b). Wavelength of 633nm.

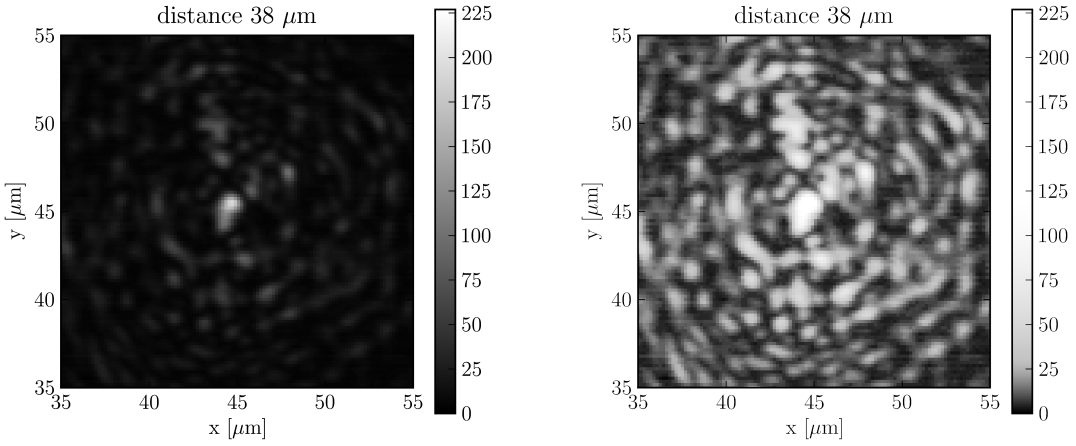

(a) (b)

Figure 5.24 – The intensity distribution in the plane 38μm away from the output facet of the microlens. A standard colourmap (a) and a colourmap modified to enhance the diffraction pattern visible around the central spot (b). Wavelength of 633nm.

The maximum intensity has been measured 16μm away from the output facet of the microlens. This distance corresponds to the back focal length (working distance) related to the brightest focus. The intensity distribution in the focal plane is shown in Fig. 5.28. The focal spot has elliptical shape. FWHM along X axis and Y axis are 0.7μm and 1.3μm respectively. It is easy to see that the contrast between a central spot and other spots in the focal plane is significantly lower compared to wavelengths 850nm and 633nm. Maximum intensity in a given plane perpendicular

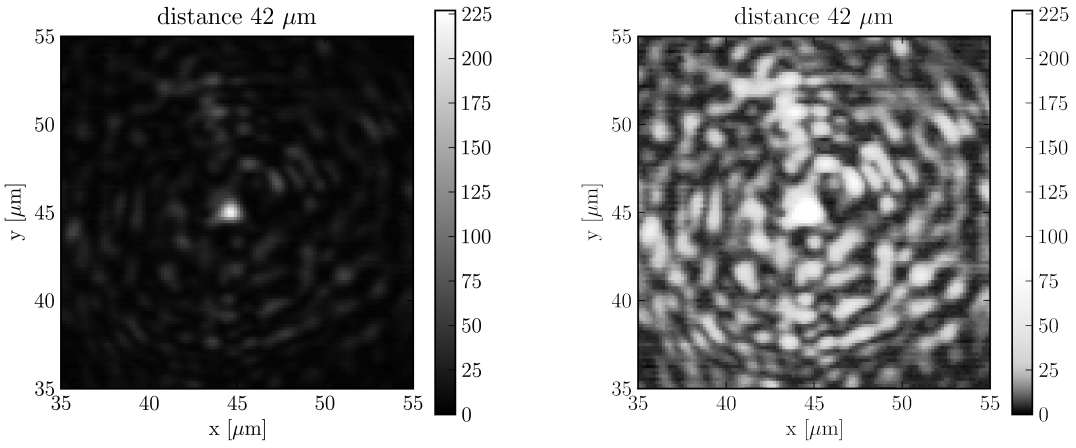

(a) (b)

Figure 5.25 – The intensity distribution in the plane 42μm away from the output facet of the microlens. A standard colourmap (a) and a colourmap modified to enhance the diffraction pattern visible around the central spot (b). Wavelength of 633nm.

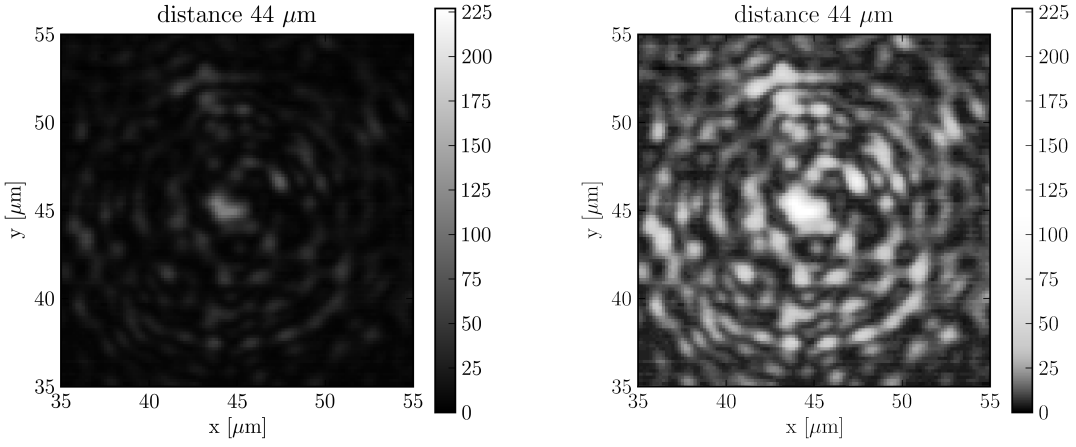

(a) (b)

Figure 5.26 – The intensity distribution in the plane 44μm away from the output facet of the microlens. A standard colourmap (a) and a colourmap modified to enhance the diffraction pattern visible around the central spot (b). Wavelength of 633nm.

to the optical axis as a function of the propagation distance is shown in Fig. 5.29. Focusing performance is relatively low for the wavelength of 532nm meaning that the focal spot is not 'clean' and this fact results in irregularity of the dependence shown in Fig. 5.29. Clearly the longer wavelength of illumination is utilised the better focusing performance is obtained. Most likely the focusing performance of the considered quantised microlens is closely related to the ratio of width of a single value refractive index zone to the wavelength.

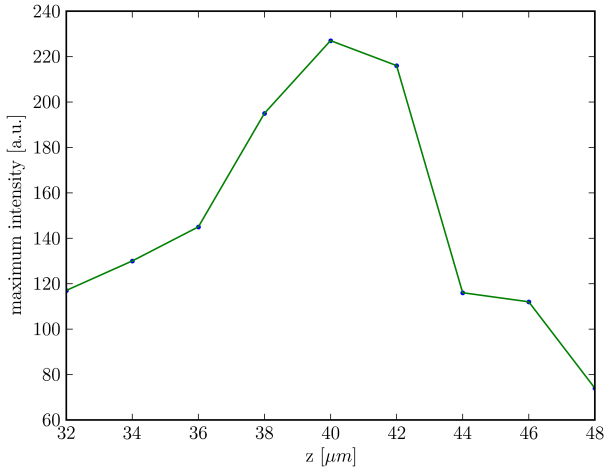

Figure 5.27 – Maximum intensity in a plane as a function of the propagation distance. Wavelength of 633nm.

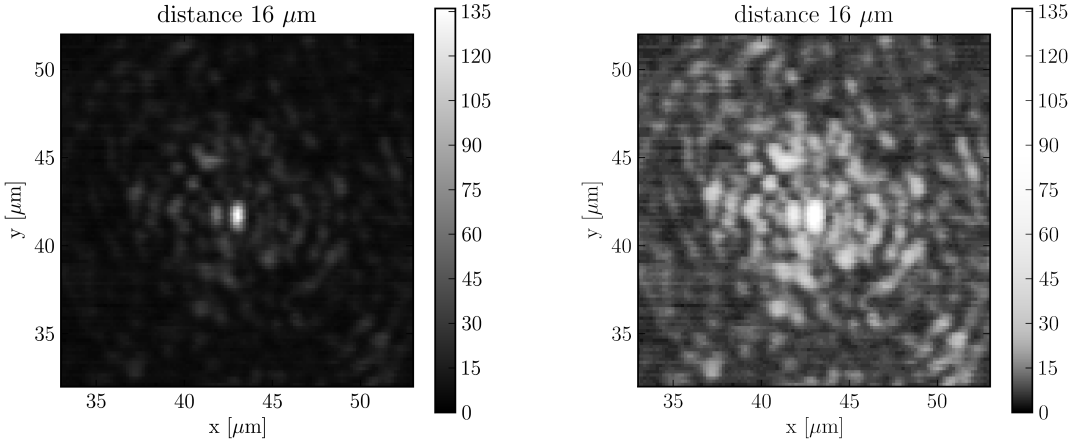

(a) (b)

Figure 5.28 – The intensity distribution in the focal plane 16μm away from the output facet of the microlens. A standard colourmap (a) and a colourmap modified to enhance the diffraction pattern visible around the focal spot (b). Wavelength of 532nm.

5.5.4 Summary of the experimental results

The experimental results confirm the expected optical performance of the fabricated microlens. The focal spot diameter is similar to that predicted for 850nm illumination and of the same order for 633nm. However for 633nm illumination this is larger than that predicted by theory . This may be due to the resolution of our optical measurement system with the nanostructured origin of the quantised lens also playing a role. The slightly elliptical shape of observed focal spots might be due to the linear polarisation of the incident light [48]. The observed working distances (back focal lengths) are approximately 50% smaller that those predicated by theory. This is primarily

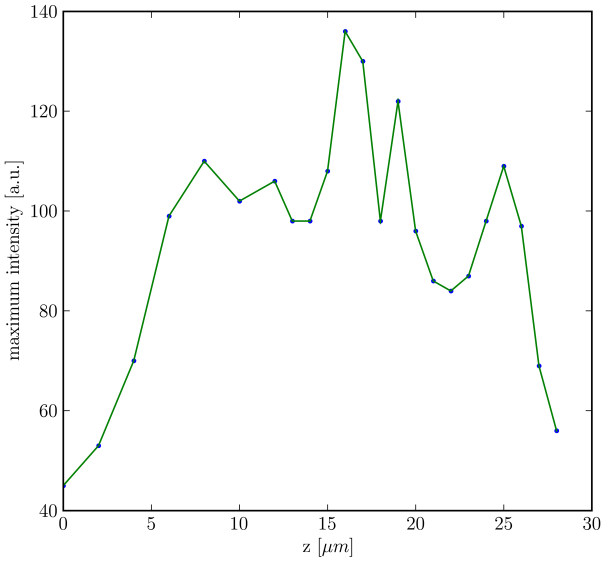

Figure 5.29 – Maximum intensity in a plane as a function of the propagation distance. Wavelength of 532nm.

due to the accuracy of our measurement system and the difficulties associated with determining precisely the surface of the microlens. By assuming we have a systematic error in the measurement of the working distance, the difference in working distances obtained for both the 850nm and 633nm illumination are in good agreement with predicted values.

For the wavelength of 532nm quality of focusing is significantly lower compared to the wavelengths 850nm and 633nm. Most likely it is caused by the fact that the sizes of the zones characterised by a single value of the refractive index are too large with respect to the wavelength of 532nm.

5.6 Conclusions

The design and fabrication of nanostructured microlenses, where a quasi-continuous refractive index gradient is produced by means of a nanometre scale composite of two mechanically and thermally compatible soft glasses, has been successfully demonstrated. The quantised approach, where a set of discrete refractive index structures are created and then combined to create a quantised refractive index profile, has been used to design and fabricate a 7–level microlens with a diameter of 100μm.

The fabricated lens shows good focusing properties with focal spot diameters of $0.9 \times 1.2\mu$m at the focus. This is in very good agreement with the simulated results for similar nanostructured lens designs. The working distance of the lens was observed to be 34μm and is 50% shorter than the working distance predicted by simulation.

As it has been mentioned in subsection 5.5.4 it is primarily due to the accuracy of our measurement system and the difficulties associated with determining precisely the surface of the microlens. The chromatic properties of the lens have also been verified with the fabricated lens showing good performance at both 850nm and 633nm. The working distances for 633nm and 850nm were observed to be 40μm and 34μm, respectively, while the focal spot sizes remain unchanged.

Chapter 6

Novel micro and nanostructured materials fabricated with stack-and-draw technique

The present chapter is divided into two main sections. Section 6.1 covers the concept and fabrication of the nanostructured birefringent material made using the modified stack-and-draw technique. The numerical and experimental verification of its optical properties has been performed by Andrew Waddie and it is also included here for the sake of completeness [52, 6, 49].

Section 6.2 is devoted to diffractive optical elements (DOEs) fabricated with the modified stack-and-draw technique. The fabrication and preliminary optical characterisation are reported [50]. DOEs considered in the section do not have subwavelength feature sizes but their fabrication is very similar to the fabrication of nGRIN microlenses and the nanostructured birefringent material.

The conclusions of the both main sections of the chapter are summarised in the section 6.3.

6.1 Nanostructured birefringent material fabricated with stack-and-draw technique

Exploitation of the modified stack-and-draw technique for fabrication of the nanostructured microlenses was described in chapters 3 and 5. However, the idea of the nanostructured optical element fabrication with the stack-and-draw technique can be extended beyond the microlens manufacture. The important advantage of the investigated in previous chapters nanostructured microlenses is the fact that their optical properties can be described within the frame of the effective medium theory (EMT). The second-order EMT introduced in section 2.3.2 is capable of predicting also the birefringence of the anisotropic nanostructured material shown in Fig. 6.1 [6, 49]. Such a birefringent nanostructured material can be manufactured using the modified stack-and-draw technique. The form birefringent material made of subwavelength in

thickness, alternate layers of two isotropic glasses gives a significant freedom to design artificial birefringence with needed phase retardation. Fabrication of competing nanostructured materials based on the same principle of operation generally requires the use of more expensive techniques i.e. direct electron beam litography [51]. The single optical element made with the stack-and-draw technology is relatively cheap because one can obtain thousands of elements out of the single preform.

6.1.1 Concept of the nanostructured birefringent material

As has been mention in section 2.3, birefringence can be caused by suitable arrangement of subwavelength in thickness layers of isotropic dielectric. Such birefringence is called the form birefringence. In this chapter the nanostructured birefringent material shown in Fig. 6.1 is considered [6, 49]. The structure consists of alternate, subwave-

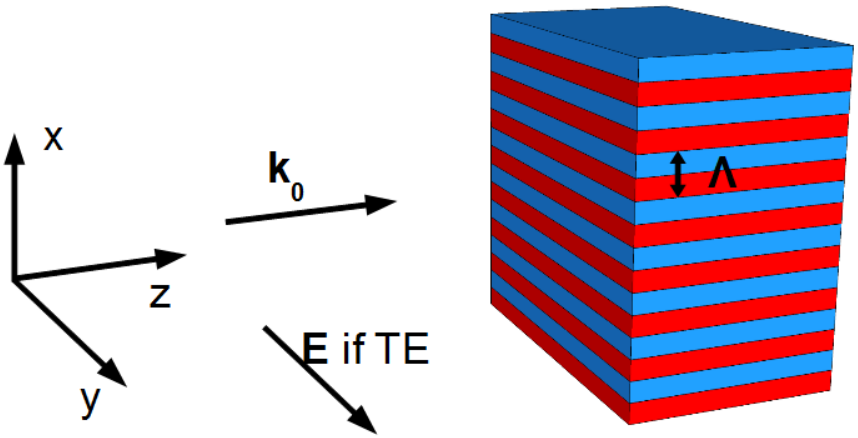

Figure 6.1 – Schematic of the nanostructured birefringent material. A direction of wave vector $\mathbf{k_0}$ of incident illumination is shown. A direction of electric field $\mathbf{E}$ in the case of TE polarisation is also shown.

length in thickness layers of two isotropic glasses with refractive indices $n_i = \sqrt{\epsilon_i}$ and $n_e = \sqrt{\epsilon_e}$. According to the second-order EMT described in section 2.3.2 optical properties of the considered nanostructured material are the same as the optical properties of homogenous anisotropic uniaxial medium with different refractive indices (or permittivities) for TE ($\mathbf{E} \parallel Y$axis) and TM ($\mathbf{H} \parallel Y$axis) polarisations [7, 6]. Critical parameters of such a nanostructured birefringent material, apart from the refractive indices of the constituent glasses, are the structure period Λ and the volume filling factor f of the dielectric with the permittivity of ϵ_i. Effective refractive indices for both polarsations are given by formulae (2.56) and (2.57). FDTD simulation results presented in section 6.1.3 show that these formulae are sufficiently accurate to calculate the phase retardation within the nanostructured birefringent element provided

the difference between refractive indices of the constituent glasses n_i and n_e is small enough. The FDTD modelling has been performed for a F2 i NC21A glasses with $n_i - n_e \approx 0.1$.

6.1.2 Fabrication of the nanostructured birefringent material

The fabrication procedure of the considered nanostructured birefringent material with the modified stack-and-draw technique is similar to the small-diameter nGRIN microlens fabrication procedure described in chapter 3. The most significant difference is related to the fact that the nanostructured birefringent material is periodic (Fig. 6.1). It is great facilitation in terms of the preform assembly compared to nGRIN microlenses.

Similarly to nGRIN microlens the birefringent material is an all-glass structure i.e. there are no air holes within the material. The nanostructured material consists of two glasses with different refractive indices. One has to choose a pair of glasses which is matched in terms of thermal and mechanical properties. For a proof-of-concept fabrication F2 glass made by Schott AG and NC21A glass made by Institute of Electronic Materials Technology (ITME) have been utilised. Weight composition and refractive indices of these glasses are given in Tab. 5.1 in chapter 5.

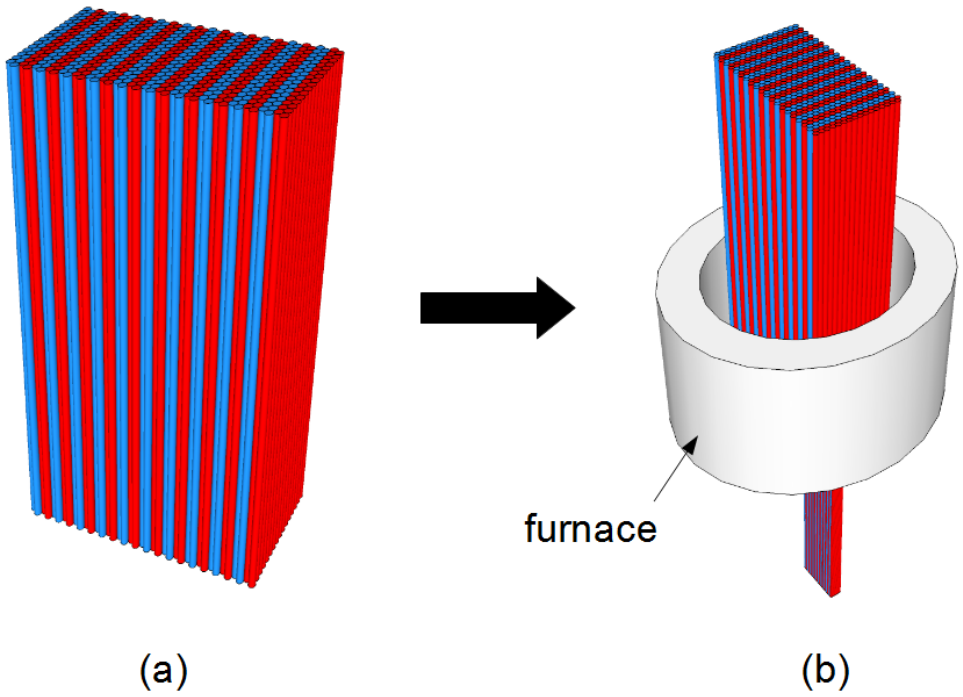

Figure 6.2 – Schematic of the fabrication procedure (Part 1).

The fabrication procedure can be summarised in the following steps.

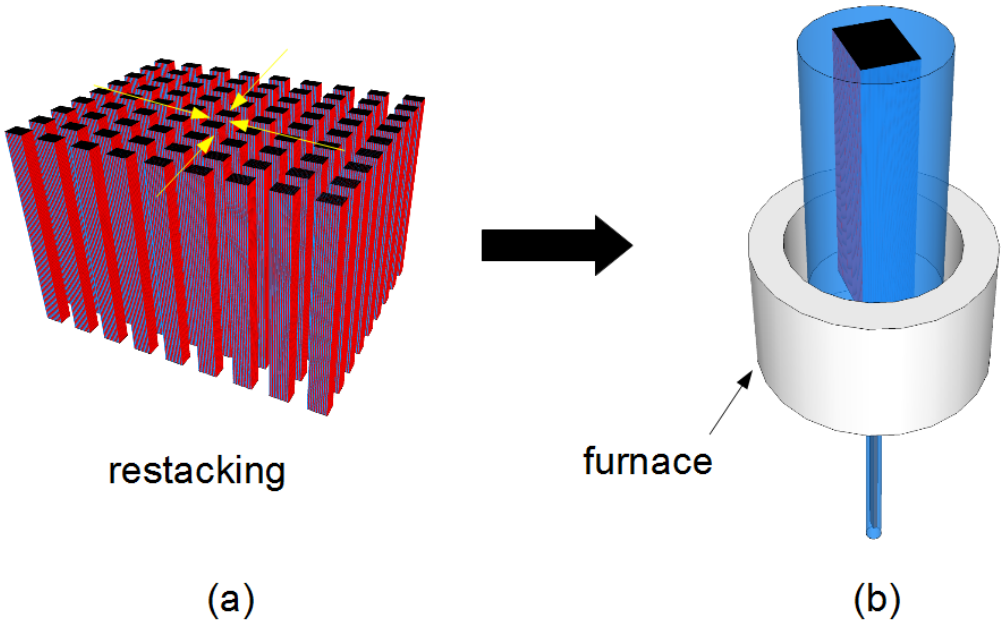

Figure 6.3 – Schematic of the fabrication procedure (Part 2).

1. Two glasses, characterised by different refractive indices and similar mechanical and thermal properties, are cast as long rectangular bars which are then cut, ground and polished to obtain rods with a round or rectangular cross-section.

2. These rods are then scaled down, using a fibre drawing tower, to a diameter of approximately 1mm.

3. A few hundreds to a few thousands of the rods obtained in the previous step are stacked together in order to assemble an initial preform (Fig. 6.2a).

4. The stacked initial preform is drawn-down in the high temperature (600–700°C) using the draw tower (Fig. 6.2b and Fig. 3.6).

5. Rods obtained in the drawing of the initial preform are stacked into an intermediate preform (restacking – Fig. 6.3a) . Additionally an outer glass tube and filling rods are utilised for constructing this intermediate preform (Fig. 6.3b).

6. The intermediate preform is drawn-down in the high temperature (600–700°C) using the draw tower (Fig. 6.3b).

7. The cross-section of the rod obtained in the drawing of the intermediate preform has to be scaled down further in the drawing process in order to reach subwavelength thickness of the single glass layer of approximately 300nm.

8. Final rod is cut into slices and then polished down to the desired thickness (from a few hundreds of microns to a few millimetres). Every slice is a slab of the nanostructured artificially birefringent material.

Photos of the intermediate preform and the preform used for final drawing are shown in Fig.6.4. As has been mentioned before, stacking of the initial and intermediate preforms is simplified compared to the case of nGRIN microlenses due to periodicity of the nanostructured birefringent material. The fabricated final nanos-

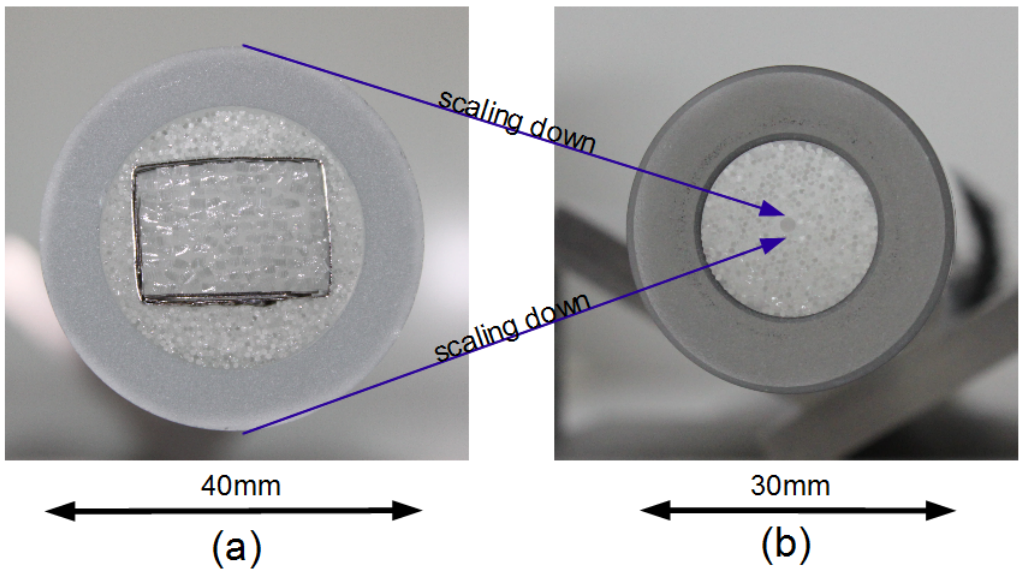

Figure 6.4 – Photos of the intermediate (a) and final (b) preform. The intermediate preform had been scaled down in the drawing process, and the obtained rod was utilised for constructing the final preform. This rod, containing the structure, was placed in the centre of the final preform, and it was surrounded by homogeneous filling rods and the outer tube. The idea is schematically shown by the blue arrows.

tructure has an active area approximately 35μm $\times$ 22μm in the cross-section with a single glass layer thickness of 300nm The same drawing tower has been used for the fabrication of the birefringent material as in the case of the nGRIN microlenses fabrication (see section 3.2.1). The issues related to the control over the drawing process are similar as well.

6.1.3 FDTD modelling of light propagation within nanostructured birefringent material

In order to verify applicability of the second order effective medium theory [7] and formulae (2.56) and (2.57) in the case of the considered nanostructured birefringent

material FDTD simulations has been performed [52, 6, 49]. The schematic of the simulated system is shown in Fig. 6.1. The FDTD simulations, presented in this section, were performed by Andrew Waddie [52] and are included in the thesis for the sake of completeness. All modelling results have been obtained for nanostructures made of F2 glass and NC21A glass. This pair of glasses has been utilised for the fabrication of the prototype birefringent material (Fig. 6.4).

Fig. 6.5 shows a comparison between the effective refractive indices $n_{\text{eff}}^{\text{TE}}$ and $n_{\text{eff}}^{\text{TM}}$ for both polarisations predicted by the second-order EMT and a fully vectorial FDTD simulations for a variety of nanostructures with the increasing filling factor f. The Maxwell-Garnet theory curve lies midway between the transverse electric (TE) and transverse magnetic (TM) curves and has been omitted for the sake of clarity. There is a good agreement between modelling results and the theoretical curves given by formulae (2.56) and (2.57). It is also clear that the largest difference between the effective refractive indices $n_{\text{eff}}^{\text{TE}}$ and $n_{\text{eff}}^{\text{TM}}$ occurs when $f = 0.5$. Further results concern the case with the filling factor f of 0.5 when all nanolayers in the material have the same thickness.

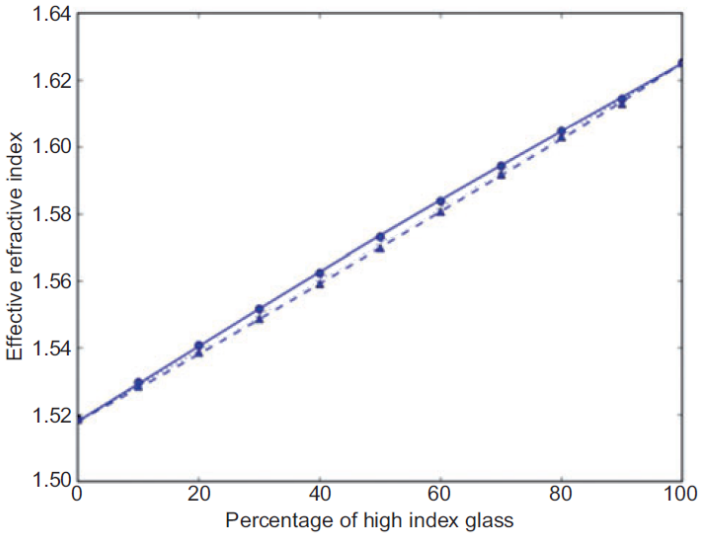

Figure 6.5 – Variation of effective refractive index for increasing proportion of high index glass (filling factor f) at wavelength of 1μm. Circle/solid shows the FDTD/second order effective medium theory results for TE polarisation and the triangle/dashed for TM polarisation [52, 49].

The next set of simulations has been performed in order to investigate how the birefringence Δn (defined as difference between the effective refractive indices $n_{\text{eff}}^{\text{TE}}$ and $n_{\text{eff}}^{\text{TM}}$) depends on the wavelength λ_0 and the structure period Λ. The simulations still concern the arrangement presented in Fig. 6.1. The birefringence Δn as a function of the wavelength for an infinite slab of the nanostructured birefringent material with grating period Λ of 250nm is presented in Fig. 6.6. The second-order effective medium

theory (solid blue) shows a good agreement with the fully vectorial results (blue dots). It is worth mentioning that the general trend of the curve is primarily determined by the relative differences between the glass dispersion curves (shown by the red line in Fig. 6.6).

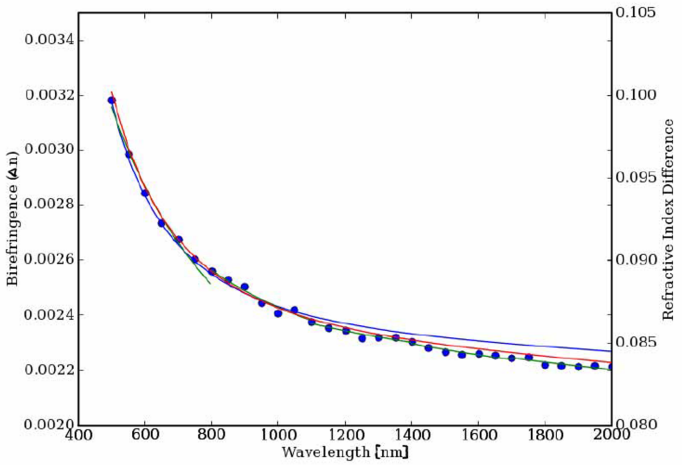

Figure 6.6 – Dependence of birefringence on wavelength of light for a 250nm structure period made of F2 and NC21A glasses. The second-order effective medium theory (solid blue) and the fully vectorial results (blue dots). The general trend matches that of the refractive index difference between the two constituent glasses (solid red) [52, 6].

Fig. 6.7 shows how the birefringence depends on the ratio Λ/λ_0 (grating period/wavelength). The scaled birefringence dn is plotted – the birefringence Δn divided by its peak value (taken from Fig. 6.6) for a given wavelength. FDTD modelling results are shown for four different wavelengths. It is clear that for a given wavelength, there is a definite threshold beyond which the expected level of birefringence is significantly reduced. This reduction in dn is due to the structure ceasing to operate as a true effective medium and instead beginning to function as a scalar domain diffraction grating - as shown by the inset figures for an incident wavelength of light of 1μm. It can be also seen that the value of the ratio Λ/λ_0 (grating period/wavelength) is not critical as long as it is approximately 0.5 or smaller. It means that, for a given wavelength, the birefringence Δn (defined as difference between the effective refractive indices $n_{\text{eff}}^{\text{TE}}$ and $n_{\text{eff}}^{\text{TM}}$) is independent of the grating period Λ as long as Λ/λ_0 (grating period/wavelength) is approximately 0.5 or smaller.

6.1.4 Experimental verification of nanostructured material birefringence

Experimental verification of the fabricated prototype nanostructured birefringent material has been performed using a set-up similar to the one proposed by Robertson [53].

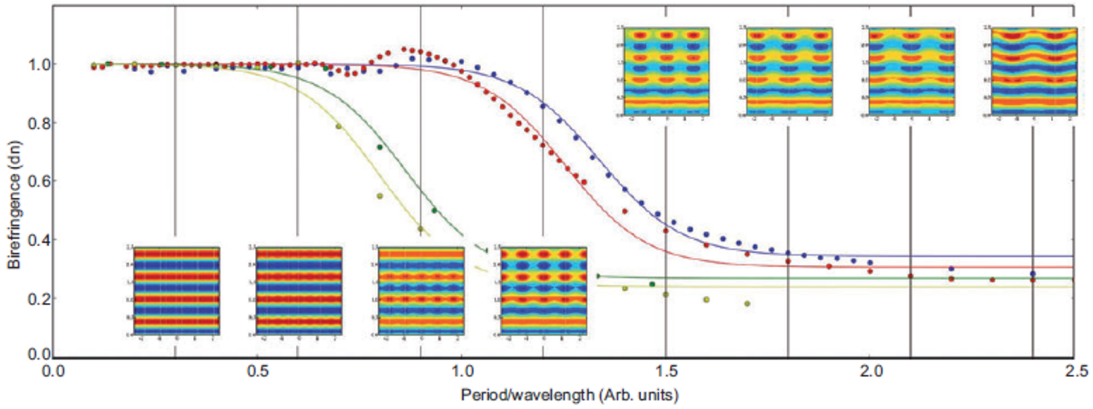

Figure 6.7 – FDTD simulations of nanostructured birefringent material for different wavelengths (500nm: yellow, 1000nm: green, 1500nm: red, 2000nm: blue). Dots show the numerical data points obtained with FDTD; solid lines were determined by fitting the sigmoid-like functions to the numerical data points. The scaled birefringence dn is plotted – the birefringence Δn divided by its peak value for a given wavelength. Inset images are electric field magnitudes within the structure for the wavelength of 1000nm – propagation direction up the page [52, 49].

A source of light with controlled direction of the linear polarisation, the test sample followed by a quarter wave plate, an output polariser and power meter are the key components of the utilised set-up, which is shown in Fig. 6.8. The experiment was performed by Andrew Waddie [6, 49] and its results are described here for the sake of completeness.

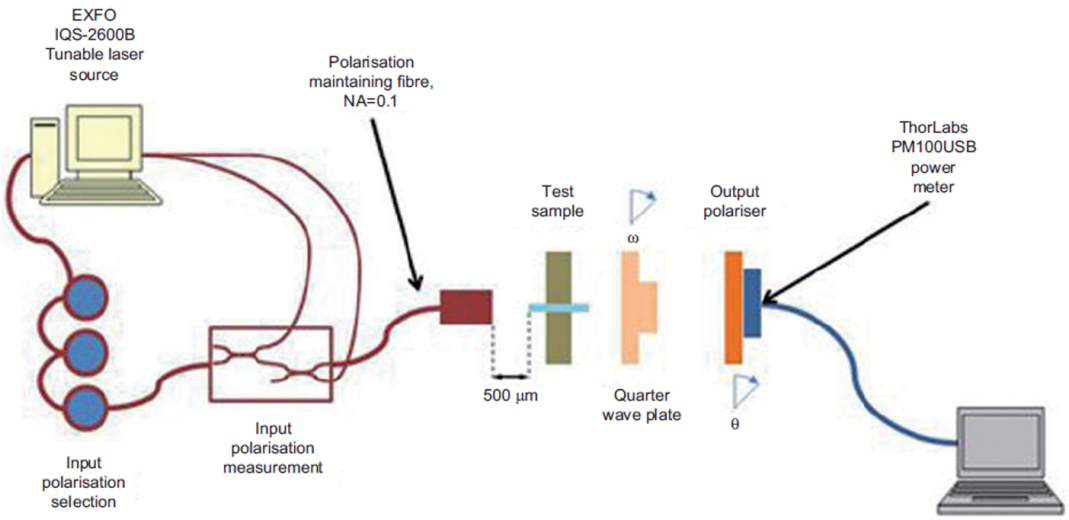

Figure 6.8 – Experimental set-up used for testing the fabricated nanostructured birefringent material [52, 49].

The angle of the test sample was held constant throughout the measurements. For a given input polarisation and the quarter wave plate angle ω one can measure

output polariser angle θ giving the minimum reading on the power meter. It is possible to determine how the angle θ depends on the he quarter wave plate angle ω. This relation has been numerically calculated using Jones vectors assuming the test sample properties given by the second-order effective medium theory. Comparison between numerical results and measured values of θ is presented in Fig 6.9. It can be seen that the measured values of θ follow the theoretical curves. The relatively small discrepancies between the modelled and experimental results for the lower curve are primarily due to the difference in the relative proportions of the two input polarisations in the lower experimental curve (210μW:17μW) compared to the relative proportions in the upper experimental curve (0.84μW:227μW). The larger admixture of the non-desired polarisation slightly shallows the leading edge while adding a small overall shift to the minimum angle.

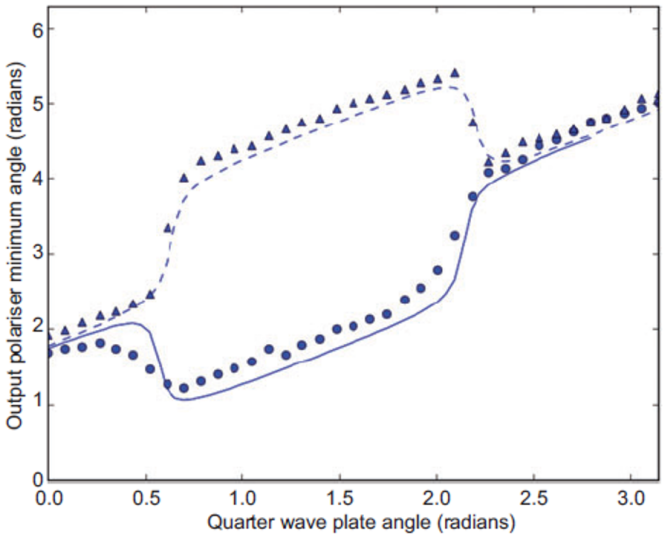

Figure 6.9 – Comparison between modelled and experimental variation of minimum intensity polarisation angle θ with quarter wave plate angle for two approximately orthogonal polarisations. Numerical results for these two polarisations are shown by the dashed and continuous lines. Triangles and circles denote corresponding experimental data for two polarisations [52, 49].

6.2 Diffractive optics development with stack-and-draw technique

Traditional diffractive optical elements (DOEs) are fabricated with microlitographic techniques [23]. With this method diffractive performance is obtained using a surface relief profile. It is common for some applications to coat this surface relief profile with additional layers of polymer to obtain a flat top surface. The ion exchange method has been used for DOE development [54, 55, 56, 57] as well as direct laser writing

methods [58, 59] In this thesis an alternative approach is explored. DOEs fabricated with the modified stack-and-draw technique are reported [50]. In the previous chapters the possibility of using this method for the fabrication of nanostructured GRIN microlenses is presented. Additionally the fabrication of nanostructured birefringent elements using the modified stack-and-draw technique is reported in section 6.1.

In the DOEs considered in this section, different phase shifts are attained using different types of glass and hence different refractive indices for different 'pixels' of the diffractive optical element. In the proof of concept trials two types of glass have been used, although, in principle, it is possible to use a larger number of glass types. The stack-and-draw technique allows the creation of arbitrary patterns of pixels. Moreover, such DOE elements have completely flat surfaces and they are robust and easy to integrate with other optical components. In order to demonstrate the new application of the modified stack-and-draw technique, periodic checkerboards with square and hexagonal lattices have been fabricated. Such structures might be used as beam splitters in the optical fiber systems. In this section, the fabrication technique and optical characteristics of the tested DOEs are presented.

6.2.1 Fabrication of DOE elements

The fabrication of the considered DOEs is based on the same principles as the fabrication of small-diameter nGRIN microlenses (see chapter 3) and the fabrication of nanostructured birefringent elements described earlier in this chapter. The most significant difference between the fabrication of the considered DOEs and the fabrication of the nanostructured elements investigated earlier in this thesis is the final feature size which is much larger in the case of DOEs.

The modified stack-and-draw technique consists of a few steps. First two or more types of glass are melted and then cast in the form of rectangular rods which are cut and polished. Square or round rods characterised by different refractive indices are obtained. These rods are about 3–5cm in diameter and it is possible to scale down their diameter down to about 1mm using a fibre drawing tower. Next, the scaled down rods are stacked according to the designed pattern into an initial preform (Fig. 6.10a). Each rod corresponds to one 'pixel' of the DOE. The number of the glass types corresponds to the number of the phase steps in the final element.

In this case, for the development of checkerboard structures, the in-house synthesised low-index silicate glass, NC21, and the commercially available, high-index lead-silicate glass, F2 have been used. Both glasses are thermally matched and have been used successfully for the development of the prototype large-diameter nGRIN microlerns (see chapter 5) and also a photonic crystal fibre [60].

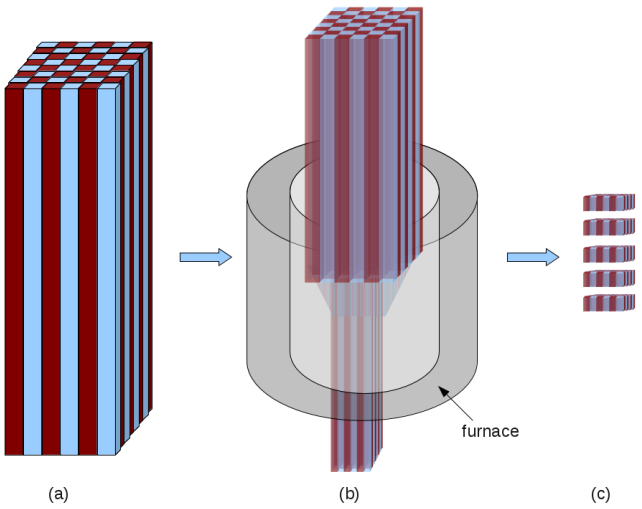

Figure 6.10 – Schematic of the fabrication procedure.

The initial preform is drawn using a fibre drawing tower (Fig. 6.10b). During the drawing the cross-section of the preform is scaled down by a linear factor of 10–30. The drawing process is performed at a relatively high temperature (600–700°C). Different glass types are drawn together and therefore it is necessary to utilise glass types which are thermally matched with each other. The obtained rods might be cut into slices, ground and polished down to the required thickness which is typically about 100μm (Fig. 6.10c). In this one-step process it is possible to fabricate DOE with a 'pixel' (feature) size of 20μm–100μm. If smaller feature size is needed the rods obtained during the first drawing can be restacked into an intermediate preform and then drawn again. This repeated stack-and-draw process allows to obtain feature sizes of few microns. The limiting factor is the diffusion process between the glasses. However, this can be taken into account during the design of the DOE.

As a proof of concept, three different checkerboards have been fabricated and tested. The checkerboards are periodic elements made of two types of glass with different refractive indexes. Two checkerboards were fabricated with a square lattice (Fig. 6.11). They have feature sizes of 46μm and 8μm, respectively and a refractive index difference of 0.101 for a wavelength of 589nm. The third structure was based on a hexagonal lattice (Fig. 6.12). For every type of tested DOEs two samples have been prepared, with thicknesses of 190μm and 270μm.

6.2.2 Measurements of diffraction patterns

To verify the performance of the fabricated DOEs, we have observed the far field diffraction patterns produced when the elements are illuminated with two lasers with wavelengths of 543.5nm and 632.8nm. The screen was $L = 270$cm away from DOE for

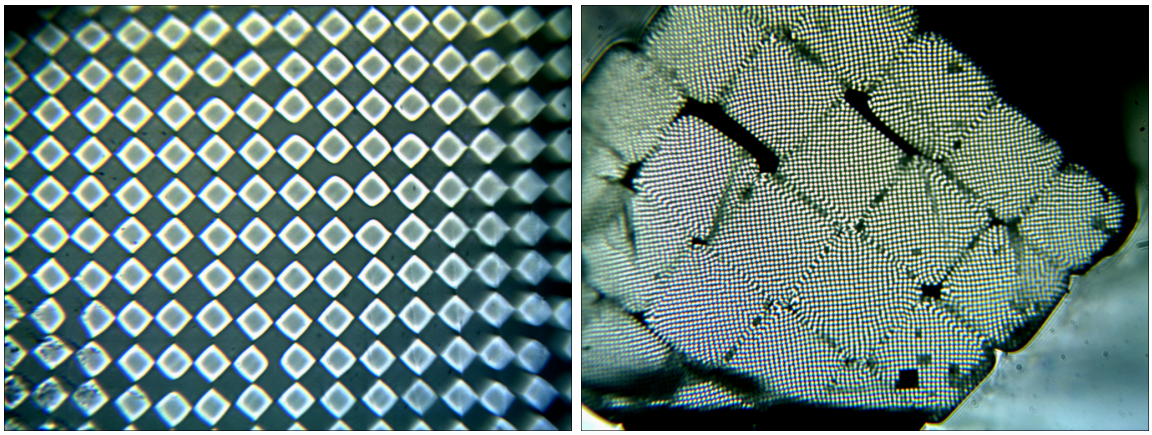

(a) (b)

Figure 6.11 – Photo of the square checkerboards with feature size of 46μm (a) and 8μm (b).

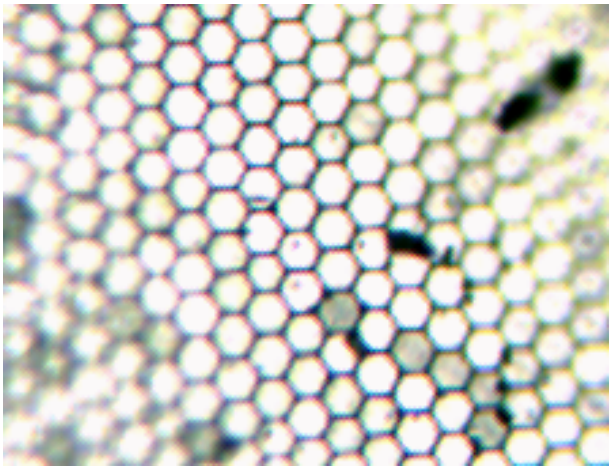

Figure 6.12 – Photo of the hexagonal checkerboard.

all measurements (Fig. 6.13). Since the thicknesses of the DOEs were not optimized for the illumination wavelengths, we can only verify the position of the diffraction orders not the intensity distribution between the orders.

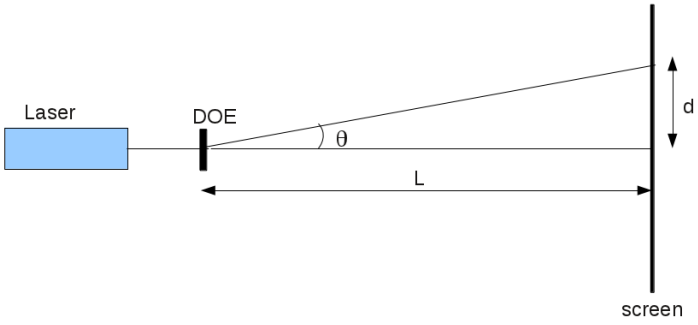

Figure 6.13 – Schematic of the experimental set-up.

A lattice pitch Λ and a diagonal lattice pitch Λ' are introduced for the square

checkerboard (Fig. 6.14a). According to this convention the feature size is equal to $\Lambda/2$. In the case of the square checkerboards a square array of bright spots on the screen (Fig. 6.14b) is obtained as a result of diffraction.

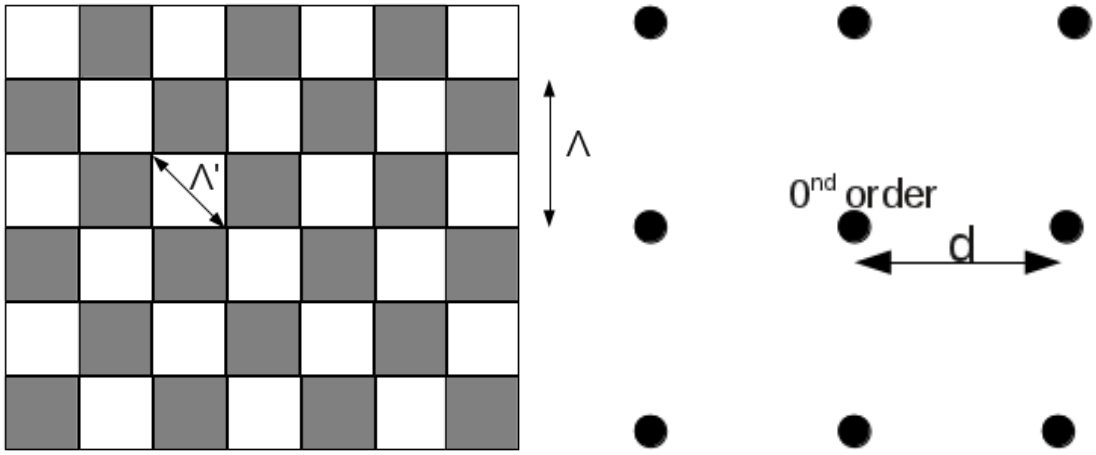

(a) (b)

Figure 6.14 – Layout of pixels in the square checkerboard (a). Schematic of the central part of the diffraction pattern for the square checkerboard (b).

The angle θ and the diagonal lattice pitch Λ' are related to the wavelength λ_0 by

$$\sin(\theta)\,\Lambda' = \lambda_0. \tag{6.1}$$

Since the angle θ is small it can be assumed that

$$\sin\theta \approx \theta \approx d/L. \tag{6.2}$$

Eq. (6.1) gives a condition for 1st order maximum. Using Eqs. (6.1), (6.2) and relation $\Lambda = \sqrt{2}\,\Lambda'$ it is possible to calculate the feature size from the diffraction pattern and then compare the result with a direct measurement.

The phase shift difference $\Delta\varphi$, introduced by the different refractive indices of the pixels in the checkerboard, is related to the refractive indices (n_1 and n_2) and the checkerboard thickness s by

$$\Delta\varphi = (n_1 - n_2)\frac{2\pi}{\lambda_0}s. \tag{6.3}$$

The refractive indices of the glasses F2 and NC21 are $n_1 = 1.62$ and $n_2 = 1.52$ respectively. In order to use the checkerboard as a 2x2 beam splitter, the desired $\Delta\varphi$ must be equal to π. Because of the relatively high refractive index difference ($n_1 - n_2 = 0.1$) this corresponds to an element thickness which is an odd multiple of $\sim 3\mu$m for a wavelength of ~ 600nm. It is difficult to control the element thickness to such a high degree of accuracy due to limitations in the polishing process. The next

set of test DOEs is planned to be fabricated using a pair of glasses with a much lower refractive index contrast of $\Delta n = 0.02$, such as the two in-house synthesised silicate glasses NC25 and NC21 [12].

A regular square array of diffraction fringes has been obtained with the square checkerboards with feature sizes of 46μm (Figs. 6.15 and 6.16). Using the data from the measurement of the diffraction pattern (Tab. 6.1) together with Eqs. (6.1), (6.2) and relation $\Lambda = \sqrt{2}\,\Lambda'$ one can calculate the pitch $\Lambda_{\text{exp}} = 92\mu$m of the DOE. This is very close to the value of $\Lambda = 93\mu$m, which has been obtained by direct measurement of the lattice pitch using an optical microscope.

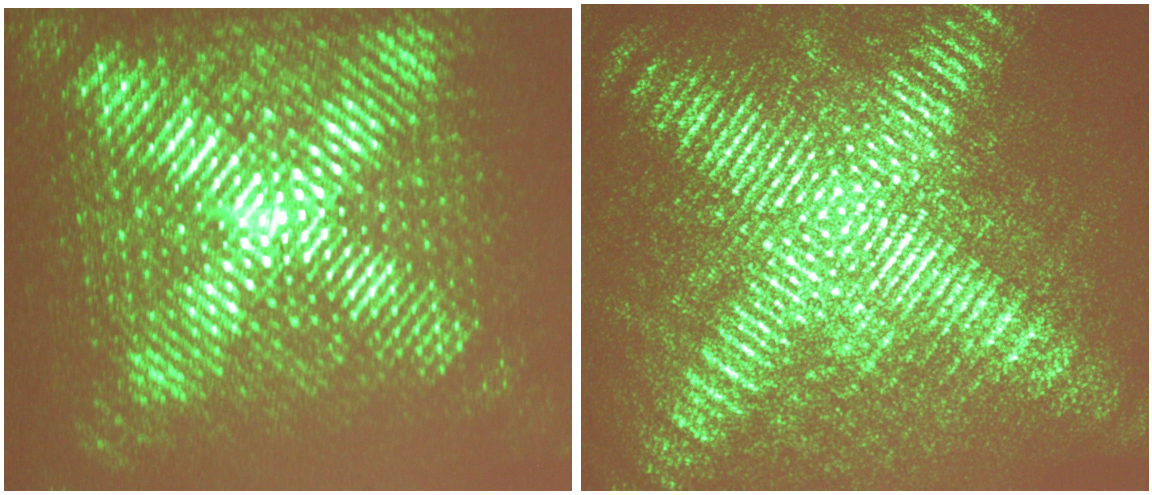

(a) (b)

Figure 6.15 – Diffraction patterns generated with 543.5nm laser and the square checkerboards with feature size of 46μm and thickness of 190μm and 270μm (b).

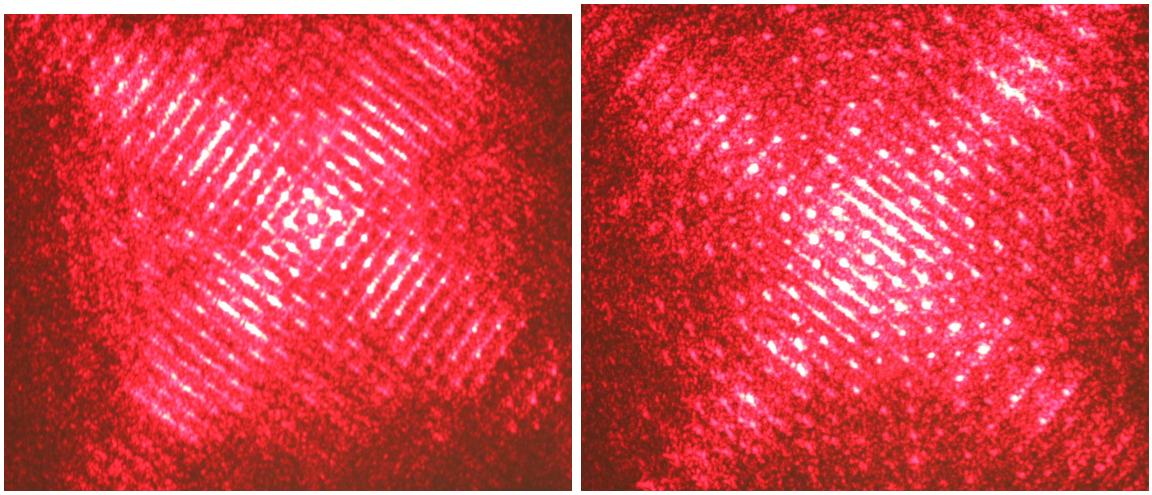

(a) (b)

Figure 6.16 – Diffraction patterns generated with 633nm laser and the square checkerboards with feature size of 46μm and thickness of 190μm and 270μm (b).

	d[mm]	d/L	θ [degrees]
$\lambda_0 = 543.5$nm thickness 190μm	22.5	0.0083	0.48
$\lambda_0 = 543.5$nm thickness 270μm	22.5	0.0083	0.48
$\lambda_0 = 633$nm thickness 190μm	26	0.0096	0.55
$\lambda_0 = 633$nm thickness 270μm	26.5	0.0098	0.56

Table 6.1 – Parameters of the diffraction pattern obtained for the square checkerboards with feature size of 46μm at the distance of 270cm.

Despite the distortions in the checkerboard structures which are shown in Fig. 6.11b, a regular square array of diffraction fringes has been obtained for the square checkerboards with a feature size of 8μm (Figs. 6.17 and 6.18). A similar set of measurements to those performed for the previous square checkerboards, yielded a calculated lattice pitch $\Lambda_{\text{exp}} = 15\mu$m from the measurement of the diffraction pattern (Tab. 6.2). This result is consistent with value $\Lambda = 16\mu$m measured directly using an optical microscope.

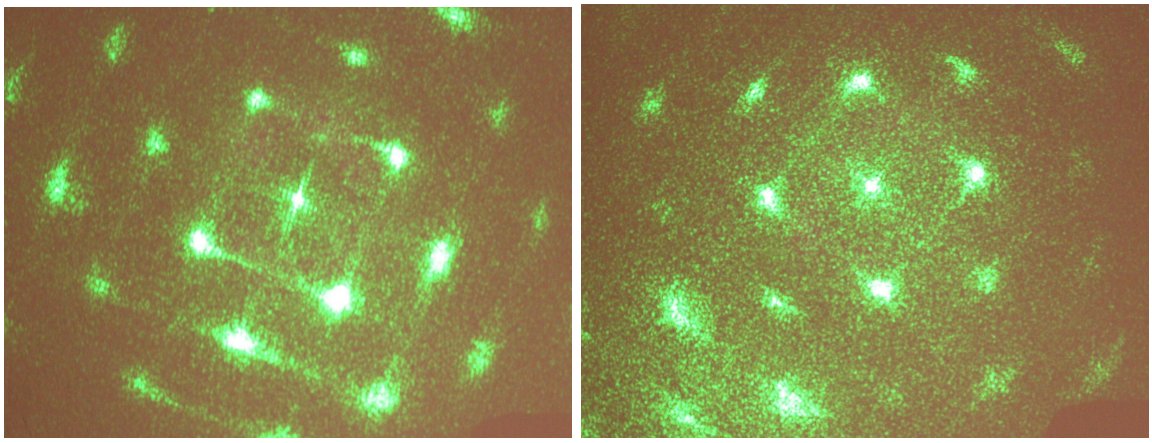

(a) (b)

Figure 6.17 – Diffraction patterns generated with 543.5nm laser and the square checkerboards with feature size of 8μm and thickness of 190μm and 270μm (b).

The hexagonal checkerboards have generated a regular hexagonal pattern of diffraction fringes (Fig. 6.19 and 6.20). Distances d between the 1$^{\text{st}}$ order maximum and the 0 order is given in Tab. 6.3.

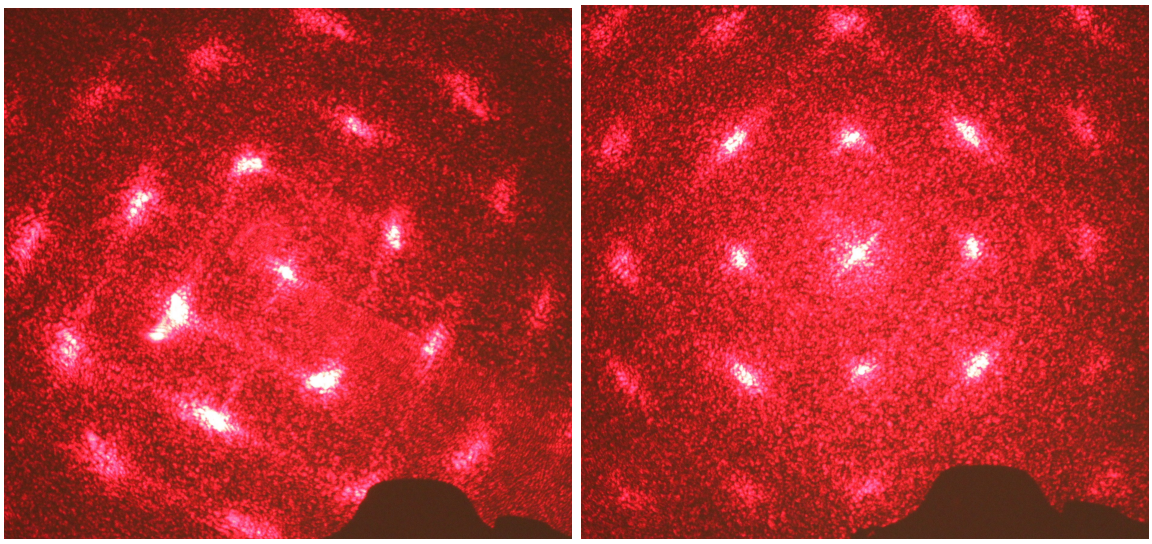

(a) (b)

Figure 6.18 – Diffraction patterns generated with 633nm laser and the square checkerboards with feature size of 8μm and thickness of 190μm and 270μm (b).

	d[mm]	d/L	θ [degrees]
$\lambda_0 = 543.5$nm thickness 190μm	135	0.050	2.86
$\lambda_0 = 543.5$nm thickness 270μm	137.5	0.051	2.92
$\lambda_0 = 633$nm thickness 190μm	160	0.059	3.39
$\lambda_0 = 633$nm thickness 270μm	161	0.060	3.41

Table 6.2 – Parameters of the diffraction pattern obtained for the square checkerboards with feature size of 8μm at the distance of 270cm.

6.3 Conclusions

In this chapter it has been described how to extend the use of the modified stack-and-draw technique beyond the fabrication of nanostructured microlenses. Successful development of the form birefringent nanostructured material has been reported. It has been numerically and experimentally shown that the fabricated birefringent nanostructured element can be described by the second-order effective medium theory. Applicability of the second-order EMT facilitates a rapid design of such birefringent components. The presented concept of the nanostructured birefringent material allows to customise chromatic properties of an birefringent element by choice of a

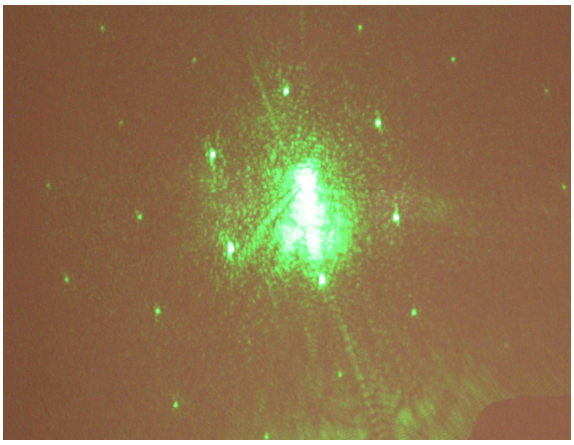

Figure 6.19 – Diffraction pattern generated with 543.5nm laser and the hexagonal checkerboard with thickness of 270μm.

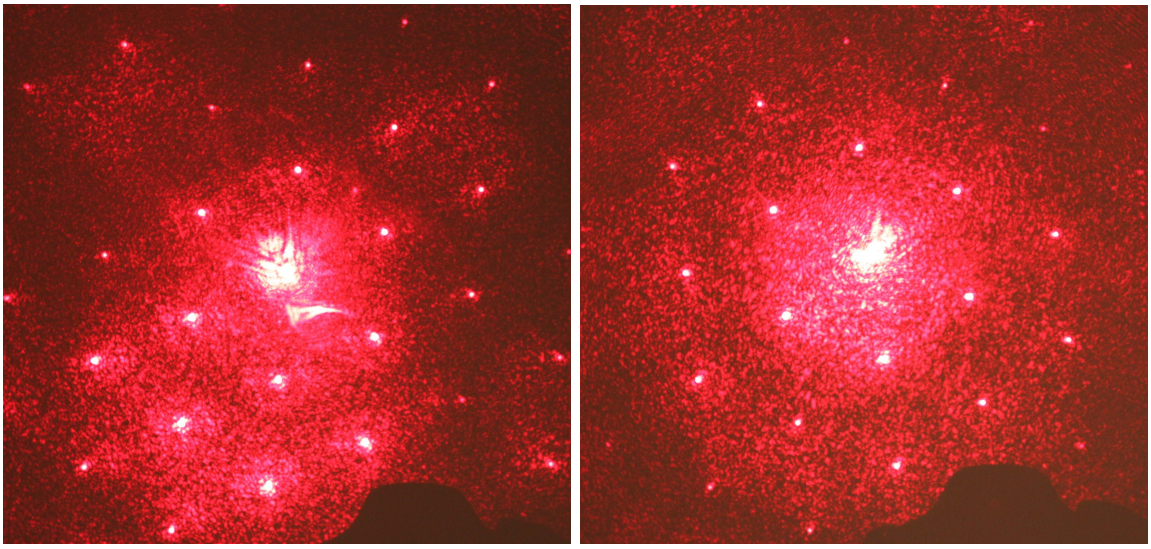

(a) (b)

Figure 6.20 – Diffraction patterns generated with 633nm laser and the hexagonal checkerboards with thickness of 190μm and 270μm (b).

	d[mm]	d/L	θ [degrees]
$\lambda_0 = 543.5$nm thickness 270μm	127.5	0.047	2.70
$\lambda_0 = 633$nm thickness 190μm	147.5	0.055	3.13
$\lambda_0 = 633$nm thickness 270μm	148.5	0.055	3.15

Table 6.3 – Parameters of the diffraction pattern obtained for the hexagonal checkerboards at the distance of 270cm.

suitable pair of constituent glasses. For example, it is possible to fabricate an element which operates as the quarter wave plate for a range of wavelengths [6]. Such an element can be useful when a tunable or broadband light source is exploited.

It has been also demonstrated that it is possible to fabricate flat, easy to integrate and robust diffractive optical elements using the modified stack-and-draw technique. It has been verified that the fabricated checkerboards generate regular diffraction patterns. The location of the diffraction orders is consistent with the values of structure lattice pitch measured using an optical microscope. When the phase shifts obtained with such a DOE are precisely controlled, the element can serve as a beam splitter used for coupling laser beam into a multicore optical fibre.

Chapter 7

Conclusions and outlook

7.1 Conclusions

As has been mentioned in the introduction (chapter 1), the main theme of the thesis and thereby its main goal was the numerical and experimental verification of the concept of the structured micro-optical elements fabricated with the modified stack-and-draw technique.

In chapter 4, it was demonstrated that, in terms of Gaussian beam propagation, the continuous GRIN microlens and corresponding nanostructured GRIN microlens are equivalent. It was also shown that standard paraxial GRIN theory gives a fairly good approximation of the Gaussian beam propagation in the high contrast nanostructured GRIN rod microlenses. The clear trend was observed that the accuracy of the standard paraxial GRIN theory improves with decreasing gradient parameter. One can calculate effective parameters of nanostructured GRIN microlenses using standard formulae from the scalar paraxial GRIN theory in order to fabricate nanostructured GRIN microlenses and use them in real systems with laser beam [11, 41].

Additionaly, in conclusion of the section 4.2, the FDTD simulation of Gaussian beam collimation shows that the far field divergence half-angle is reduced by the nGRIN microlens with the ideal quarter-pitch thickness from 10.1° to 3.3° and that ±10% inaccuracy of the microlens thickness leads to roughly 10% increase in a final far field divergence.

Chapter 5 covers numerical and experimental verification of the large-diameter quantised nGRIN microlens focusing performance and also the prototype microlens fabrication is reported. The design and fabrication of nanostructured microlenses, where a quasi-continuous refractive index gradient is produced by means of a nanometre scale composite of two mechanically and thermally compatible soft glasses, was successfully demonstrated. The quantised approach, where a set of discrete refractive index structures are created and then combined to create a quantised refractive index

profile, was used for the design and fabrication of a 7–level microlens with a diameter of 100μm.

According to FFT-BPM modelling results significant improvement of the focusing performance due to diameter reduction is observed in the case of the quantised microlens. One can conclude that the quantised microlens with a diameter of the order of 100μm and a 7–level refractive index profile ensures good optical performance for vacuum wavelength of 850nm. FFT-BPM simulations of the fabricated quantised microlens and its unquantised counterpart showed that the working distance for the quantised microlens lies within 5% of that of the ideal lens and there is a variation of around 9% over a wavelength range of 200nm (633nm–850nm)[37].

The experimental results confirmed the expected optical performance of the fabricated microlens. The fabricated lens shows good focusing properties with focal spot size of $0.9 \times 1.2\mu$m at the focus. The focal spot size is similar to that predicted for 850nm illumination and of the same order for 633nm. However for 633nm illumination this is larger than that predicted by theory . This may be due to the resolution of our optical measurement system with the nanostructured origin of the quantised lens also playing a role. The slightly elliptical shape of observed focal spots is likely to be due to the linear polarisation of the incident light [48]. The working distance of the lens was observed to be 34μm and is 50% shorter than the working distance predicted by simulation. It is primarily due to the inaccuracy of our measurement system and the difficulties associated with determining precisely the surface of the microlens. Assuming we have a systematic error in the measurement of the working distance, the difference in working distances obtained for both the 850nm and 633nm illumination are in good agreement with predicted values. The working distances for 633nm and 850nm were observed to be 40μm and 34μm, respectively, while the focal spot sizes remain unchanged [37].

In chapter 6, it was described how to extend the use of the modified stack-and-draw technique beyond the fabrication of nanostructured microlenses. Successful development of the form birefringent nanostructured material was reported. It was numerically and experimentally shown that the fabricated birefringent nanostructured element can be described by the second-order effective medium theory. Applicability of the second-order EMT facilitates a rapid design of such birefringent components [6, 49].

It was also demonstrated that it is possible to fabricate flat, easy to integrate and robust diffractive optical elements using the modified stack-and-draw technique. It was verified that the fabricated checkerboards generate regular diffraction patterns. The location of the diffraction orders is consistent with the values of structure lattice pitch measured using an optical microscope [50].

7.2 Future work

One of the future challenges, one needs to face in order to break current limitations of the technology, is related to automation of the preform assembly. A prototype of an automated rod stacker has been built but the low tolerance to the glass rod imperfections (such as a diameter spread) still needs to be addressed. However, one may say that the development of the system for automatic preform assembly is a matter of time and money.

The possibility of control over chromatic properties of the micro and nanostructured elements by means of the choice of glass pair with suitable chromatic dispersions curves can be investigated. Also the feasibility of fabricating achromatic nanostructured microlenses and wave plates for broadband or tunable light sources is very appealing to the optical industry.

Nanostructured GRIN microlenses with a non-radial effective refractive index distribution in the cross-section can be used for edge-emitting laser diode beam shaping. In particular, an elliptical GRIN microlens is useful for coupling of light generated by edge-emitting laser diode into a fibre. Such a lens has been already investigated both numerically and experimentally in paper [12]. The modified stack-and-draw technique allows to fabricate also nanostructured vortex microlenses. Vortex lenses are an example of optical elements with a number of applications e.g. in particle trapping and microscopy. The fabrication method considered in this thesis is suitable for axicon microlens development. Such nanostructured axicon microlenses have the potential to be exploited in the field of medical endoscopy because of their large depth of field. The large depth of field facilitates obtaining sharp images when the control over camera-object distance is poor.

Another task is to test methods of integration and alignment nanostructured elements with other photonic components such as lasers and fibres, as almost all real life applications of the micro-optical elements require stable integration with the larger optical system.

References

[1] D. Marcuse, *Light Transmission Optics.* New York: Van Nostrand Reinhold Company, 1972.

[2] B. A. E. Saleh and M. C. Teich, *Fundamentals of Photonics.* John Wiley and Sons, 1991.

[3] C. Gomez-Reino, M. V. Perez, and C. Bao, *Gradient-Index Optics: Fundamentals and Applications.* Berlin: Springer, 2002.

[4] A. E. Siegman, *Lasers.* Mill Valey: University Science Books, 1986.

[5] K. Okamoto, *Fundamentals of Optical Waveguides.* San Diego: Academic Press, 2000.

[6] A. J. Waddie, R. Buczynski, F. Hudelist, J. Nowosielski, D. Pysz, R. Stepien, and M. R. Taghizadeh, "Form birefringence in nanostructured micro-optical devices," *Opt. Mater. Express*, vol. 1, pp. 1251–1261, Nov 2011.

[7] I. Richter, P.-C. Sun, F. Xu, and Y. Fainman, "Design considerations of form birefringent microstructures," *Appl. Opt.*, vol. 34, pp. 2421–2429, May 1995.

[8] A. Sihvola, *Electromagnetic Mixing Formulas and Applications.* London: The Institution of Electrical Engineers, 1999.

[9] L. D. Landau and E. M. Lifshitz, *Electrodynamics of Continuous Media.* Course Theor. Phys., Oxford: Pergamon Press, 1960.

[10] F. Hudelist, R. Buczynski, A. J. Waddie, and M. R. Taghizadeh, "Design and fabrication of nano-structured gradient index microlenses," *Optics Express*, vol. 17, pp. 3255–3263, 2009.

[11] J. M. Nowosielski, R. Buczynski, F. Hudelist, A. J. Waddie, and M. R. Taghizadeh, "Nanostructured GRIN microlenses for Gaussian beam focusing," *Optics Communications*, vol. 283, no. 9, pp. 1938–1944, 2010.

[12] F. Hudelist, J. M. Nowosielski, R. Buczynski, A. J. Waddie, and M. R. Taghizadeh, "Nanostructured elliptical gradient-index microlenses," *Optics Letters*, vol. 35, no. 2, pp. 130–132, 2010.

[13] A. Taflove and S. C. Hagness, *Computational Electrodynamics: The Finite-Difference Time-Domain Method*. Boston: Artech House, second ed., 2000.

[14] M. N. O. Sadiku, *Numerical Techniques in Electromagnetics*. Boca Raton: CRC Press, 2001.

[15] S. G. Johnson. Nanostructures and Computation Wiki at MIT website: `http://ab-initio.mit.edu/wiki/index.php/Yee_lattice`.

[16] J. W. Goodman, *Introduction to Fourier Optics*. MaGraw-Hill, 2nd ed., 1996.

[17] N. Morton, "Gradient refractive index lenses," *Physics Education*, vol. 19, pp. 86–90, 1984.

[18] D. T. Moore, "Gradient-index optics: a review," *Applied Optics*, vol. 19, no. 7, pp. 1035–1038, 1980.

[19] N. Soodbiswas and A. B. S. K. Sarkar, "Radial GRIN glasses in Li2O-Na2O-Al2O3-TiO2-SiO2 systems," *Journal of Materials Science*, vol. 33, pp. 5401–5403, 1998.

[20] B. Messerschmidt, T. Possner, and R. Goering, "Colorless gradient-index cylindrical lenses with high numerical apertures produced by silver-ion exchange," *Applied Optics*, vol. 34, no. 34, pp. 7825–7830, 1995.

[21] S. N. Houde-Walter and D. T. Moore, "Delta-n control in GRIN glass by additives in AgCl diffusion bath," *Applied Optics*, vol. 25, no. 19, pp. 3373–3378, 1986.

[22] H. Ottevaere, R. Cox, H. P. Herzig, T. Miyashita, K. Naessens, M. Taghizadeh, R. Volkel, H. J. Woo, and H. Thienpont, "Comparing glass and plastic refractive microlenses fabricated with different technologies," *Journal of Optics A: Pure and Applied Optics*, vol. 8, pp. S407–S429, 2006.

[23] S. Sinzinger and J. Jahns, *Microoptics*. Weinheim, Germany: Wiley-VCH, second ed., 2003.

[24] S. Sinzinger, K. Brenner, J. Moisel, T. Spick, and M. Testorf, "Astigmatic gradient-index elements for laser-diode collimation and beam shaping," *Applied Optics*, vol. 34, no. 29, pp. 6626–6632, 1995.

[25] W. A. Reed, M. F. Yan, and M. J. Schnitzer, "Gradient-index fiber-optic microprobes for minimally invasive in vivo low-coherence interferometry," *Optics Letters*, vol. 27, no. 20, pp. 1794–1796, 2002.

[26] C. Ye and R. R. McLeod, "Grin lens and lens array fabrication with diffusion-driven photopolymer," *Optics Letters*, vol. 33, no. 22, pp. 2575–2577, 2008.

[27] S. P. Wu, E. Nihei, and Y. Koike, "Large radial graded index polymer," *Applied Optics*, vol. 35, no. 1, pp. 28–32, 1996.

[28] E. Centeno and D. Cassagne, "Graded photonic crystals," *Opt. Lett.*, vol. 30, pp. 2278–2280, Sep 2005.

[29] H. Kurt, E. Colak, O. Cakmak, H. Caglayan, and E. Ozbay, "The focusing effect of graded index photonic crystals," *Applied Physics Letters*, vol. 93, no. 17, p. 171108, 2008.

[30] C. Tan, T. Niemi, C. Peng, and M. Pessa, "Focusing effect of a graded index photonic crystal lens," *Optics Communications*, vol. 284, no. 12, pp. 3140 – 3143, 2011.

[31] J. D. Joannopoulos, S. G. Johnson, J. N. Winn, and R. D. Meade, *Photonic Crystals: Molding the Flow of Light (Second Edition)*. Princeton University Press, 2 ed., Feb. 2008.

[32] D. W. Prather, A. Sharkawy, S. Shi, J. Murakowski, and G. Schneider, *Photonic Crystals, Theory, Applications and Fabrication*. John Wiley and Sons, 2009.

[33] D. Pysz, I. Kujawa, P. Szarniak, M. Franczyk, R. Stepien, and R. Buczynski, "Multicomponent glass fiber optic integrated structures," *Proceedings SPIE*, vol. 5951, 2005.

[34] I. P. Kaminow, T. Li, and A. E. Willner, eds., *Optical Fiber Telecommunications V A: Components and Subsystems*, ch. 14, pp. 485–522. Academic Press, 2008.

[35] P. Russell, "Photonic crystal fibers," *Science*, vol. 299, no. 5605, pp. 358–362, 2003.

[36] GRINTECH GmbH website `www.grintech.de`.

[37] J. Nowosielski, R. Buczynski, A. J. Waddie, A. Filipkowski, D. Pysz, A. McCarthy, R. Stepien, and M. R. Taghizadeh, "Large diameter nanostructured gradient index lens," *Opt. Express*, vol. 20, pp. 11767–11777, May 2012.

[38] J. C. Knight, "Photonic crystal fibres," *Nature*, vol. 424, pp. 847–851, 2003.

[39] X. Feng, T. Monro, P. Petropoulos, V. Finazzi, and D. Hewak, "Solid microstructured optical fiber," *Opt. Express*, vol. 11, pp. 2225–2230, Sep 2003.

[40] F. Luan, A. K. George, T. D. Hedley, G. J. Pearce, D. M. Bird, J. C. Knight, and P. S. J. Russell, "All-solid photonic bandgap fiber," *Opt. Lett.*, vol. 29, pp. 2369–2371, Oct 2004.

[41] J. M. Nowosielski, R. Buczynski, F. Hudelist, A. Waddie, D. Pysz, R. Stępień, I. Kujawa, and M. R. Taghizadeh, "Focusing a Gaussian beam in nanostructured non-periodic GRIN microlenses," *Photonics Letters of Poland*, vol. 2, no. 1, pp. 34–36, 2010.

[42] A. K. Hartmann and H. Rieger, *Optimization Algorithms in Physics*. Berlin: Wiley-VCH, 2002.

[43] N. Metropolis, A. Rosenbluth, M. Rosenbluth, A. Teller, and E. Teller, "Equation of state calculations by fast computing machines," *Journal of Chemical Physics*, vol. 21, no. 6, pp. 1087–1092, 1953.

[44] A. F. Oskooi, D. Roundy, M. Ibanescu, P. Bermel, J. D. Joannopoulos, and S. G. Johnson, "MEEP: A flexible free-software package for electromagnetic simulations by the FDTD method," *Computer Physics Communications*, vol. 181, pp. 687–702, January 2010.

[45] S. Eitel, S. J. Fancey, H.-P. Gauggel, K.-H. Gulden, W. Bachtold, and M. R. Taghizadeh, "Highly uniform vertical-cavity surface-emitting lasers integrated with microlens arrays," *Photonics Technology Letters, IEEE*, vol. 12, pp. 459–461, May 2000.

[46] H. Otoma, A. Murakami, Y. Kuwata, N. Ueki, N. Mukoyama, T. Kondo, A. Sakamoto, S. Omori, H. Nakayama, and T. Nakamura, "Single-mode oxide-confined VCSEL for printers and sensors," in *Electronics Systemintegration Technology Conference, 2006. 1st*, (Dresden), pp. 80–85, IEEE, September 2006.

[47] D. K. Serkland, K. D. Choquette, G. R. Hadley, K. M. Geib, and A. A. Allerman, "Size dependence of small-aperture thin-oxide VCSEL's," in *1999 Digest of the LEOS Summer Topical Meetings*, pp. III15–III16, 1999.

[48] A. Boivin and E. Wolf, "Electromagnetic field in the neighborhood of the focus of a coherent beam," *Phys. Rev.*, vol. 138, pp. B1561–B1565, Jun 1965.

[49] M. R. Taghizadeh, A. J. Waddie, R. Buczynski, J. Nowosielski, A. Filipkowski, and D. Pysz, "Nanostructured micro-optics based on a modified stack-and-draw fabrication technique," *Adv. Opt. Techn.*, vol. 1, no. 3, pp. 171–180, 2012.

[50] J. M. Nowosielski, A. Filipkowski, A. J. Waddie, I. Kujawa, R. Stepien, R. Buczynski, and M. R. Taghizadeh, "Diffractive optics development with stack-and-draw technique," *Proceedings of SPIE*, vol. 8428, no. 1, 2012.

[51] H. Herzig, ed., *Micro-Optics: Elements, Systems And Applications*. Taylor & Francis, 2004.

[52] A. J. Waddie. private communication.

[53] S. R. M. Robertson, "Measuring birefringence properties using a wave plate and an analyzer," *Appl. Opt.*, vol. 22, pp. 2213–2216, Jul 1983.

[54] R.-P. Salmio, J. Saarinen, J. Turunen, and A. Tervonen, "Graded-index diffractive structures fabricated by thermal ion exchange," *Appl. Opt.*, vol. 36, pp. 2048–2057, Apr 1997.

[55] R.-P. Salmio, J. Saarinen, and E. Noponen, "Ion-exchanged diffractive elements in glass for substrate-mode optics," *Appl. Opt.*, vol. 37, pp. 5093–5098, Aug 1998.

[56] A. Lipovskii and V. Zhurikhina, "Is it possible to use ion exchange in glasses for producing effective diffraction gratings?," *Journal of Non-Crystalline Solids*, vol. 351, no. 52–54, pp. 3784–3788, 2005.

[57] A. A. Lipovskii, V. V. Rusan, and D. K. Tagantsev, "Imprinting phase/amplitude patterns in glasses with thermal poling," *Solid State Ionics*, vol. 181, no. 17–18, pp. 849 – 855, 2010.

[58] J. Ihlemann and D. Schäfer, "Fabrication of diffractive phase elements for the UV-range by laser ablation patterning of dielectric layers," *Applied Surface Science*, vol. 197–198, pp. 856–861, 2002.

[59] M. Schulz-Ruhtenberg, J. Ihlemann, and J. Heber, "Laser patterning of SiOx-layers for the fabrication of UV diffractive phase elements," *Applied Surface Science*, vol. 248, no. 1–4, pp. 190 – 195, 2005.

[60] R. Buczynski, I. Kujawa, R. Kasztelanic, D. Pysz, K. Borzycki, F. Berghmans, H. Thienpont, and R. Stepien, "Supercontinuum generation in all-solid photonic crystal fiber with low index core," *Laser Physics*, vol. 22, no. 4, pp. 784–790, 2012.